Single and multijunction silicon based thin film solar cells on flexible substrates with absorber layers made by hot-wire CVD

The cover is an optical microscopy image of the surface of a silicon epitaxial layer grown on a (100) mono-crystalline silicon wafer by Hot-Wire CVD.

ISBN: 978-90-393-4630-3

Print: Ponsen & Looijen b.v. graphic company, Wageningen

Single and multijunction silicon based thin film solar cells on flexible substrates with absorber layers made by hot-wire CVD

Flexibele enkelvoudige en multi-junctie dunne film silicium zonnecellen met absorberende lagen gemaakt via gasontleding aan een heet filament

(met een samenvatting in het Nederlands)

Proefschrift

ter verkrijging van de graad van doctor aan de Universiteit Utrecht op gezag van de rector magnificus, prof.dr. W.H. Gispen, ingevolge het besluit van het college voor promoties in het openbaar te verdedigen op woensdag 10 september 2007 des middags te 2.30 uur

door

Hongbo Li

geboren op 11 september 1971 te Tianjin, China

Promotor: Prof. Dr. R. E. I. Schropp

The work described in this thesis was financially supported by the Netherlands Agency for Energy and the Environment (SenterNovem) of the Ministry of Economic Affairs.

To my wife Ruiying, my son Yiming,

and my parents Zhe Li and Huiqin Liu.

Contents

1

Introduction

1.1 Renewable energy and silicon based thin film solar cells

With the continuous increase of the worldwide concern on the security of energy supply and the environmental problems of fossil and nuclear energy production, renewable energies such as wind energy, hydro energy and solar energy are catching much more attention than ever before. Photovoltaic devices based on solar energy, namely solar cells, directly convert sunlight to electric power and provide a clean, sustainable supply of energy, making them unique among all other energy sources.

Around 90% of the solar cells that are already in the market are made of crystalline silicon (c-Si) wafer, due to the abundance of its base material and the maturity of related technologies [1]. However, the enormous increase in the demand of raw material has made the cost of silicon ingots increase dramatically in the past few years [2]. Solar cell based on thin film silicon and its alloys is a good alternative, capable of fulfilling the fast increasing demand of a reliable solar cell supply. Also based on silicon, it has the advantage of base material availability, yet, it uses silicon much more efficiently, since the whole cell only needs Si layers that are at most a few microns thick in total instead of

hundreds of microns as in the case of c-Si based solar cell. This is due to the much higher optical absorption coefficient of such materials. Unlike crystalline silicon, thin film silicon materials are made via deposition on a foreign substrate, mostly by chemical vapor deposition (CVD) on substrates such as glass, stainless steel, or even plastic foils. The possibility to use a low cost substrate, the relative low processing temperature (~200 ºC), and the ease of mass production on large area substrates make thin film Si technology a strong competitor to c-Si based solar cells. At present, the limiting factors for the market expansion of thin film silicon based solar cells are the still relative high price compared to grid electricity, and the relative low energy conversion efficiencies.

A typical c-Si based solar cell contains a two-layer structure of a p-type and an n-type region, one of which is much thicker than the other (Fig. 1.1a). An electric field is formed over the p-n junction. Photocarriers are mainly generated in the field free region in the thick lightly doped layer. They diffuse towards the electric field region, where they are separated. Finally, they are collected in an external circuit. As a result, c-Si based solar cells are diffusion-type devices. Although the energy conversion efficiency of these solar cells can be nearly 25%, a major drawback of crystalline silicon is the fact that it is an indirect bandgap material. As a consequence, the absorption in the material is low, and thick layers are needed for efficient light absorption. As a result, nearly 40% of the module cost is due to the silicon only.

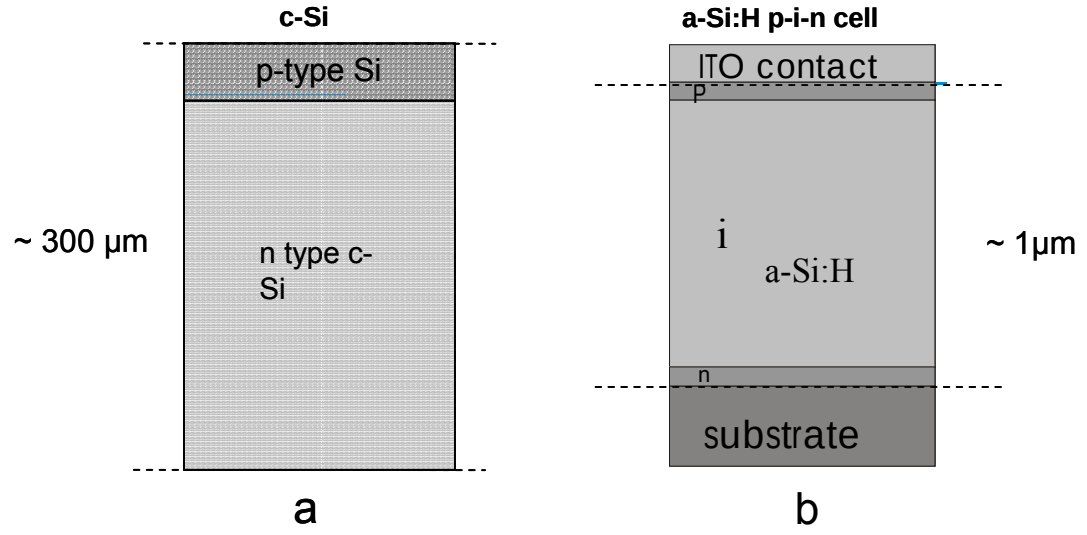

Fig. 1.1 Schematic structure of a c-Si p/n cell and a thin film silicon n-i-p cell.

A solar cell based on silicon thin films contains not only p- and n- doped layers, but also an intrinsic layer, where most of the light is absorbed (Fig. 1.1b). The reason of using such a sandwich structure, the so called p-i-n structure, is due to the very high

density of dopant-induced defects (>10^{19} cm^{-3}) that exist in the doped materials, which makes it impossible to efficiently collect photogenerated carriers from a conventional p-n junction. The doped layers generate an electric field over the intrinsic layer, where the electronic defect density is controlled to be minimal, typically ~10^{15} cm^{-3} for hydrogenated amorphous silicon (a-Si:H). Charge carriers are generated when light is incident on one side of the structure. They are separated and then move in opposite directions under the influence of the electric field. The electrons drift towards the n-layer and the holes to the p-layer, where they are collected, and a current is generated in the external circuit. This process is schematically illustrated in Fig. 1.2. Since the diffusion length of the charge carriers in a silicon based thin film is small (typically around a few hundred nm) compared to that of c-Si (up to ~1 mm), the charge collection is dominated by drift transport. A silicon based thin film solar cell is therefore a drift-type device. Due to the large amount of defects present in the i-layer, charge carriers are trapped during transport, resulting in a high recombination rate. The presence of an electric field in a solar cell increases the drift velocity of the charge carriers. As a consequence, the rate of charge carrier trapping in deep centers and the recombination rate are both decreased. Thus, to avoid recombination of charge carriers, the electric field should be as high as possible, which means that the intrinsic layer should be made as thin as possible. On the other hand, the thicker the i-layer is, the more light is absorbed, and the more charge carriers are generated. These two opposite requirements result in an optimal thickness of the intrinsic layer. For amorphous silicon, an optimal i-layer thickness is around 200~500 nm for a single junction p-i-n cell. This thickness is much smaller than that needed for c-Si based solar cells. As a result, the cost of the silicon in thin film silicon solar cells account for only a few percent of the module cost.

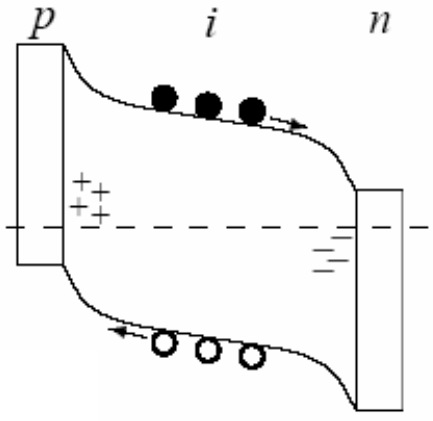

Fig. 1.2. The potential profile in a p-i-n (n-i-p) cell. The field (potential drop) in the middle part of the i-layer is weakened due to the charged defects near p- and n- side of the i-layer.

1.2 Thin film silicon and its alloys

A few different materials can be used as the absorber layer in a thin film silicon-based p-i-n solar cell. Among them, hydrogenated amorphous silicon is mostly used at the present.

Hydrogenated amorphous silicon (a-Si:H) consists of a covalent random network of Si-Si and Si-H bonds. The material does not have a long-range order, in contrast to its counterpart, crystalline silicon. However, short-range order is present, as the silicon atoms are mainly positioned in tetrahedral coordination with an average Si-Si bond length of 0.235 nm. This configuration is similar to the tetrahedral structure present in crystalline silicon. Since there is no long-range periodicity in a-Si:H, variations in Si-Si bond angles and Si-Si bond lengths exist, which are approximately 10% and 1%, respectively. Therefore, amorphous silicon has different optoelectronic properties than crystalline silicon.

Due to the distribution in bond angles and bond lengths, a considerably high density of strained Si-Si bonds is present. The energy levels associated with the electronic states of these strained or weak bonds are located in the band tails. The density of states (DOS) of these tail states decreases exponentially towards the middle of the bandgap. For amorphous silicon, typical values for the inverse slopes of these tails are ~50 meV for the valence band tail (also called Urbach tail), and ~25 meV for the conduction band tail. In addition to these strained bonds, voids and threefold coordinated silicon atoms are also present. The latter defect means that un-terminated or dangling bonds are present, with electronic states located near the center of the bandgap, where they act as effective recombination centers for free carriers. Dangling bonds can be occupied by zero, one or two electrons, which results in a positive, neutral, or negative charge, respectively. In pure, non-hydrogenated silicon, produced for example by sputtering, the dangling bond density is about 10^{19}-10^{20} cm^{-3}, which is much too high for application of this material in conventional electronic devices. In hydrogenated amorphous silicon, which contains typically 10 at. % of hydrogen, the majority of the dangling bonds is passivated by hydrogen atoms. In this case, the defect density is greatly reduced, to typically 10^{16} cm^{-3}. The presence of hydrogen is thus important for the optoelectronic properties of amorphous silicon. Fig. 1.3 shows a plot of the distribution of the density of states in intrinsic amorphous silicon.

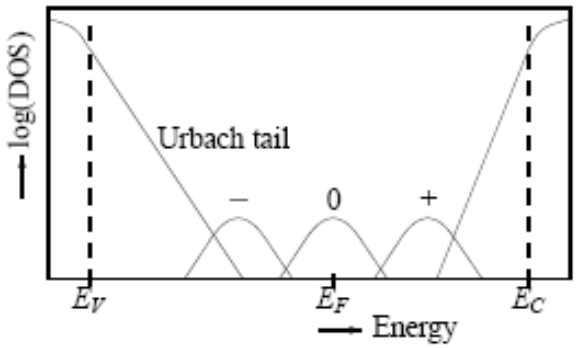

Fig. 1.3. The distribution of the density of states (DOS) in intrinsic amorphous silicon: - , 0, and + refer to the charge of the defect states [3]. E_V and E_C denote the position of the valence band edge and conduction band edge, respectively. E_F denotes the position of the Fermi level.

Amorphous silicon has several advantages over crystalline silicon. The lack of periodicity in a-Si:H implies a relaxation of the requirement of conservation of the wave vector for interband transitions in optoelectronic processes. Thus, amorphous silicon behaves as a direct-bandgap material and its visible-light absorption is much higher than that of crystalline silicon. Therefore, amorphous silicon solar cells can be made much thinner than crystalline silicon solar cells, and the material costs can be kept low. Furthermore, it is possible to tune the bandgap between 1.6 eV and 2 eV, depending on the deposition conditions.

By adding an appropriate other element, such as germanium (Ge), into the deposition of amorphous silicon, one obtains the alloy amorphous silicon germanium (a-$Si_{1-x}Ge_x$:H). By varying the index x, the energy band gap can be tuned, typically in a range between 1.3 eV to 1.7 eV. A further increase of the Ge/Si ratio will result in deterioration in the material quality, due to the increased degree of disorder in the atomic network.

Unfortunately, the electronic properties of amorphous silicon and its alloys degrade when the material is illuminated. This phenomenon was discovered in 1977 and is called the Staebler-Wronski effect (SWE), after its discoverers [4]. Due to the illumination the density of dangling bonds increases, and saturates after a long time. This light-induced increase in the defect density results in a reduced lifetime of the free carriers. The additional dangling bonds can be annealed out completely by heating the material to about 150 ^{o}C for a few hours. Although the effect has been known for 30 years, it is still unclear what the exact origin of this behaviour is. The energy for this process is most likely provided by the recombination of electron-hole pairs, but also the hydrogen concentration and the medium-range order in the material appear to play an important role in the process. Obviously, the presence of these additional defects has a large and undesirable influence on the material properties.

The plasma deposition process for a-Si:H will be described in section 1.4. The resulting structure of the material depends on the deposition conditions. Dilution of the silicon-containing (e.g. SiH_4) source gas with hydrogen during deposition results in silicon thin films with different atomic structures than amorphous silicon. For low hydrogen dilution, a material is deposited which has a higher medium-range structural order than standard amorphous silicon. This material also has a higher stability against light-induced changes than amorphous silicon, and it is often referred to as protocrystalline silicon [5]. For higher hydrogen dilution during deposition, a transition from amorphous to crystalline growth is observed. Depending on the amorphous fraction of the material, materials are referred to as protocrystalline silicon (proto-Si:H) or polymorphous silicon (pm-Si:H) [6], (hydrogenated) nano- or microcrystalline silicon (nc-Si:H; μc-Si:H) [7], or polycrystalline silicon (poly-Si) [8]. The increasing crystalline character of these materials results in an improved stability against light-soaking.

Microcrystalline silicon (μc-Si:H), also referred to as nanocrystalline silicon [9], is a two-phase material which consists of small crystallites embedded in an amorphous silicon matrix. The size of the crystallites is generally around 20 nm or smaller [10]. The bandgap of microcrystalline silicon can be tuned from about 1.1 to 1.6 eV, depending on the amorphous fraction present in the material.

1.3 Thin film silicon based multijunction solar cells

The existence of absorber materials with different band gap allows us to design solar cells with a "multijunction structure", in which every junction contains a different type of absorber material. By doing this, we can adjust the absorption spectral range of the whole structure to better match the solar irradiation spectrum. A good example of cells with this concept is the triple junction solar cell with a structure a-Si:H top cell/a-SiGe:H middle cell/μc-Si:H bottom cell, in which the three absorber layers a-Si:H, a-SiGe:H and μc-Si:H have optical bandgaps (E_{gopt}) of approximately 1.7 eV, 1.5 eV and 1.1 eV, respectively. Light first passes through the top cell, where photons with the highest energy (short wavelength) are absorbed; then the remaining light passes through the middle cell, where photons with medium energy (medium wavelength) are absorbed; and finally the light reaches the bottom cell, where photons with the lowest energy (long wavelength) are absorbed. Each subcell absorbs a portion of the incident light and generates a certain amount of current accordingly. By interconnecting all subcells in series, which is achieved automatically during successive layer deposition, the output of the whole structure shows a voltage that is the sum of the three subcell voltages and a current that equals the lowest current of the subcells. A schematic diagram of the structure of a triple junction thin film solar cell is shown in Fig. 1.4.

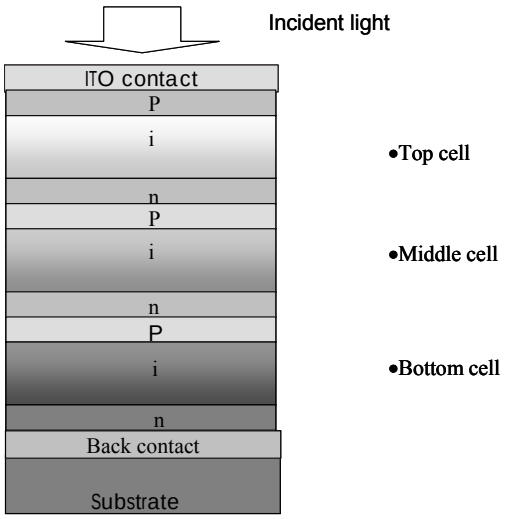

Fig. 1.4. Schematic structure of a substrate type triple junction thin film solar cell.

Another advantage of using a multijunction structure for a-Si:H based thin film solar cells is that for the same energy output, the thickness of each absorber layer is much less than that needed in a single junction cell. This is good for reducing the light induced degradation in the a-Si:H layer. Because of the SWE effect, the density of dangling bonds in the a-Si:H i-layer increases with the illumination time and the lifetime of free carriers reduces, which cause a deterioration of solar cell output performance with the illumination time. By decreasing the thickness of the intrinsic layer, the SWE effect is considerably reduced, due to the strong electric field that exists in the i-layer.

1.4 Plasma-enhanced chemical vapour deposition

At present, the plasma-enhanced chemical vapour deposition (PECVD) (also referred as the glow discharge) technique is the most widely used method for the deposition of device quality silicon-based thin films and solar cells. The technique is based on the dissociation of silicon-containing gases in a radio-frequency (RF) plasma, usually at a frequency of 13.56 MHz. The plasma is generated between two electrodes, and the substrate is attached to the grounded electrode. Inelastic collisions of energetic free electrons in the plasma with the source gas molecules result in the production of silicon-containing radicals (Si_xH_y), hydrogen radicals, and ions. These species can react further with other radicals, ions and molecules in the gas phase. Radicals that diffuse to the substrate can contribute to the film growth. For the growth of a compact layer, it is important that the surface mobility of the growth precursors is high. This surface mobility is greatly improved by hydrogen passivation of the already present surface

dangling bonds. A growth radical which reaches the surface of a growing film attaches to one of the hydrogen passivated surface silicon dangling bonds. In order to find an energetically favourable position, the radical can diffuse over the surface by hopping over the surface hydrogen atoms. Cross-linking with the neighbouring silicon atoms finally results in film growth, under the release of molecular hydrogen. For the deposition of device quality a-Si:H, SiH_3 radicals are believed to be the main growth precursors.

1.5 Hot-Wire CVD, a short history

One of the motivations to develop hot-wire CVD was to avoid the plasma damage of the conventional PECVD, which is now still a problem of this commonly used technique. Compared with PECVD, the method of depositing Si thin films by hot wire CVD is not yet mature, although the first patent on this technique already appeared in 1979 [11]. In 1979, Wiesmann et al. reported that silicon thin films could be formed by cracking silane (SiH4) gas with a heated tungsten (W) or carbon foil with a temperature of 1400-1600 ºC. At such temperatures thermal decomposition of silane into a gaseous mixture of hydrogen and silicon atoms was thought to take place. Since the background pressure they used was obtained with a normal rotary pump, and very low gas pressure ($<10^{-5}$ Torr) was used during the deposition, the material (a-Si:H) they made showed much lower photoresponse than that obtained by PECVD at that time: therefore, the method did not catch much attention. Several years later, without knowing the work of Wiesmann, the group of Matsumura at JAIST in Japan published their result of a-Si:H material deposited with a heated tungsten (W) wire and fluorinated silicon gases, which shows a very high photo-sensitivity (defined as the ratio between photo- and dark conductivity, σ_{ph}/σ_d) and a spin density around 6×10^{15} cm^{-3}, both characteristics of a good material [12]. Later, the use of silane also produced a-Si:H with promising material quality [13]. Since they inferred that the reactions taking place on the surfaces of the heated filaments are catalytic, they called this method catalytic chemical vapour deposition (Cat-CVD) [14]. Typical parameters used by Matsumura at that time were a relatively low filament temperature (1200-1400 ºC) in combination with a rather high pressure (>0.1 mbar) and large filament surface area (>5 cm^2). One of the reasons to work in a high-pressure regime was that at that time they also only used a rotary pump to get a background vacuum; with a high gas pressure, the influence of impurities, such as water vapor and oxygen, could be suppressed.

Similar to Matsumura's group, also unaware of Wiesmann's work, Doyle et al. studied silicon deposition using a heated tungsten wire, undiluted silane, and an intermediate pressure (4- 30 mTorr) [15]. By doing mass-spectrometry analysis, they

could identify the radicals emitted from the filament versus filament temperature (T_f). Over a wide range of T_f, they found that the SiH_4 was mostly atomized into H atoms and Si atoms, with only few other radicals present. They were thus able to differentiate between the work of Wiesmann and Matsumura. Wiesmann's films were deposited entirely from these Si and H radicals and Matsumura's materials from the products of gas phase reactions between these radicals and the ambient [15, 16]. Using $T_f \sim 1450$ ºC, σ_p/σ_d ratios > 10^5 were repeatedly obtained for film with a deposition rate r_d as high as 15 Å/s, suggesting that high quality a-Si:H was possible in this P = 4~30 mTorr regime[15].

Significant expansion in HWCVD research activity was, however, triggered by the work of Mahan et al. at NREL, who demonstrated in 1991 the possibility to produce device-quality a-Si:H with a H concentration below 1 at.-% [17,18]. In contrast to the a-Si:H material obtained by PECVD and other techniques, the electrical properties did not deteriorate when the H content was lowered. This was regarded as a significant progress in the silicon thin film technology, since the major disadvantage of a-Si:H as a photovoltaic material, the H assisted degradation under sun light illumination (the Staebler-Wronski effect), is believed to be reduced if the H content is lowered while maintaining a low level of sub-gap defect density.

With a thin tungsten wire, the deposition parameters Mahan used were also in the pressure range around several and several tens of mTorr as used by Doyle et al. [15], but with a much higher filament temperature, >1900 ºC. The necessity of using such a high filament temperature was later explained as being necessary to avoid the formation of tungsten-silicide which is detrimental to the catalytic ability of the filament [19]. The reason for using a smaller filament surface area and a much lower gas pressure than those used by Matsumura et al in their early research was to suppress the high radical flux at the growing surface, in order to have a better control on the material quality.

The ability of making microcrystalline silicon by HWCVD was realized by Matsumura et al. in 1991 [20], when they started to shift their deposition parameter regime from around 1 Torr to several mTorr. Microcrystalline silicon with high volume fraction, ~90%, as determined from the X-ray diffraction peak before and after annealing the sample at > 900 ºC in N_2, was obtained at a low gas pressure region, below several tens of mTorr. The film with a thickness around 1 micron deposited on a glass substrate was found to be completely (220) oriented and had an initial amorphous phase of around 0.2 μm - 0.3 μm. The real substrate temperature, estimated by thermally sensitive paint painted at the back side of the glass substrate, showed a value around 430 ºC. An interesting point in this work is that at the time Matsumura did this experiment, he was still using a filament temperature around 1300 ºC, measured by an infrared thermometer for a fresh filament. During the deposition, the filament was covered with silicide, which influenced the emissivity of the filament surface. He therefore adjusted the filament

power in order to keep the temperature reading from the thermometer constant. Due to the large difference between the emissivities of a fresh tungsten wire and a wire coated with tungsten-silicide, the real filament temperature during the deposition might have been several hundred degrees higher, so that actually it was right in the temperature range currently used by most of the researchers today.

1.6 Solar cells made with hot wire CVD

Although the quality of materials made by HWCVD was generally equal or better than obtained by PECVD at that time [17,18], the progress in obtaining good solar cell efficiency was initially very slow. One reason for the unbalance between the material and device development using HWCVD is that the major deposition technique for Si thin films has long been plasma CVD (PECVD), especially in the ultra large integrated circuit (ULIC) and TFT (thin film transistor) industries. In the field of silicon thin film solar cells, plasma CVD was the first successful technique in producing device quality amorphous silicon material and solar cell devices, mainly initiated by the first successful doping in a-Si:H materials by Spear and LeComber (1975-1976)[21, 22]. However, in developing high quality intrinsic microcrystalline silicon materials that can be used as an efficient absorber layer in a p-i-n structure, people using plasma CVD encountered a large problem - a too low deposition rate (r_d). The central reason for the low r_d is that in plasma CVD, the silane decomposition reaction happens in the gas phase by high-energy electrons. So in principle it is a point collision reaction, and the use of gaseous sources in that case is rather inefficient. In HWCVD, however, the silane breaking reaction happens on the surface of hot filaments, which is in principle a surface collision reaction, and the use of silane gases is much more efficient.

Another important reason for the slow development of solar cells made with HWCVD is that there was a lack of support from some major players in the this field, i.e. the companies and institutes that have been successful in making high performance solar cells, who had accumulated enough experience in device optimization to go in production with PECVD. The success of HWCVD in depositing a-Si:H films with excellent quality, motivated the research of the SID group at Utrecht University.

1.7 Previous work

At Utrecht University, the hot-wire CVD technique has been applied for the deposition of amorphous and microcrystalline silicon layers and solar cells during the PhD work of K.F. Feenstra [23] and M.K. van Veen [24]. Using tungsten filaments at a high substrate temperature, ~430 ºC, a deposition rate of more than 2 nm/s was reached

for intrinsic a-Si:H, but cells using this material as the absorber layer showed similar degradation after light soaking as those made with PECVD. This was attributed to the too high filament temperature used, which was necessary for tungsten filaments in order to prevent the formation of tungsten silicides that deteriorate the optoelectronic properties of deposited films [23].

Using tantalum as the filament material, it was possible to reduce the substrate temperature to values around 250 ºC, while the device quality of amorphous silicon was maintained. The hydrogen concentration for the material made at this temperature is rather high and the Tauc bandgap is 1.8 eV. This makes the material a good candidate to be used as the top cell absorber in a multijunction solar cell.

Deposition conditions for intrinsic microcrystalline silicon were also explored with tantalum filaments, at a substrate temperature around 250 ºC. Material deposited at high hydrogen dilutions $R_H > 0.93$ (R_H defined as gas flow ratio $H_2/(SiH_4 + H_2)$) had a high crystalline ratio and showed a random orientation. The average crystallite size ranged between 10 nm and 25 nm. The bandgap of the material was around 1.25 eV. Materials made at hydrogen dilutions higher than 0.971 oxidized upon exposure to air, indicating a porous nature; those made at hydrogen dilutions below 0.96 did not oxidize. It was found that the structure of the material made at a dilution of 0.935 is inhomogeneous along the growth direction – it becomes less crystalline with increasing thickness.

Single-junction n-i-p structured solar cells using hot-wire deposited films as the absorbing layers resulted in initial efficiencies of 7.2% for amorphous silicon and 4.8% for microcrystalline silicon without using light-trapping techniques such as a textured back reflector (TBR). Preliminary results on n-i-p/n-i-p structured tandem solar cells showed an efficiency of over 8.5% (measured without an illumination mask) for a-Si:H/a-Si:H tandem cells, 6.1% for a-Si:H/µc-Si:H tandem cells (measured with a mask) and 8.5% for a a-Si:H/µc-Si:H/µc-Si:H triple cells (measured without a mask). For optimization on the current matching of the subcells, an improvement on the tunnel-recombination junction was suggested. [24]

1.8 Aim of this work

The primary aim of this work was to develop thin film single and multijunction solar cells on stainless steel foil with the absorber layers made of silicon and its alloys using the HWCVD method. Concentrated efforts were put on identifying problems that exist in the structure of the devices and on following an appropriate way to solve them. Challenges existing for the intrinsic layers, the doped layers, TCO layers and the interfaces between them are discussed; problems that arose upon the use of textured back reflectors are particularly stressed since a significant improvement in solar cell efficiency

was expected only by employing a properly designed rough back reflector. This knowledge has been transferred to triple junction solar cells, leading to devices with good efficiencies.

1.9 Outline of this thesis

The subject of this thesis is single and multijunction thin-film silicon solar cells with i-layers deposited by HWCVD. In total, the thesis consists of eight chapters.

Chapter 1 provides an introduction on thin film silicon solar cells and the history of hot-wire CVD.

In chapter 2, details of the hot wire chemical vapor deposition technique are explained, and the major techniques involved in silicon thin film solar cell device characterization are described.

Chapter 3 addresses the influence of rough Ag/ZnO substrates on μc-Si:H n-i-p cells with an i-layer deposited by HWCVD. The first part deals with the shunting problems observed for cells deposited on substrates with a rough back reflector. The second part studies the surface roughness dependence of the open circuit voltage (V_{oc}) of the cell. In the third part, the development of μc-Si:H on a rough surface is investigated and a crack forming theory is presented. At the end of this chapter, a diagram is given for the influence of the substrate morphology on the performance of μc-Si:H solar cells.

Chapter 4 introduces a specially designed (reverse) H_2 profiling technique aiming for an improvement of the quality of the intrinsic layer in a μc-Si:H n-i-p cell. Emphasis is put on the opposite behaviour found in the growth evolution of μc-Si:H deposited by hot-wire CVD compared to PECVD.

Chapter 5 discusses the interface barriers discovered at the TCO/p/i region of single junction n-i-p cells. From a study of the dark *J-V* characteristics, a fingerprint is found for solar cells having barriers near this region. The voltage dependence of the diode quality factor (n-V curve) is found to be useful for recognizing transport problems in thin film silicon diodes (including solar cells).

Chapter 6 discusses a special phenomenon discovered when using spectral response technique to characterize single junction μc-Si:H solar cells - the photogating (PG) effect. Experimental findings are explained with the help of computer simulations. The possibility to use this phenomenon in identifying problems in a solar cell device is discussed.

Chapter 7 presents the work of integrating all sub-cells into a triple junction structure. Issues discussed include the optimization of the tunnel recombination junction,

studies on the very high fill factor (*FF*) observed on proto-Si:H/µc-Si:H tandem cells, and the best triple cell efficiency with i-layers made by HWCVD obtained within the time frame of this research.

Finally in chapter 8, the main conclusions of this thesis are summarized, and the outlook for further developments is given.

References

1. M.A. Green, *Solar cells: Operating principles, Technology and system Applications*, Prentice-Hall, New Jersey, 1982, ISBN 0 85823 580 3.
2. W.G.J.H.M. van Sark, G.W. Brandsen, M. Fleuster, M.P. Hekkert, Energy Policy 35 (2007) 3121.
3. M. J. Powell and S. C. Deane, Phys. Rev. B 48 (1993) 10815.
4. D. L. Staebler and C. R. Wronski, Appl. Phys. Lett. 31 (1977) 292.
5. R. J. Koval, J. Koh, Z. Lu, L. Jiao, R. W. Collins and C. R. Wronski, Appl.Phys. Lett. 75 (1999) 1553.
6. P. Roca i Cabarrocas, J. Non-Cryst. Sol. 31 (2000) 266.
7. E. Vallat-Sauvain, U. Kroll, J. Meier, A. Shah and J. Pohl, J. Appl. Phys. 87 (2000) 3137.
8. R. E. I. Schropp, B. Stannowski, A. M. Brockhoff, P. A. T. T. van Veenendaal and J. K. Rath, Mater. Phys. Mech. 1 (2000) 73.
9. M. Fonrodona, D. Soler, J. M. Asensi, J. Bertomeu and J. Andreu, J. Non-Cryst. Sol. 14 (2002) 299.
10. R. E. I. Schropp, K. F. Feenstra, E. C. Molenbroek, H. Meiling and J. K. Rath, Phil. Mag. B 76 (1997) 309.
11. H. Wiesmann, A. K. Ghosh, T. McMahon, and M. Strongin, J. Appl. Phys. 50 (1979) 3752; H. J. Wiesmann, U.S. Patent No. 4,237,150; Dec. 2, 1980.
12. H. Matsumura, Jpn. J. Appl. Phys. 25 (1986) L949.
13. H. Matsumura, J. Appl. Phys. 65 (1989) 4396.
14. H. Matsumura, Mat. Res. Soc. Symp. Proc. 118 (1988) 43.
15. J. Doyle, R. Robertson, G.H. Lin, M.Z. He, and A. Gallagher, J. Appl. Phys. 64 (1988) 3215.
16. A.H. Mahan, Solar Energy Mater. Solar Cells 78 (2003) 299.
17. A. H. Mahan, B. P. Nelson, S. Salamon, and R. S. Crandall, J. Non-Cryst. Solids 137&138 (1991) 657.
18. A. H. Mahan, J. Carapella, B.P. Nelson, R.S. Crandall and I. Balberg, J. Appl. Phys. 69 (1991) 6728.

19. A. H. Mahan, A. Mason, B. P. Nelson, and A. C. Gallagher, Mat. Res. Soc. Symp. Proc. Vol. 609 (2000) A6.6.1.
20. H. Matsumura, Jpn. J. Appl. Phys. 30 (1991) L1522.
21. W.E. Spear and P. G. LeComber, Solid State Commun. 17 (1975) 1193.
22. W.E. Spear and P.G. LeComber, Phil. Mag. 33 (1976) 935.
23. K.F. Feenstra, *Hot-wire chemical vapour deposition of amorphous silicon and. the application in solar cells,* PhD thesis, Utrecht University, the Netherlands, 1998.
24. M. van Veen, *Tandem solar cells deposited using hot-wire chemical vapor deposition,* PhD thesis, Utrecht University, the Netherlands, 2003.

2

Hot-Wire reaction mechanism and experimental techniques in solar cell characterization

In this chapter, I first give an overview of the hot-wire reaction mechanism as known so far. The information collected in section 2.1 gives a basic knowledge on hot-wire chemical reactions, and their possible influence on hot-wire deposited films. Section 2.2 and 2.3 briefly summarize the experimental techniques for deposition and characterization of thin film silicon solar cells, which are commonly referred to in all the following chapters.

2.1 An overview of the Hot-Wire reaction mechanism

The first systematic study of the mechanism of the Hot-Wire deposition process was done in the late 1980s by Doyle et al. [1] of the University of Colorado. He used a technique called threshold ionization mass spectroscopy (TIMS), which enables discrimination of radical species from silane (SiH_4) due to their lower ionization

potentials compared to that of SiH_4. The hot surface was the W filament of a commercial quartz halogen lamp. SiH_4 was led into a glass tube and pumped out through a sampling hole which served as the entrance of a differentially pumped mass spectrometer. This sampling hole could be moved laterally to align it with the mass spectrometer entrance, thus maximizing the radical beam signal. The two apertures could also be deliberately misaligned to remove the radical beam but retain the stable gas background signal. Since low pressures (<10 mTorr) and a very small filament–aperture gap (2 mm) were used, almost all radicals entered the mass spectrometer without undergoing gas phase collisions [2].

To discuss the surface decomposition of SiH_4, the standard flowing-reactor equation can be used, i.e.

$$F_0 = F + D' \tag{2.1}$$

in which F represents the radical flux entering the detector orifice when there are reactions happening on the filament surface (at a filament temperature T) and F_0 the silane flux when no reactions take place (when T is sufficiently low). D' is the difference between these two signals, and is equal to the SiH_4 decomposition rate on the filament surface, D, multiplied by a proportionality factor k $(0<k<1)$,

$$D' = kD \tag{2.2}$$

k is a geometry-related factor which changes with the position and angle of the sampling hole relative to the hot filament. Assuming α is the decomposition efficiency per silane collision with the surface, v_f the average speed of the SiH_4 molecules near the hot surface, A_f the filament surface area, and $[SiH_4]_f$ the density at filament temperature T, D can be written as

$$D = \frac{1}{4}\alpha v_f A_f [SiH_4]_f \tag{2.3}$$

In a similar way, F and F_0 can be written as

$$\begin{aligned} F &= \frac{1}{4} v_s A_s [SiH_4]_s \\ F_0 &= \frac{1}{4} v_{s0} A_s [SiH_4]_{s0} \end{aligned} \tag{2.4}$$

where the subscripts for *v*, *A* and *[SiH4]*, denote the quantities at the sampling hole position during reaction (*s)* and when there is no reaction (*s0*). Thus,

$$\alpha = \frac{1}{k}\frac{A_f}{A_s}\left(\frac{v_{s0}[SiH_4]_{s0} - v_s[SiH_4]_s}{v_f[SiH_4]_f}\right) \qquad (2.5)$$

Generally, both *v* and [SiH_4] are temperature dependent. For simplicity, we take the ideal gas assumption. Then, the mean velocity *v* of a gas molecule of mass M at absolute temperature T is given by

$$v = \left(\frac{8k_BT}{\pi M}\right)^{\frac{1}{2}} \qquad (2.6),$$

where k_B is the Boltzmann constant. We have,

$$\alpha = \frac{A_f}{kA_s}\left(\frac{T_{s0}^{\frac{1}{2}}[SiH_4]_{s0} - T_s^{\frac{1}{2}}[SiH_4]_s}{T_f^{\frac{1}{2}}[SiH_4]_f}\right) \qquad (2.7)$$

If we completely neglect the temperature dependence of *v* and *[SiH4],* α can be further simplified as

$$\alpha \propto \frac{A_f}{A_s}\left(\frac{S_0}{S} - 1\right) \qquad (2.8),$$

where S denotes the detected signal by the mass spectrometer when reactions are taking place and S_0 if there are no reactions. Therefore, by simply detecting the Si radical species with and without heating the filament, one can estimate the SiH_4 decomposition efficiency at the filament surface. This was the form used by Doyle et. al [1]. By logarithmically plotting α against *1/T*, one can estimate the activation energies for the detected radicals. Fig. 2.1 shows the results measured by threshold-ionization mass spectrometry using an undiluted SiH_4 source. The detected signals for different radical species (Si, SiH_3, H) were calibrated by taking into account the mass spectrometer sensitivity and ionization cross sections. Absolute calibration was done by normalizing

these signals to the silane decomposition by assuming that every Si atom from decomposed silane is evaporated at very high filament temperatures. This is consistent with negligible filament resistance changes (alloying) observed under these conditions.

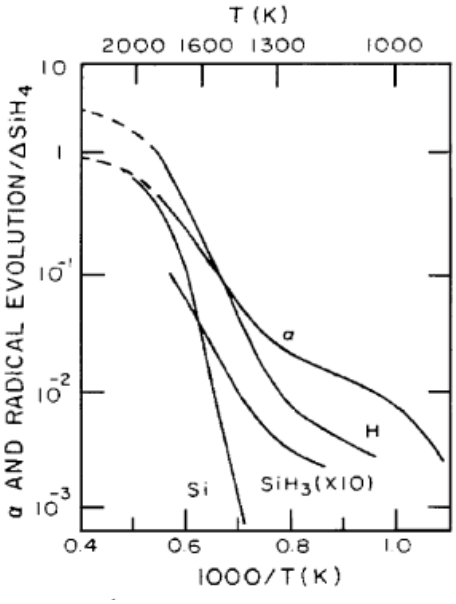

Fig. 2.1 Radical production and α vs. T^{-1} for an initial silane pressure of 10 mTorr. The dashed portions of the curve are averages through scattered data, whereby the scattering is attributed to changes of the filament surface (from Doyle, et al [1]).

Of interest in Fig. 2.1 is the significant H production. Three regions could be identified from the H curve. At T_f>1800 K essentially every H from a silane molecule evolves as an H atom. The $H/\Delta SiH_4 \sim 4$ observed at higher temperatures justifies the used normalization, i.e. that a SiH_4 molecule is completely dissociated at a high filament temperature. Below 1800 K some H evolves as H_2, so that the H atom flux has an activation energy of ~ 42 kcal/mole from 1300 to 1800 K and ~ 11 kcal/mole below 1300K. It was proposed that at T_f > 1800K, H surface coverage on the W surface was small and H atoms evaporated before recombining into H_2. At T_f <1800K, surface H coverage was high and the lower energy required to evolve H_2 favours its evolution. The H/H_2 evolution below 1800K is consistent with the thermodynamics for the H_2 - 2H reaction as a function of T_f.

At T_f < 1700 K in Fig. 2.1 the Si evolution falls below the silane decomposition α, so that a Si film or Si/W alloy was growing on the W filament. The observed Si evolution was attributed to the Si evaporation from this surface. The activation energy of ~ 83 kcal/mole is comparable to the energy required for evaporation of Si.

After the result of Doyle, more groups put their effort in investigating this issue. It is worth to mention that in more recent publications, researchers have been trying to separate the gas phase reactions from the reactions occurring on the filament surface more strictly. For this purpose a very low operation pressure, typically around a few mPa, was used, which is almost 3 orders of magnitude lower than that used by Doyle. At such low pressures, the mean free path of silicon radicals investigated can be tens or hundreds times larger than the chamber geometry. Therefore molecular collisions in the gas phase can be completely ruled out. Results are then more trustworthy for the study on reactions taking place at the filament surface. In agreement with Doyle et al. [1], most groups find that at a high enough filament temperature the largest Si-containing radical signal is that of Si. Tange et al. [3] used a 1% SiH_4 in He mixture and observed the dominance of the Si signal at $T_f >$ 1800K, while Nozaki et al., using Laser Induced Fluorescence (LIF) [4], saw a saturation of this Si with a very low activation energy of 5.0 kcal/mole between 1900K and 2300K. However, in the latter case the SiH_4, especially for the small amount used, might have been depleted at such a high filament temperature.

Duan et al. [5], also using VUV single photon ionization (SPI) but with pure SiH_4, observed Si production at all T_f investigated (>1500K). Holt [6] used threshold ionization mass spectrometry and pure silane, the same technique and gases as those used by Doyle but at this lower pressure, reported the same trend as that of Doyle et al. [1] and Duan et al. [5].

Electron emission

At the beginning of the development, one of the important differences between the hot-wire technique and glow discharge plasma deposition was regarded to be the total absence of electron and ion-induced effects [8]. But a hot filament is expected to show thermal electron emission. Upon application of a substrate bias, a considerable electron current as well as an ion current was observed. Therefore the electron impact effect can not be completely ruled out [9]. However, as long as no external bias is applied or the substrate is well grounded such that no significant static voltage can be accumulated on the substrate surface, the electron energies are believed to be too low to significantly affect the film growth.

Filament reactions under deposition conditions

Although much knowledge has been gained in the past decades about reactions happening at the filament surface at a very low pressure (a few mPa), studies of reactions under practical deposition conditions (a few Pa) are still in their early stage. The main complication of doing direct analysis comes from the difficulties in separating the signal from gas phase reactions and filament surface reactions. Indirect measurements, however,

can provide useful information. It was found that when used in a deposition, filaments quickly age and the electrical properties of the filament material are altered [10]. This instigated Holt et al. to study the radical chemistry of an aged filament [11]. With threshold ionization mass spectroscopy, they found that for aged W wires at high temperature (> 2100 K), the activation energy for all radicals detected (namely Si, SiH, SiH_2 and SiH_3) is higher than those for new wires. In particular, the low activation energy, which is believed to be a sign of catalytic reaction involving an H atom exchange at the filament surface, for SiH_3 of around 8 kcal/mol when using a new wire, becomes much larger when an aged filament is used, namely ~ 110 kcal /mole. This suggests that the aging of the wire has led to a reduction, if not an elimination, of its catalytic ability. Si is still observed to be the predominant radical (above 2100 K), but with an activation energy of ~ 120 kcal/mole at higher temperatures, which is consistent with evaporation from liquid silicon. Also, in contrast to the results obtained with the new filament, SiH and SiH_2 are both in greater abundance than SiH_3 (Fig. 2.2).

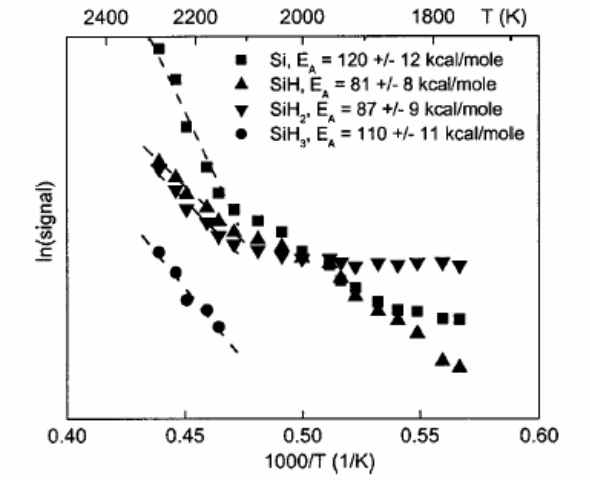

Fig. 2.2 Result of Holt et al.: SiH_x radical signals measured from an aged W wire at a total pressure of 5×10^{-6} Torr. Activation energies quoted are accurate within ± 10 %, due to uncertainties (± 50K) in wire temperature; error bars are not shown (from [11]).

Influence of different filament materials

Moreover, various filament materials have been examined in relation to Si radical detection. Working in the low pressure region, ~ 1 mPa, Duan et al. [7] studied the Si radicals produced from W, Re, Mo and Ta filament materials by laser based single photon ionization (SPI) as a function of the hot wire temperature. A similar predominance of Si radicals was seen for all the filaments in a temperature range above 1600 ºC - 1800ºC (depending on filament material). At the temperatures below 1600 ºC, different filaments show different activation energy for silicon radical production, and

they are all lower than the energy that is needed to pyrolytically cleave four Si-H bonds, ~308 kcal/mole. This suggests a catalytic nature of the filament surface reaction. Table 2-1 lists the apparent temperature activation energy of Si as measured by Duan [7] for different filament materials.

Table 2-1 Apparent temperature activation energies (in kcal/mole) using UVU SPI technique for different filament materials.

W	*Ta*	*Re*	*Mo*
30-60	140-170	30-60	120-160*

* Data for Mo filament are taken from a more recent publication from the same group [12].

To understand the difference in Si activation energies between each material, a multiple-step filament surface reaction process has to be considered, i.e. the reactions like silane adsorption, silane dissociation into adsorbed Si and H, Si diffusion, and H and Si desorption. The apparent activation energy for Si production from a filament at constant silane pressure is dominated by the activation energy of the rate-limiting step, i.e. the step with the lowest reaction rate, during the decomposition process. Considering the thermal desorption of evaporated Si from a metal (Ta, W, Mo, Re) surface, it was proposed that the silicon desorption from Ta at the aforementioned temperature range and with low silicon coverage is the silicon desorption from the tantalum surface. Similarly, the desorption from Mo was also attributed to desorption from the metallic surface. However, the Si desorption from W and Re is most likely from a Si layer which has already been accumulated on the metal surface. Proof for this postulation comes from the observation that the activation energies for these two materials are much lower than the thermal desorption energies from clean W and Re surfaces, but comparable to the average bond energy for a Si-Si single bond [12]. Also, Si seems to have a lower diffusion coefficient in tungsten than in tantalum [13]. And a free silicon layer on a tungsten surface was observed in the tungsten silicidizing experiment at a filament temperature of 1000-1600ºC.

Gas phase reactions

The radicals created at the filament surface will further react in the gas phase if the pressure is high enough, i.e. larger than a few μbar for a typical deposition configuration. From a material quality point of view [14, 15], the most important reactions are

$$H_2 + SiH_4 = SiH_3 + H_2 \qquad (1.9),$$

and

$$Si + SiH_4 = HSiSiH_3^* \qquad (1.10).$$

The reaction rates for these two reactions are of the order of the collision rate for a silicon atom with silane, i.e. the probability for a chemical reaction is close to unity upon a collision with a silane molecule. At a too low pressure, a high density of Si atoms reaches the substrate, resulting in a disordered material due to the high sticking probability of Si atoms [16]. At too high pressures, multiple reactions of the radicals occur and higher silanes or SiH and SiH_2 are formed [1, 4] by further abstraction reactions, which leads to a porous structure of the material [17].

2.2 Experimental techniques

2.2.1 Deposition of silicon and its alloys

Chemical vapour deposition system: PASTA

All the silicon layers involved in this study were deposited in the vacuum deposition system called PASTA. This is an UHV system with 5 deposition chambers and a load-lock. Deposition of the intrinsic silicon layers is performed by Hot Wire Chemical Vapour Deposition (HWCVD), that of doped layers and the SiGe:H layers by Plasma Enhanced Chemical Vapour Deposition (PECVD). The p-, i- and n layers are made in separate chambers and all chambers are connected to each other via a central transport chamber. SiH_4, GeH_4, CH_4, PH_3, TMB, and H_2 gas lines are connected to the system to make, a-Si:H, proto-Si:H, µc-Si:H, poly-Si, µc-Si(B), a-Si:H(P), a-SiC:H(B), µc-Si(P), and a-$Si_{1-x}Ge_x$:H films on 10 cm x 10 cm substrates or to perform interface treatments. A schematic drawing of a typical hot-wire CVD reactor is shown in Fig. 2.3.

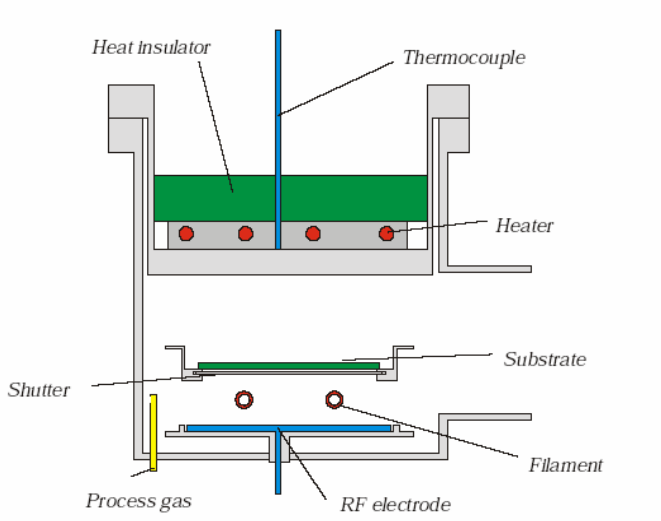

Fig. 2.3 Schematic drawing of a pasta chamber for Hot-Wire deposition. Picture was drawn by C.H.M. van der Werf.

Substrate temperature calibration for Hot-Wire deposited layers

One of the main characteristics of hot-wire CVD is the substrate heating from the hot filaments. For a certain system configuration, described by the surface-filament distance, gas pressure, filament type and dimensions, and chamber geometry, the amount of heat reaching the substrate surface can be predicted [18]. Fig. 2.4 shows the temperature (T_{sub}) as measured at the center of substrate by a thermocouple at different filament current (I_{fil}) and different heater temperature (T_{set}). As can be seen, even with the T_{set} set to zero, the substrate is still at a rather high temperature. For most of our depositions, both for proto-Si:H and µc-Si:H i-layers, we use a filament current of 10.5 A with the substrate heater set to off. These settings are chosen after the intensive study on hot-wire deposited silicon materials by M. van Veen [19] The substrate temperature is typically around 250ºC for a 1.1 mm thick Corning glass substrate, and 270ºC for a 150 µm stainless steel sheet or a 300 µm thick c-Si wafer.

Thickness profile and sample configuration

The thickness homogeneity of hot-wire deposited layers does not directly depend on the shape or size of deposition chamber, due to the absence of plane electrode commonly used in a PECVD setup. Therefore scaling up for industry production is straightforward. But certain parameters such as filament configuration do cause thickness differences on different sample positions. Throughout our research, we did not spend time on optimizing film homogeneity; instead, we often use it as a parameter to obtain extra information of the deposited sample. Most of our depositions were done with the sample strips, either glass sheets or stainless steel foil, fixed in the centre of the substrate

holder and with the longer dimension perpendicular to the filaments. Since we only use two wires, there is quite some thickness inhomogeneity on the deposited layers. Fig. 2.5 shows the thickness profile for a proto-Si:H sample deposited on Corning 1737 glass substrate; The position of two 2 cm × 10 cm substrate relative to thickness profile is also shown. The thickness uniformity is within 100± 5% over an area of approximately 25 cm^2. Towards the edge of the substrate, however, the film thickness drops to approximately 80% of that in the center at a position of around 1cm from the edge. This gives a range of i-layer thickness as well as substrate temperature at different cell positions. To have a complete picture of the influence of deposition condition variations on cell properties, *J-V* characteristics were recorded for all the cells on each sample strip.

In most of our discussion, the measurements are compared between cells located in the center of the substrates. In some cases, however, cells on the edge are also discussed. For a few μc-Si:H n-i-p cells, we deliberately put the sample to the side of the deposition area to study the effect of a larger substrate-filament distance and a lower substrate temperature. As a way to obtain extra information, position dependent cell *J-V* characteristics were, actually, intensively used as a useful tool for both single and multi-junction solar cell optimization.

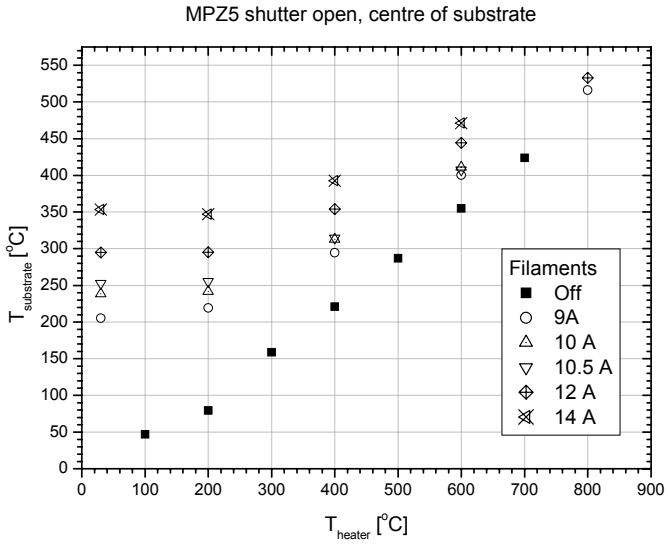

Fig. 2.4 The substrate temperature (T_{sub}) measured at the centre of a glass substrate by a thermocouple at different filament current (I_{fil}) and different substrate heater temperature settings (T_{set}).

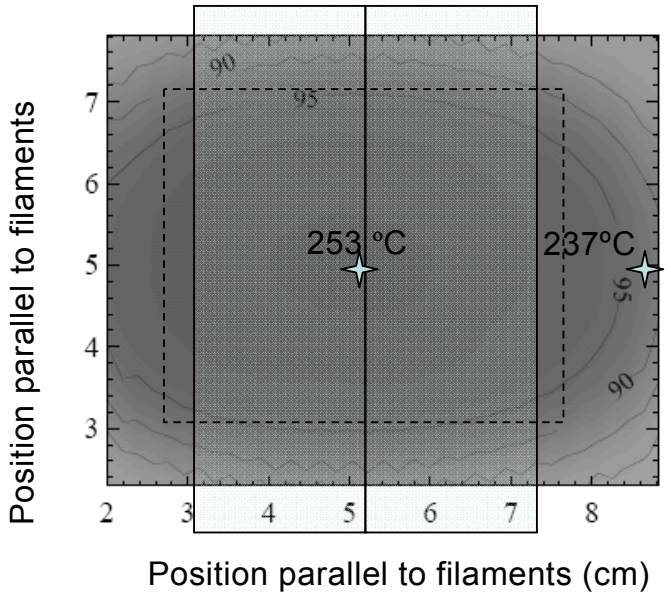

Fig. 2.5 The thickness profile for a proto-Si:H sample deposited on Corning 1737 glass substrate. The region surrounded by dashed lines indicates the homogenous square, where the thickness deviation is within ~5% of the centre thickness.

Standard deposition parameters

Table 2-2 gives an overview of the standard deposition parameters for the devices and materials made in PASTA.

Table 2-2 Standard deposition parameters for the materials made in PASTA.

	p-µc-Si:H	***i-µc-Si:H***	***i-proto-Si:H***	***i-SiGe:H***	***n-a-Si:H***	***n-µc-Si:H***
Chamber #	1	5	5	2	3	3
CVD	RF-13.56 MHz	Hot-Wire	Hot-Wire	RF-13.56 MHz	RF-13.56 MHz	RF-13.56 MHz
Electrode distance (mm)	14	-	-	12	23	23
SiH_4 (sccm)	0.53	5~7	90	2.1	5	0.7
H_2 (sccm)	100	100	-	186	40	100
TMB (sccm)(1% in He)	0.26	-	-	-	-	-
PH_3 (sccm) (1% in He)	-	-	-	-	10	0.6
GeH_4 (sccm)	-	-	-	1~3	-	-
Pressure (mbar)	1100	20	50	2200	300	990
Heater Set Temperature (ºC)	260	0	0	320	230	230
RF-Power (W)	10	-	-	3~6	3	10
Filament current (A)	-	10.5	10.5	-	-	-

2.2.2 Deposition of the front and back contacts

2.2.2.1 Sputtering system SALSA

Most of the depositions for the top and back contact involved in this research were performed in a sputtering system SALSA (Sputtering Apparatus for Light Scattering Applications). The system consists of one load lock with a movable cooling stage and a process chamber equipped with four torus magnetron sputter sources, each with its own matching network. In order to avoid cross contamination between targets during deposition, the targets are separated from each other by four liner shields and one horizontally placed contamination shield with four circular openings. Slightly above this shield a rotating shutter plate is placed with one circular opening. During the course of this research, three target positions have been used with a fixed material, namely Ag, ZnO:Al (1%) and In_2O_3:Sn_2O_3 (10%), for the deposition of a textured back reflector (Ag/ZnO) and transparent top contact ITO. In Table 2-3, the standard deposition parameters for the three fixed target materials are given.

Table 2-3 Standard sputtering parameters for three different types of target materials.

Target material	***Ag***	***ZnO:Al (1%)***	***ITO***
Target-substrate distance (mm)	140	125	115
Power (W)	500	300	400
Pressure (μbar)	2	3	20
Temperature setting (^oC)	200-400	0-250	0-150
Substrate temperature (^oC)	200-280	90-230	90-180
Gas flow (sccm) Ar	10	6.6	20
Ar:O_2 (0.3%)	-	3.3	3.3
Deposition rate (nm/min)	33.3	10.0	6.2
Deposition time (s)	1600	600	770

2.2.2.2 Short description on the masking system used for the ITO/metal grid deposition

To define the area of the sample solar cells 0.3 mm thin stainless steel masks with 4 x 4 mm^2 square openings were used during the ITO front contact deposition. Sample strips are typically 10 cm long, and 2 or more cm wide. This allows 16 columns (Y direction) and 3 or more rows (X direction) of sample cells. Therefore the minimum amount of 48 cells is available to characterize the properties of that sample. The columns are counted with alphabetic letters from A to P, and the rows with numbers from 1. Therefore every cell has a name like A1, A2, A3, B1, B2, …, P2 and P3. To reduce the series resistance, a metal (Au or Ag/Al) grid is evaporated on top of the ITO with another

mask. The active area of the cell for the light *J-V* characterization as the area of an ITO square minus the area of the metal grid on top of it and is calculated to be 0.131 cm^2.

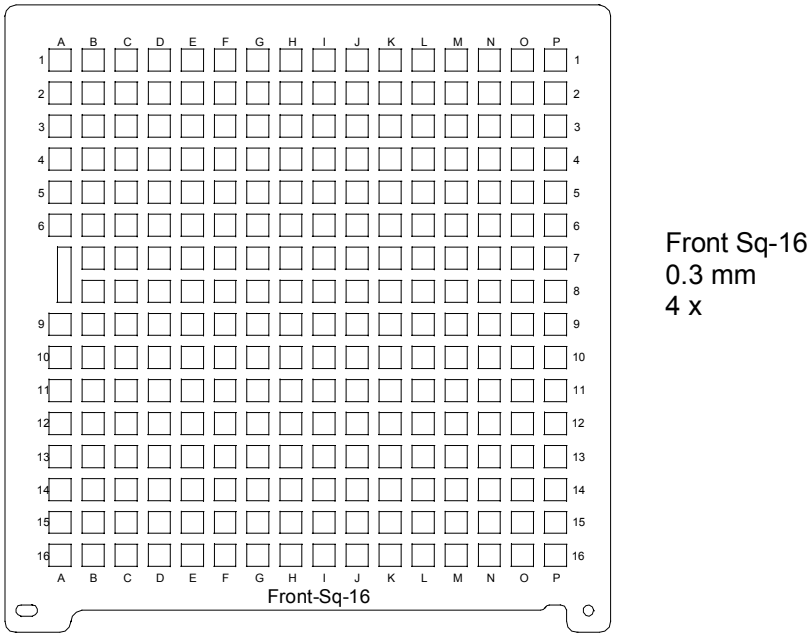

Fig. 2.6 The ITO mask used for depositing ITO contact and for AM1.5 light *J-V* measurement.

2.3 Solar cell Characterization techniques

The two most important techniques for solar cell characterizations are the Current density-Voltage (*J-V*) measurement and the Spectral Response (SR) measurement.

2.3.1 *J-V* measurement

2.3.1.1 Current-voltage characteristics of a solar cell

In most cases, the electrical properties of a silicon based thin film solar cell can be represented by the equivalent circuit shown in Fig. 2.7. The areal current density J, defined as the current flow through the two contacts of the device divided by the total area of the cell can be written as:

$$J = J_0(e^{\frac{q(V-JR_s)}{nkT}} - 1) + \frac{V - JR_s}{R_p} - \alpha\Phi + J_{rec}(J) \quad (2.11),$$

in which, the first term to the right of the equal sign is the diode current density represented as J_{diode} in Fig. 2.7, the second the shunting current density J_{par}. The third

term is the photogenerated current density J_{ph} and is generally proportional to the intensity of the incident light (photon flux Φ). The fourth term is the internal recombination current density J_{rec}, which is related to the current density J. J_0 is the reverse saturation current density of the diode, n the diode quality factor, k the Boltzmann constant, T the absolute temperature, q the elementary charge, V the applied voltage, R_s the areal series resistance, R_p the areal parallel resistance, α is a proportionality factors which depend on the type of material. The value of the diode quality factor n is 1 in the case of diffusion-driven current, and 2 for pure field-driven current [20]. A combination of these different current modes results in a value for the diode quality factor between 1 and 2. The current density J at zero voltage defines the short-circuit current density J_{sc}, and the voltage at zero current density is called the open-circuit voltage V_{oc}. In Fig. 2.8 the AM1.5 current density of an amorphous silicon solar cell is plotted as a function of the applied voltage. In this figure also some of the above discussed cell parameters are indicated. From the J-V curve measured under illumination, the differential resistances R_{sc} and R_{oc} are defined:

$$R_{sc} = \left(\frac{dJ}{dV}\bigg|_{V=0}\right)^{-1} \qquad (2.12),$$

$$R_{oc} = \left(\frac{dJ}{dV}\bigg|_{J=0}\right)^{-1} \qquad (2.13).$$

The degree of deviation from a rectangular shape is expressed by the fill factor FF, defined as the ratio between the power at the maximum power point (mmp) and the product of J_{sc} and V_{oc}:

$$FF = \frac{J_{mpp}V_{mpp}}{J_{sc}V_{oc}} \qquad (2.14)$$

The energy conversion efficiency η of a solar cell is then defined as:

$$\eta = \frac{P_{mpp}}{P_{in}} = \frac{J_{mpp}V_{mpp}}{P_{in}} = \frac{V_{oc}J_{sc}FF}{P_{in}} \qquad (2.15).$$

In the dark, the current through a solar cell is given by equation (2.11) if the photon flux Φ equals zero.

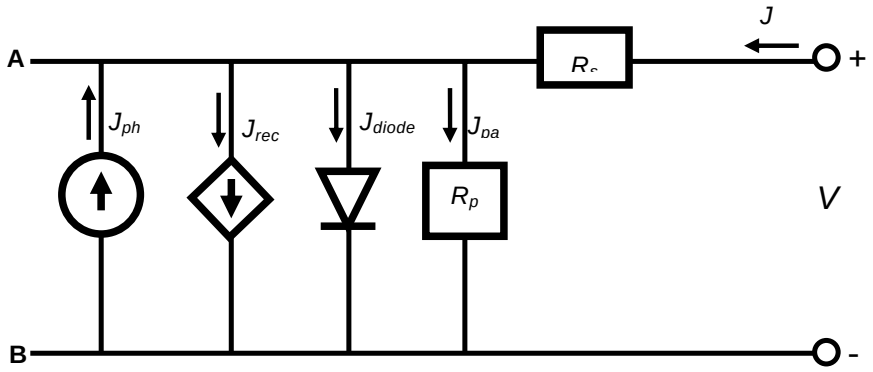

Fig. 2.7 An electrical equivalent circuit of a solar cell.

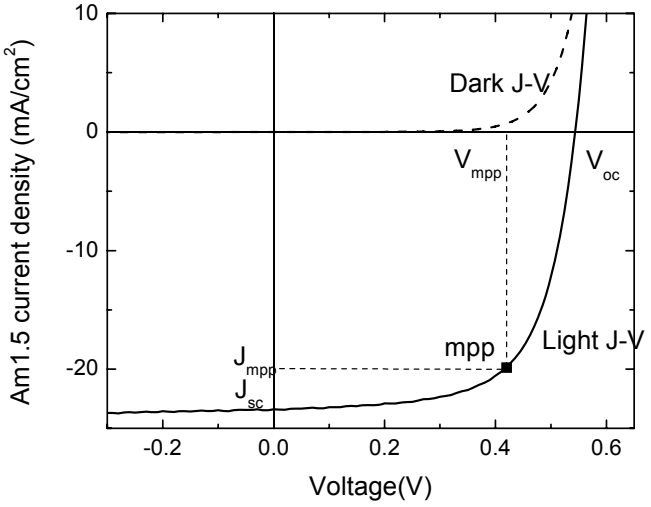

Fig. 2.8 AM1.5 *J-V* characteristics of an μc-Si:H n-i-p solar cell on a rough substrate.

The solar simulator

The *J-V* measurements involved in this study were performed with a WACOM dual beam solar simulator. It includes two light sources: a 1000 Watt xenon lamp for the UV and visible part of the spectrum (below 700 nm) and a 300 Watt halogen lamp for the infrared part. With help of a computer and a Keithley 238 source meter, an *J-V* curve can be obtained for a photovoltaic device. The parameters as described in the previous section can be derived from the dark and light *J-V* curves.

2.3.1.2 Accuracy of the current density estimation from the *J-V* measurements

The accuracy of the cell *J-V* measurement is limited by many factors. The deviation of the spectrum of the WACOM dual beam solar simulator from the AM1.5 spectrum is given in Table 2-4 for several wavelength regions. The accuracy of the reference cells used in the *J-V* measurement is also listed. The reference cells are built in a single module and are made of filtered crystalline silicon diodes. They have the response of c-Si, a-Si, SiGe/µc-Si and IR (no filter use). For each cell the *J-V* curve and spectral response has been determined, and were calibrated at NREL (National Renewable Energy Laboratories, Colorado US). By using these reference cells, the measurement error for J_{sc} is limited to ±3%.

The current density, *J*, is given as *I/A*, where *I* is the measured current at each given voltage, and *A* is the effective cell area, which is usually considered to be the area of transparent contact excluding the metal grids (for n-i-p cells) or the full area of the metal contact (for p-i-n cells).

The effective cell area under illumination can introduce some error in current density J, especially for small area cells (<1 cm^2). This is due to a side-collection effect which tends to give a higher current density when the contact area is small. When measuring the solar cell under an illuminated condition, not only the carriers (electrons and holes) that are generated below the contacts but also the carriers directly around the contacts are collected, mainly due to the high conductivity of the doped silicon layers. To reduce the amount of side-collected carriers, lab-size p-i-n cells are frequently made with an amorphous n-layer which normally has lower conductivity compared to the phosphorus doped µc-Si:H. This has been widely accepted as a standard configuration for lab-size p-i-n cells. In n-i-p cells, where the amount of side-collected carriers depends mainly on the conductivity of the p-layer, the use of a less conductive p-layer is not recommended, since it will influence the cell vertical collection as well (see the discussions in chapter 5). A way to avoid this side-collection is to limit the size of illuminated area to the contact area by using a shadow mask. However, due to the finite thickness of the mask and the accompanying shadow effect, the thus measured J_{sc} will be slightly underestimated.

One other effect that influences the accuracy of current density estimation for p-i-n cells is the light scattering (or absorption) by the thick glass which is normally used as the substrate for such cells. This effect, however, does not exist for the n-i-p cells, especially those made during our research, since the ITO/grid were directly in contact with air and no lamination was used throughout this study.

Table 2-4 Deviation of the WACOM dual beam solar simulator spectrum from AM1.5

Wavelength region (nm)	*Deviation from AM1.5*
400~500	+2%
500~600	-3%
600~700	-2%
700~800	-3%
800~900	-9%
900~1100	+14%
Reference cells calibrated at NREL	±3%

2.3.2 Spectral response measurement

Spectral response (SR) measurements of a solar cell are performed to obtain information about the response of the cell to light of different wavelengths. The cell is illuminated with a modulated monochromatic light beam, and the photocurrent $j_{ph}(\lambda)$ is measured with a lock-in amplifier.

A schematic drawing of the setup used in this study is shown in Fig. 2.9. In this setup, both the monochromatic beam and the bias beam are from the same Xenon lamp. For the standard measurement with white bias light, the bias beam is calibrated with the standard photo diode before each measurement in order to have a similar light intensity as that of AM1.5 sun light. Solar cell samples are mounted in an adjustable sample-frame with silver probes connected to the front and back contact. A bipolar power supply (Kepco) was used to give a DC bias voltage during the measurement. Data are collected via an IEEE interface card and recorded by a PC program called SRWin [21]. A typical wavelength step of 10 nm between each point is used.

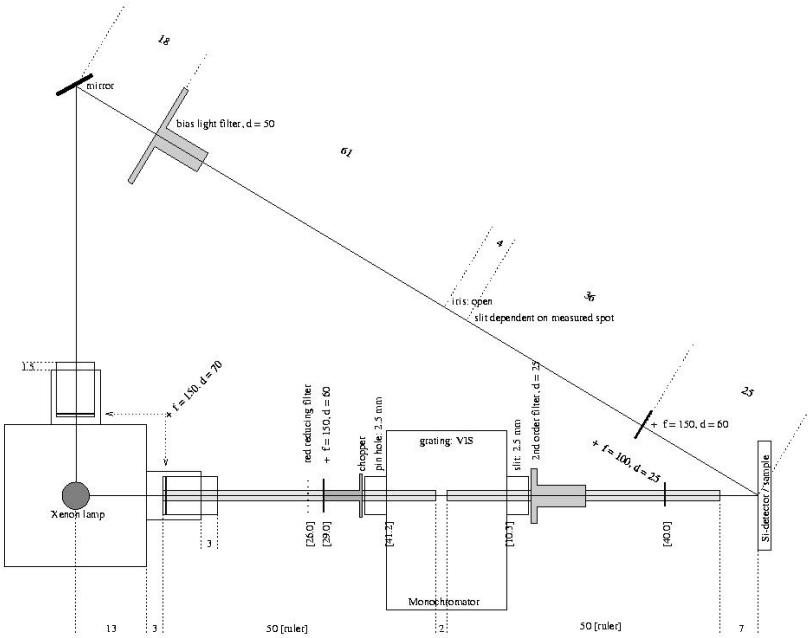

Fig. 2.9 Spectral response setup used during this study (Drawn by A. Gordijn)[22].

The external collection efficiency (*ECE*) is defined as

$$ECE = \frac{j_{ph}(\lambda)}{e\phi_{ph}(\lambda)} \qquad (2.16),$$

where $\phi_{ph}(\lambda)$ is the incident number of photons with wavelength λ per unit area per second. From the *ECE* the short-circuit current density J_{sc}^{SR} under AM1.5 conditions can be calculated by

$$J_{sc}^{SR} = e\int ECE(\lambda)\phi_{AM1.5}(\lambda)d(\lambda) \qquad (2.17).$$

This calculated value for the short-circuit current density correlates with the value obtained from AM1.5 *J-V* measurement, J_{sc}, but a deviation (up to 10%) may exists. This is dependent, among others, on the integration boundaries and the numerical integration procedure chosen in equation (2.17) [23].

For single-junction solar cells, the spectral response measurement is usually performed under short-circuit conditions. Due to the high density of electrical defects

normally existing in the silicon thin films, measurements performed under dark and illuminated conditions can be different, because of the trapping-related internal electric field modification. In order to compare the integrated J_{sc} values with those obtained from AM1.5 *J-V* measurements, a bias light with a similar intensity and spectrum to that of standard sun light is always necessary. Using a negative bias voltage, the internal electric field will increase, leading to a decrease of trapping and recombination of charge carriers. In most cases this results in an increase of *ECE*. At a certain negative voltage all charge carriers are collected, resulting in saturation of the external collection efficiency. The *ECE* obtained above this point can be defined as external quantum efficiency (*EQE*).

The spectral response of a tandem cell can also be measured. This is done by measuring the separate SR of the subcells. As the output current of each subcell depends on the amount of light it absorbs, one can use a filtered bias light to control which subcell gives the lowest current. Since all subcells are connected in series (Fig. 1.4), only the subcell that generates the lowest current will be measured. For instance, high energy photons (short wavelength light) will be mostly absorbed by the top cell, therefore a blue bias light will make the bottom cell current limiting; under a red bias light, the top cell will become current limited. As long as no other effect is involved (see section 7.1), the SR of a tandem cell measured without bias light (dark) is equal to the minimum of the two spectral responses of the subcells. Fig. 2.10 gives an example of the external collection efficiency of a tandem cell. In the case of measuring triple junction solar cells, the principle is the same; an appropriate bias light in order to separate the middle cell from the top and bottom cells is then needed.

One important issue for the measurements of multijunction solar cell is the use of a bias voltage. Namely, if no bias voltage is applied (short circuit condition), the voltage over each subcell is not zero and the subcells are not measured under short-circuit conditions. According to Kirchhoff's rules, for a triple junction cell,

$$V_{top} + V_{middle} + V_{bottom} = V \qquad (2.18),$$

$$I_{top} = I_{middle} = I_{bottom} \qquad (2.19).$$

Thus, by applying a bias voltage, the working point of the probed subcell (the current limiting cell) can be shifted to short-circuit conditions. The correct value of the bias voltage is approximately equal to the sum of the open-circuit voltage of the subcells that are not probed.

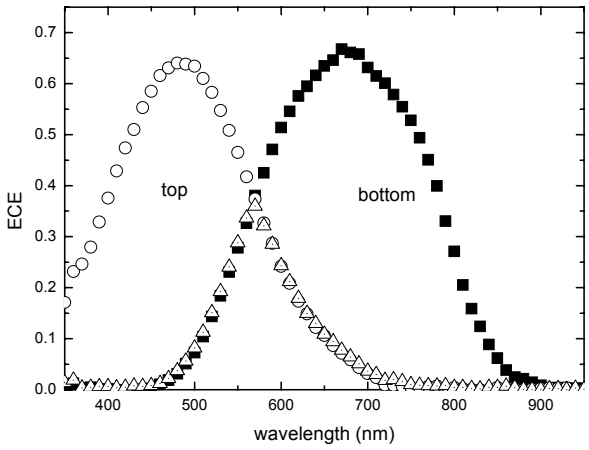

Fig. 2.10 External collection efficiency of the top cell (round dot) and bottom cell (square) of a tandem cell. Also plotted is the response of the tandem cell in the dark (up triangles).

References

1. R. Doyle, R. Robertson, G. Lin, M. He, and A. Gallagher, J. Appl. Phys. 64 (1988) 3215.
2. A.H. Mahan, Sol. Energ. Mat. Sol. C. 78 (2003) 299.
3. Shinya Tange, Keisuke Inoue, Kenichi Tonokura, Mitsuo Koshi, Thin Solid Films 395 (2001) 42.
4. Y. Nozaki, M. Kitazoe, K. Horii, H. Umemoto, A. Masuda, and H. Matsumura, Thin Solid Films 395 (2001) 47.
5. H.L. Duan, G.A. Zaharias, Stacey F. Bent, Thin Solid Films 395 (2001) 36.
6. J. K. Holt, *Hot-Wire Chemical Vapor Deposition of Silicon and Silicon Nitride for Photovoltaics: Experiments, Simulations, and Applications,* Ph.D. thesis, California Institute of Technology, 2003.
7. H. L. Duan, G. A. Zaharias and Stacey F. Bent, Mat. Res. Soc. Symp. Proc. Vol. 715 (2002) A15.5.7.
8. A. H. Mahan, J. Carapella, B. P. Nelson, R. S. Crandall and I. Balberg, J. Appl. Phys. 69 (1991) 6728.
9. M. Heintze, R. Zedlitz, H.N. Wanka, et al., J Appl. Phys 79 (1996) 2699.
10. A. H. Mahan, A. Mason, B. P. Nelson, and A. C. Gallagher, Mat. Res. Soc. Symp. Proc. Vol. 609 (2000) A6.6.1.
11. J.K. Holt, M. Swiatek, D.G. Goodwin, and H.A. Atwater, J. Appl. Phys. 92 (2002) 4803.
12. H.L. Duan, S.F. Bent , Thin Solid Films 485 (2005) 126.

13. P.A.T.T. van Veenendaal, O.L.J. Gijzeman, J.K. Rath, R.E.I. Schropp, Thin Solid Films 395 (2001) 194.
14. A. Gallagher, Thin Solid Films 395 (2001) 25.
15. E. Molenbroek, A. Mahan, and A. Gallagher, J. Appl. Phys. 82 (1997) 1909.
16. P. Ho, W. Breiland, and R. Buss, J. Chem. Phys. 91 (1989) 2627.
17. J. Perrin, J. Non-Cryst. Solids 137–138 (1991) 639.
18. K.F. Feenstra, *Hot-wire chemical vapour deposition of amorphous silicon and. the application in solar cells,* PhD thesis, Utrecht University, the Netherlands, 1998.
19. M. van Veen, *Tandem solar cells deposited using hot-wire chemical vapor deposition,* PhD thesis, Utrecht University, the Netherlands, 2003.
20. S. M. Sze, Physics of Semiconductor Devices, 2nd Edition. John Wiley & Sons, 1981.
21. SRWin was developed in Utrecht University by Ruurd Lof, Utrecht University
22. Introduction of spectral response setup, lab document, Utrecht University.
23. Detailed comparison of the J_{sc} values obtained from SR and *J-V* measurements requires a separate Chapter, which is not in the scale of this dissertation. Readers who are interested in this topic are suggested to read the literature, or contact the author Hongbo Li, or his colleague Robert L. Stolk, and ask for their unpublished work conducted in year 2003.

3

Structure defects caused by rough substrate and its influence on the performance of μc-Si:H n-i-p solar cells

3.1 Introduction

Due to the indirect energy band gap of crystalline silicon, the optical absorption coefficient (α) of μc-Si:H is one or two orders of magnitude lower than that of amorphous silicon. A much thicker i-layer is, therefore, needed to absorb most of the incident light. In a multi-junction solar cell, the bottom cell receives mostly photons with lower energy, in the range of 1.1 eV to 1.5 eV, for which α is normally below 1000 cm^{-1}. For photons with energy around 1.3 eV (wavelength 826 nm), the absorption coefficient is typically around 200 cm^{-1}. This means a light path of 50 μm is needed to absorb 63% ($1-e^{-1}$) of the total incident photons. The highest deposition rate reached so far for a near-device quality μc-Si:H i-layer is in the order of 1 nm/s. With this deposition rate, a 50 micron μc-Si:H i-layer would take around 14 hours. The deposition would take a few days with the deposition rate of a few angstroms per second, which is the rate used by

most of the labs to produce a high quality μc-Si:H i-layer. For this reason, it is essential to have a sufficient light trapping in a μc-Si:H solar cell.

In the past few years, considerable effort has been put into the development of substrates with a suitable rough surface for μc-Si:H solar cells. The structures mostly studied include conventional tin oxide, newly developed acid etched zinc oxide (ZnO), and Ag/ZnO double layers. At Utrecht University, we develop silver layers with proper roughness and cover them with a thin ZnO layer to enhance the surface reflection at the back side of a μc-Si:H solar cell. We have developed a method to control the surface morphology of Ag layers in both the vertical and lateral direction in order to obtain a maximum current for μc-Si:H n-i-p cells [1]. We found that surface plasmon absorption of a textured Ag layer is one of the limiting factors to the current enhancement of a μc-Si:H solar cell. Moreover, we showed improved correlation between the enhanced red light absorption and the substrate surface *rms* roughness by introducing a weighting factor based on the power spectral density analysis of substrate surface morphology [2]. The aim of the current study is to further analyze the influence of the Ag/ZnO rough substrate on the structure of silicon layers in μc-Si:H n-i-p cells, and to interpret the observed correlation between solar cell *J-V* parameters and the substrate surface *rms* roughness.

The structure of this chapter is arranged in the following way. First we show our experimental result for solar cells made on Ag/ZnO coated stainless steel (SS) with very high surface roughness (very large Ag grains). We focus our discussion on the dependence of the number of the working cells (the yield) on substrates with Ag layers made at different substrate temperatures, and show our findings on the existence of a critical n-layer thickness for having a reasonable yield on those substrates. Then we turn our discussion to the dependence of cell *J-V* characteristics, namely the open circuit voltage (V_{oc}), the dark saturation current density (J_0) and the diode quality factor (n), on the substrate *rms* roughness for a series of cell samples deposited on Corning glass/Ag/ZnO substrate with surface morphology controlled by introducing AlO_x inhibitors during Ag sputtering. We focus our discussion on the possible reasons that cause the near linear correlation between $\log(J_0)$ values and substrate *rms* roughness estimated from the AFM topographic pictures of each substrate used. We used various techniques to figure out what is the most probable reason that explains this J_0-*rms* relation, and compare to what has been published in the literature. Then, we switch to the discussion of Si growth on a rough Ag/ZnO surface, and try to find a clue on how to avoid the deteriorative effect of a rough substrate while maintaining a sufficient light trapping. In the end of the chapter, we give a complete diagram on the structure of μc-Si:H n-i-p cells deposited on a rough Ag/ZnO coated substrate.

3.2 Experimental details

Series of solar cell samples were made on Ag/ZnO substrates with various degrees of surface roughness. The cell structure is substrate (stainless steel or Corning 1737 glass) /Ag/ZnO/n-type μc-Si:H/1.3 μm μc-Si:H/p-type μc-Si:H/ITO/metal grid. Except for the surface roughness of the Ag/ZnO coated substrates and a few modifications on the n-layer, the deposition conditions of all other layers (including the silicon layers, ITO and metal grids) are identical. Intrinsic μc-Si:H layers were deposited by hot-wire CVD with a SiH_4/H_2 gas flow ratio of 5/100. Doped layers were deposited by PECVD. Ag and ZnO layers were made by RF magnetron sputtering. The roughness of the silver layers was tuned by varying the substrate temperature during Ag sputtering. A detailed description of the technique and the deposition conditions for Ag and ZnO layers can be found in reference [1]; parameters for hot-wire i-layer deposition are listed in Table 3-1. Thickness of the doped Si layers was estimated by means of optical fitting to reflection and transmission measurements for material samples separately deposited on glass substrates; that of μc-Si:H i-layer was estimated by earlier determination of the deposition rate and the deposition time. The i-layer thickness estimations were calibrated with cross-sectional TEM pictures of solar cell samples, and were found to be within 5% accuracy.

Table 3-1 Parameters for hot-wire CVD microcrystalline silicon i-layers deposition.

Filaments used	two 15- cm long tantalum wires, 0.5 mm in diameter
Filament temperature	1850 ºC (pre-deposition, measured in vacuum)
Filament to substrate distance	~4 cm
Substrate temperature	~ 250 ºC

J-V characteristics of all the samples were measured automatically with our well-calibrated XY-Table. In order to have a precise definition on the cell area, the sample strips were covered with a 0.3 mm thick stainless steel mask while doing the AM1.5 *J-V* measurement. The same mask was also used for sputtering the ITO top contact.

Rms values and the lateral feature sizes of Ag/ZnO surfaces were estimated from the AFM pictures measured on each substrate. The structural and electrical properties of the solar cell samples were investigated by using characterization techniques such as *J-V*, spectral response, Raman, and cross-sectional TEM examination. Raman measurements were performed with the laser beam (wavelength 514 nm) incident on the p side of the sample on the area without ITO coating. Cross-sectional TEM samples were prepared on

samples made on glass substrates with a method described in Chapter 4; a Philips Tecnai12 transmission electron microscope was used. Unless mentioned otherwise, all comparisons are for cells on the centre of the substrates (cells at the G, H and I columns) to avoid the influence from cell thickness variations at different sample positions. In a few cases, cells at a position near the edge of the substrate strips are also compared. In these cases, the influence from the sample position differences is minimized by comparing cells with the same column name [see Chapter2, a short description of the masking system used in our lab].

3.3 The yield of μc-Si:H n-i-p cells deposited on very rough Ag/ZnO substrates

3.3.1 Definition of the yield of properly working cells on each solar cell sample

Before discussing the influence of the substrate on cell *J-V* properties, it is necessary to introduce a definition for the yield of working cells. The electrical shunting of a solar cell can be generally described by introducing a parallel resistance (R_p) that connects two opposite contacts, as described in Chapter 2. It has been shown by M. van Veen that the fill factor (*FF*) of a solar cell directly relates to the differential resistance (R_{scD}) deduced from the dark *J-V* characteristics of solar cells at zero bias voltage, namely $R_{scD} = (dV/dJ_D)_{V=0}$, where J_D is the dark current density. For the proto-Si:H n-i-p samples made in our system, cells with a R_{scD} less than 10^2 Ωcm^2 are completely short circuited [3]. Since the dark *J-V* for some of our μc-Si:H solar cell samples were not recorded, we define the yield based on the R_{sc} Values calculated from the AM1.5 light *J-V* characteristics at zero bias voltage, namely $R_{scL} = (dV/dJ_L)_{V=0}$, where the letter *L* stands for the light *J-V* measurement. We note that the differential resistance R_{sc} was often called R_p in some of our earlier publications [1]. Fig. 3.1 shows a correlation between R_{scL} and cell fill factor (*FF*) under AM1.5 illumination for a few different solar cell samples. It can be seen that cells with R_{scL} below around $R_{scL1} = 30$ Ωcm^2 are short circuited (with $FF \sim 0.25$), whereas for cells with $R_{scL2} = 300 \sim 1000$ Ωcm^2, the *FF* becomes saturated. The exact value of R_{scL1} and R_{scL2} varies for different cell types (a-Si:H and μc-Si:H cells) and substrates used (plain SS and SS with rough Ag/ZnO). Since the amount of shunted cells with R_{scL} close to R_{scL1} is generally much less than those with R_{scL} close to R_{scL2}, we chose $R_{scL} = R_{scL1} = 30$ Ωcm^2 as the critical value to judge if a cell is short circuited or not. Therefore,

$$yield = \frac{the\ number\ of\ cells\ with\ R_{scL}\ greater\ than\ 30\ \Omega cm^2}{the\ total\ number\ of\ cells} \tag{3.1}$$

As can be seen from Fig. 3.1, this definition has essentially the same function as defining the yield as the ratio of the cells with *FF* greater than around 0.27.[1]

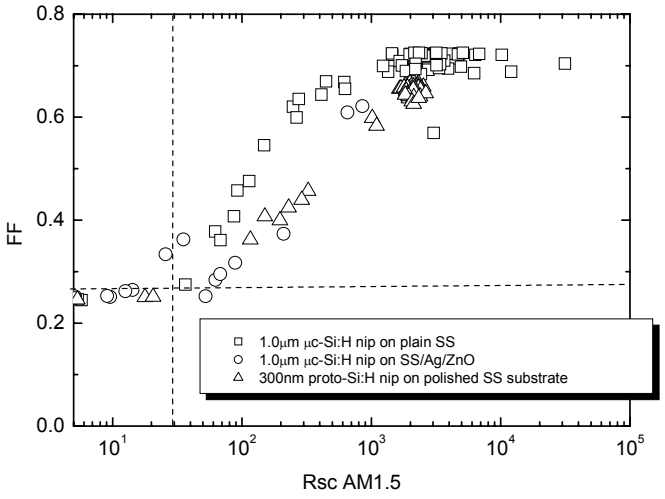

Fig. 3.1 *FF* vs R_{scL} for a few n-i-p cells made on different substrate.

3.3.2 Shunting of μc-Si:H cells made on SS/Ag substrates with high surface rms roughness

At the beginning of our research, the μc-Si:H n-i-p solar cell samples made on rough Ag/ZnO substrates all showed a serious shunting problem. The conditions that were used to make excellent μc-Si:H n-i-p cells on plain stainless steel substrates [4] did not result in good cell performance on rough substrates. Table 3-2 shows the light *J-V* characteristics of such a sample; as a reference, the parameters for a cell made on plain stainless steel substrate are also shown. One can see that except for the increase in the short circuit current density due to enhanced light trapping, all other parameters of the cells made on the stainless steel substrate with a 500ºC Ag layer showed serious deterioration; the yield of this sample was only 12%. The dramatic difference between

[1] Using a *yield* definition based on R_{scL} or R_{scD} , one can avoid the difficulty of defining *yield* of the cells showing S-shape in their light *J-V* characteristics, since the *FF* for such cells are typically lower then 0.25.

the performances of the cells made on the two substrates is also shown in Fig. 3.1 by open squares, for the cells made on plain SS, and by open circles, for the cells made on SS coated with rough Ag/ZnO.

Table 3-2 AM1.5 *J-V* characteristics of two µc-Si:H samples made in the same Si deposition condition but on different substrates. Numbers are the average values for 10 best cells on each substrate.

Substrate type	*Eff. (%)*	J_{sc} (mA/cm^2)	V_{oc} *(V)*	*FF*	R_{scL} (Ωcm^2)	*Yield (%)*
SS with 1 µm 500ºC Ag and 100 nm ZnO	2.02	18.2	0.282	0.316	125	11.9
plain SS	4.71	12.6	0.520	0.721	3115	91.7

As a basic requirement for a short circuited cell, direct connections between two electrical contacts must exist. Whether these are the pin holes or cracks or some other shunting paths was unknown, nevertheless, we believed that it was related to the rough Ag/ZnO substrate. Besides, since the shunting path must go through the more than 1 µm thick i-layer, the silicon deposition condition may also have an influence.

3.3.3 Influence of the n-layer thickness on the yield of working cells

Optimization started from varying the Ag and ZnO deposition conditions. It was found that variations on the thickness and the deposition condition of ZnO did not result in significant improvement on the yield of the working cells, whereas a decrease in the substrate setting temperature during the Ag sputtering gave encouraging result. Moreover, the yield of working cells on each substrate seems to have a direct connection with the thickness of the n-layer used. Fig.3.2 gives an overview of the cells that were made on SS/Ag/ZnO substrates with Ag layers deposited at two different substrate temperatures (425 ºC and 325 ºC). In both cases, an optimal n-layer thickness exists at about 27-30 nm. For the cells with an n-layer thickness on either side of this optimum, the yield decreases, and is especially pronounced for those made on the substrate with Ag layers prepared at a high temperature. Fig.3.3 further depicts the influence of Ag deposition temperature on the yield, in which all cells were made with exactly the same conditions for the silicon layers as well as the ZnO and ITO layers. Clearly, at the optimized n-layer thickness, the yield is still influenced by the Ag deposition temperature. In the next section, we elaborate on the possible causes for these effects.

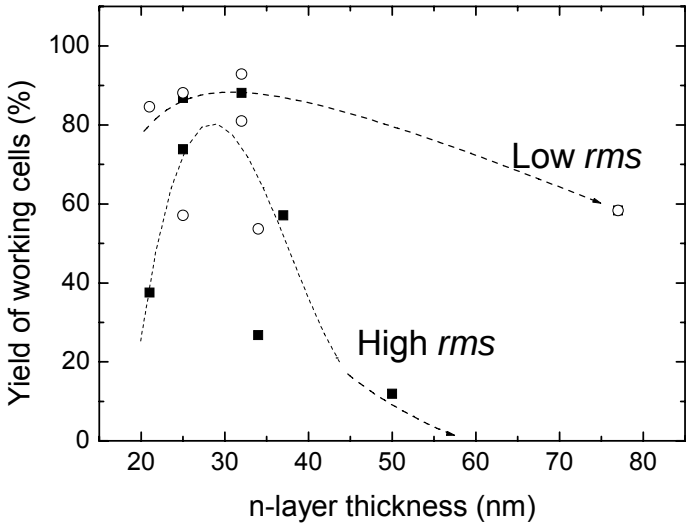

Fig.3.2 Dependence of the yield of working cells of μc-Si:H n-i-p sample on n-layer thickness. Lines are guides to the eyes.

3.3.4 Hollow area in the silicon layers and its influence on the yield of working cells

It has been shown that sputtered Ag has a polycrystalline structure; the higher the substrate temperature is, the larger the crystal grains tend to be, so is the Ag surface *rms* roughness [1]. For cells deposited on substrates coated with Ag layers sputtered at the lowest substrate temperature, with a substrate surface *rms* roughness around 34 nm, the yield reaches 100%. Now the question is why this Ag roughness influences the yield. Answers to this question come from the morphology study on the substrate surface. Fig.3.4 shows the SEM picture of a Ag layer sputtered on plain stainless steel at a substrate temperature of 425 ºC. We can clearly observe a structure of large embedded crystal grains with acute surface angles to the substrate. Such a substrate is known to form holes that are not filled by the succeeding depositions (ZnO and Si) due to the shadowing effect of these large grains. The cross-sectional TEM picture shown in Fig.3.5 indeed confirms the existence of such a hollow areas, although the Ag layer for the sample shown in this figure was made at a somewhat lower temperature due to the different substrate used (Corning glass instead of SS). Although the Ag grains can not be easily recognized due to the relatively low contrast in the picture around that area, we can clearly see a large cavity of the order of a hundred nm that is not completely filled by silicon. Cavities with this size create locations for storing impurities such as water vapour and oxygen. More seriously, as can be seen from Fig.3.5, there are stripe-like

voids formed in the silicon layers on top of this area, through which the sputtered ITO front contact might make direct connection to the Ag/ZnO layer, and therefore, could create short circuit paths for the n-i-p junction. The cause for the formation and development of these stripe-like voids will be discussed in more detail in the next section; here, we discuss only the possible consequence of the voids significant in size as shown in Fig.3.5.

If we assume that the long voids that connect the front and back contacts of the solar cell have a size of 1 μm in length and 100 nm in diameter, and that the material inside the voids is ITO with an electric resistivity of 3.0×10^{-4} Ω cm, then the resistance resulting from one of these filled voids is around 400 Ω. If we denote the average density of these voids as m cm^{-2}, the average areal shunting resistance Rp will be around $400/m$ Ωcm^2. As we discussed earlier, for a μc-Si:H cell showing completely shunting behaviour in its J-V characteristics, the R_{scD} is in the order of 100 Ωcm^2 or lower. Since R_{scD} can, to a large extend, be regarded as Rp, the minimum of value m that required to shunt the whole cell (m_{sh}) is then 400/100 = 4 (cm^{-2}). That is to say, to short-circuit a microcrystalline n-i-p cell, 4 of these voids per cm^2 are enough. The sample shown in Fig.3.5 clearly has a larger amount of voids, and indeed is found to have a low FF. Fig.3.6 shows the simulated dependence of the density m on the average size of the shunting voids based on the assumption given above. In the cases that these voids are not fully filled with ITO, or the conductive element is not from ITO but some material with a lower conductivity, the minimum requirement for m will increase. However, as long as there is a wide distribution in the size of the voids, there are always chances that the cells are shunted.

Our experimental result showed that for substrates with the Ag layer made at a temperature higher than 350 ºC, and with an average Ag thickness around 1 micron, most of the cells were shunted. The J-V characteristics of such cells were typically a straight line. This can then be explained by a high density of wide shunting paths present in these cells.

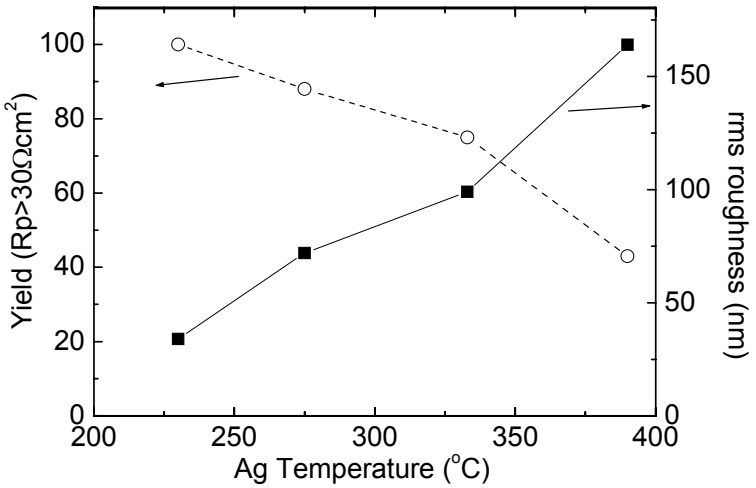

Fig.3.3 Dependence of yield of working cells on Ag substrate temperature. Cells were made with a n-layer thickness of 32 nm**.**

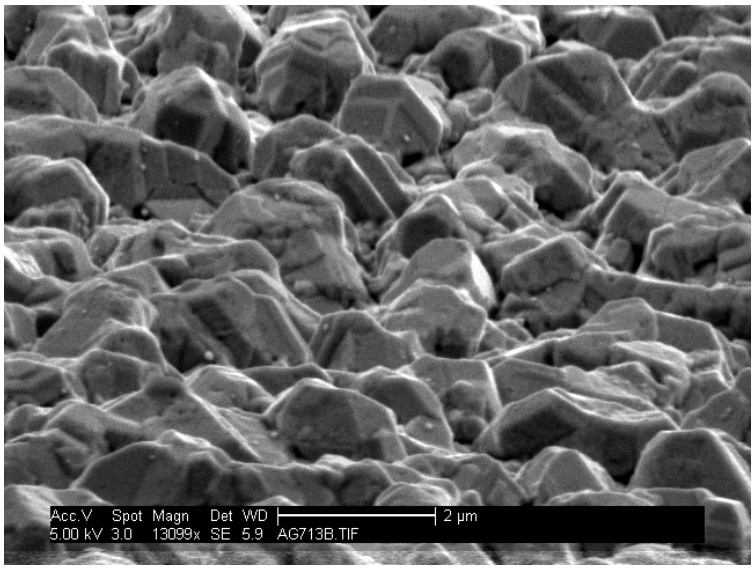

Fig.3.4 SEM picture of the surface of a sputtered Ag layer at a substrate temperature of 425 ºC.

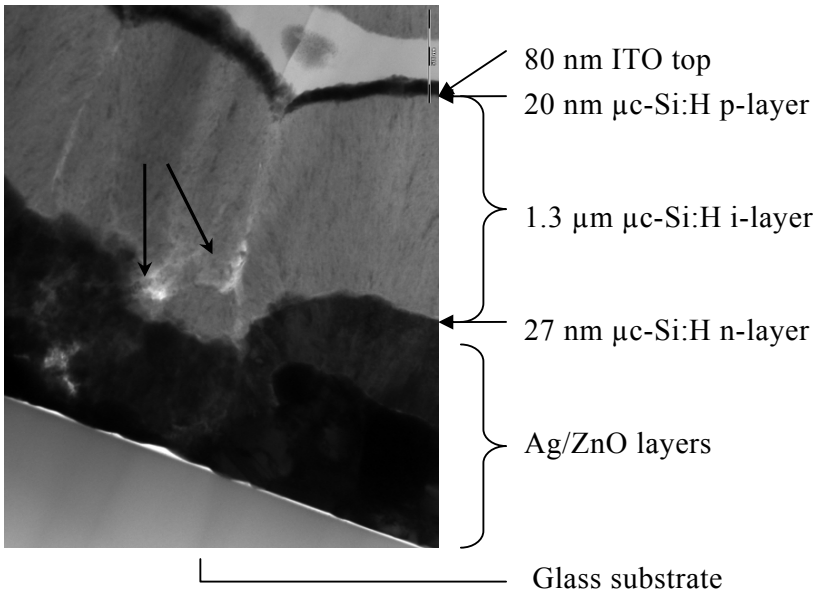

Fig.3.5 Cross sectional TEM picture of a μc-Si:H n-i-p solar cell deposited on Corning glass with a rough Ag/ZnO surface. The substrate temperature during the Ag sputtering was around 325 ºC. The i-layer thickness is around 1.3 micron. The arrows point to the cavities that not completely filled by silicon. The scale bar shown in the picture is 500nm

.

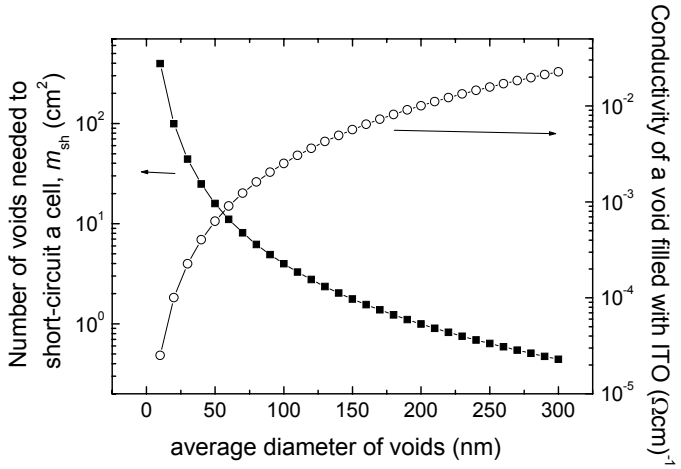

Fig.3.6 The simulated dependence of the density m_{sh} on the average size of the shunting voids filled with ITO with a conductivity of 3×10^4 S/cm.

3.4 Dependence of V_{oc} on the surface rms roughness of Ag/ZnO substrates

To sufficiently improve the yield of solar cells, the target for the Ag sputtering deposition was changed from pure Ag to a mixture of Ag and Al. During the sputter deposition, oxygen was introduced into the system, and as a result AlO_x was formed in the layer. The small amount of AlO_x acts as an inhibitor for Ag crystal growth. Consequently, growth of large Ag grains was suppressed and the hollow areas in the silicon layers deposited afterward were avoided. Optimization of the sputtering process of Al doped Ag deposition has been performed earlier in our group [1]. Here we discuss the influence of Ag/ZnO surface morphology on the structural and electrical properties of μc-Si:H solar cells

.

3.4.1 Experiment and results

3.4.1.1 Samples used in this study

Ten pieces of Corning 1737 glass/Ag/ZnO substrates were prepared, each with a different surface *rms* roughness varying from 13 nm to 135 nm. Due to the limited deposition area in PASTA and the un-optimized homogeneity for the hot-wire i-layer, the solar cells were made in 5 deposition runs, each with two of these substrates. The samples were, therefore, divided into 5 groups. Table 3-3 lists the surface parameters of these substrates, as well as the data for an Ag (200 nm) /ZnO (100 nm) coated Asahi U-type glass as a reference. The AFM images of 4 of these substrates are shown in Fig. 3.7.

Table 3-3 substrate parameters derived from 10 μm by 10 μm AFM images.

Group	*Sample name*	*substrate*	*Rms (nm)*
A	A_1	S_A_1	73
A	A_2	S_A_2	133
B	B_1	S_B_1	13.4
B	B_2	S_B_2	88.2
C	C_1	S_C_1	61
C	C_2	S_C_2	111
D	D_1	S_D_1	67
D	D_2	S_D_2	135
E	E_1	S_E_1	83
E	E_2	S_E_2	92
R	R	Asahi_U	32

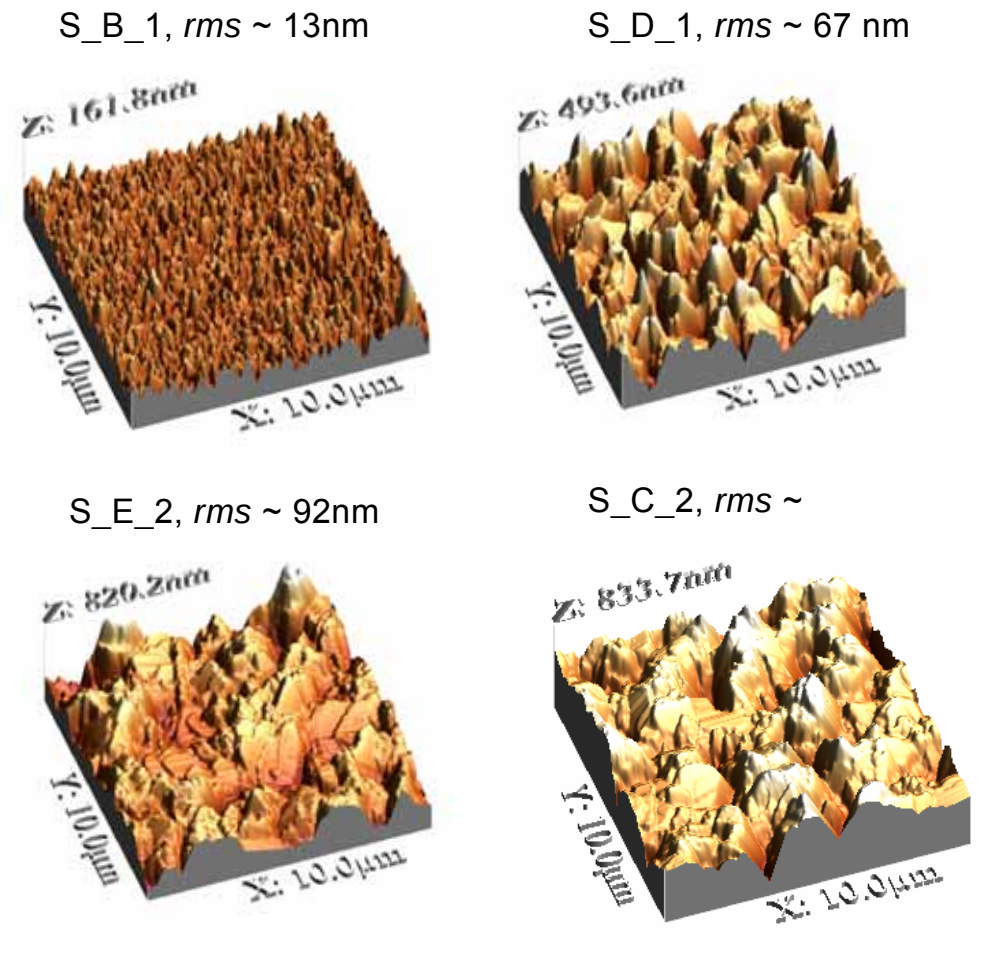

Fig. 3.7 AFM pictures of glass/Ag/ZnO substrate with different surface roughness.

3.4.1.2 Electrical properties: Substrate surface *rms* roughness dependence of open circuit voltage (V_{oc}), diode quality factor (n) and dark reverse saturation current density (J_0)

Fig.3.8a shows the dependence of the AM1.5 open circuit voltage (V_{oc}) on the substrate *rms* roughness. For the samples made under identical conditions, a clear trend of decreasing V_{oc} with increasing *rms* roughness exists. The samples with their data point surrounded by a circle (group A) were made with a profiled n-layer consisting of a two-step deposition: the first step consisted of standard n-type a-Si:H deposition conditions with a thickness of around 5 nm, and the second of those of n-type μc-Si:H, around 27 nm thick. From Fig.3.8a, it is clear that this group of samples shows higher V_{oc}. Fig.3.8b and Fig.3.8c give the values of the reverse saturation current density J_0 and the diode quality factor n deduced from the dark J-V curves. For all the 10 samples studied, the

trends of the observed increase in both parameters as a function of the *rms* roughness are clearly visible, although the samples in group A show somewhat lower J_0 and higher n values than that of the other samples with a similar substrate *rms* roughness.

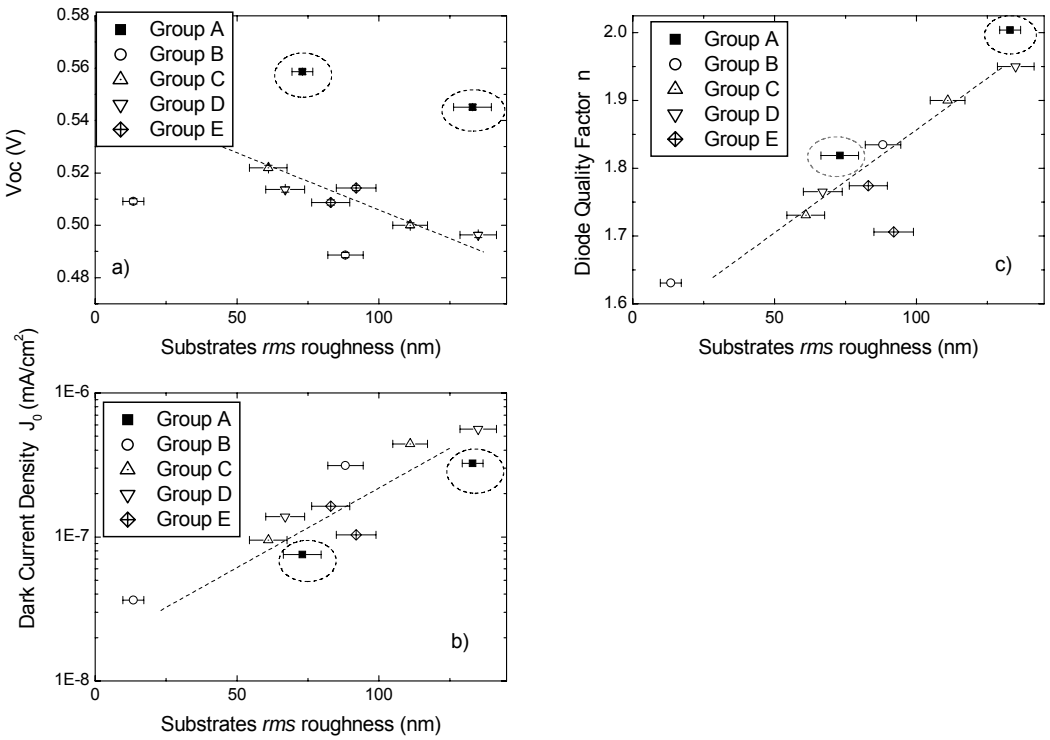

Fig.3.8 Correlations of V_{oc}, J_0 and n of working cells with substrate surface roughness *rms* value. Points in the dashed circles are cells made with a double n-layer. Lines are guides to the eyes.

To study this remarkably clear correlation between Ag/ZnO substrate surface roughness and the solar cell *J-V* characteristics, especially the J_0 and n values, the samples are compared within each group. In this way, we can minimize the possible influence from any run to run variation of the deposition parameters in the PASTA system.

Fig.3.9 presents the *J-V* characteristics, namely V_{oc}, *FF*, J_0 and n values, of the samples with a profiled n-layer. The *rms* roughness of the substrates used for these two samples are estimated to be around 73 nm and 133 nm. Instead of presenting only the parameters of the best cell on the centre of the sample strips, Fig.3.9 shows, for each sample, the characteristics of all the cells in the same row. Clearly, the cells on the

rougher substrate show inferior cell parameters. Moreover, except for a few short-circuited cells, the parameter differences between the cells are almost constant at all Y position. This constancy against cell position variations also exists for the samples in the other groups, which clearly indicates that the observed *rms* roughness dependence of cell *J-V* parameters is *not* originated from the non uniformity in the hot wire i-layer deposition.

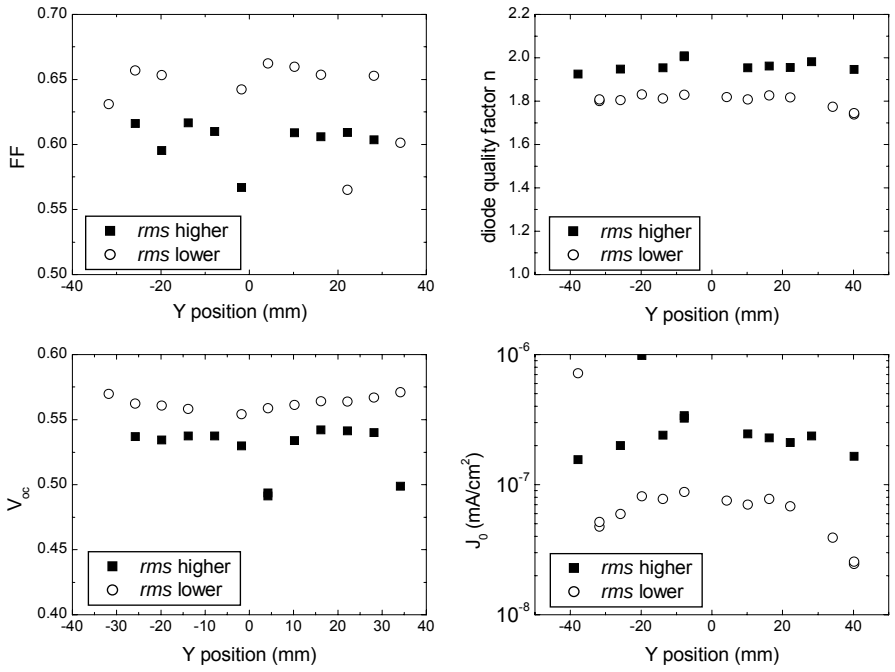

Fig.3.9 AM1.5 *J-V* characteristics of the two solar cell samples in Group A, on substrate S_A_1 (open circles) and on substrate S_A_2 (solid squares). They were made in the same PASTA run but on substrates with different roughness.

3.4.1.3 Structural properties

TEM examination: Stripe-like area in the µc-Si:H i-layer

Fig.3.10 shows the bright field TEM pictures of the two samples in group A. The substrate *rms* roughness for these two samples are 73 nm (a) and 133 nm (b and c), respectively. In the pictures of the sample made on the rougher substrate, one can clearly see low density lines appearing in the silicon layers and also in the ZnO layer. Those lines, or the stripe-like areas, are the place where very few or no atoms are present in the atom network during the layer growth. Some of these stripes have a diameter of ~ 100 nm

(as that shown in Fig.3.10c), which is wide enough to form a micro shunting path between the front contact (or p-layer) and the Ag/ZnO back contact. As a reference, Fig.3.10d shows the structure of a sample deposited under the identical condition but on a substrate with a nearly flat Ag/ZnO substrate (*rms* ~4 nm). Clearly, no stripes can be observed in that sample.

Stripe-like areas with various sizes are observed in the TEM pictures of many of the examined samples in this series, and they can be classified into two categories: 1). those that start in the ZnO layers; 2). those that start in the silicon layers. For the stripes that already appear inside the ZnO layer, it is often observed that the stripes become a hollow area in the silicon layers; whereas for those that start in the silicon layers, it is often hard to distinguish whether they are hollow or are filled with some silicon atoms with a low atom density, since the diameter of these stripes are often smaller (below around tens of nanometres).

One common feature of these two types of stripes in this series of samples is that once being formed they develop along the Si growth direction toward the top surface of the n-i-p structure, with a tendency to decrease in diameter, which is defined as the width of the stripes estimated from the TEM picture. Some of the stripes with a small width show closure near the top surface, although the collision of silicon columns can still be clearly seen.

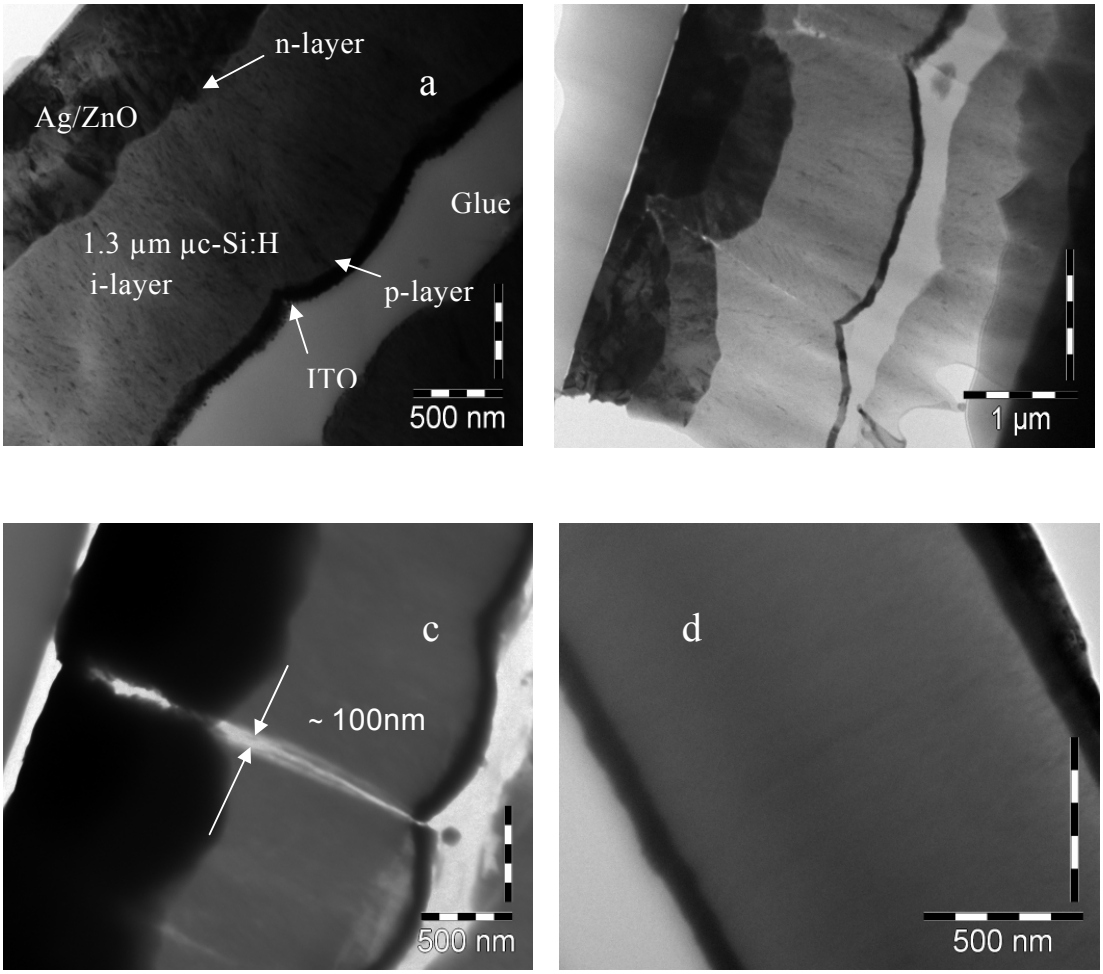

Fig.3.10 Cross sectional TEM pictures of µc-Si:H n-i-p cells made on Ag/ZnO coated Corning 1737 glass. a) sample S_A_1, b) sample S_A_2, c) another picture of sample S_A_2 for cracks study. d) a µc-Si:H n-i-p sample made on a nearly flat Ag/ZnO substrate with a substrate surface *rms* roughness of ~ 4 nm. The total thickness of the silicon layers in all the samples are around 1.3 µm.

Raman spectroscopy examinations

A common explanation for the V_{oc} difference of µc-Si:H cells is the difference in the i-layer crystallinity. The most straightforward way to check the i-layer crystallinity is by means of the Raman scattering spectroscopy at one side of the sample. Due to the limited penetration depth of the excitation light, this, however, only gives the structural information in the upper most part of the layer stack. Fig.3.11a shows the normalized Raman scattering spectra for samples in group B, D and E, where the substrate *rms* roughness varies from 13.4 nm to 135 nm. The spectra were taken employing with a 514.5 nm wavelength Argon laser beam incident from the p-side of the sample, on the area without the ITO coating. The penetration depth for light with this wavelength is

around 200 nm for a μc-Si:H material, therefore the Raman spectra give structure information on the whole p-layer (~ 20 nm thick) and the top part of the i-layer. Except for a small shift in the peak values, due to the different calibrations between measurements, the normalized intensity for all the samples exactly overlap. For the two samples made with a double n-layer (group A, shown in Fig.3.11b), the Raman spectra show clearly higher intensity in the spectral range between 400 cm^{-1} and 510 cm^{-1} than the rest of the samples (represented by sample B_1), which indicates a higher amorphous content for this group of samples. Again, no difference can be observed between the two samples in that group.

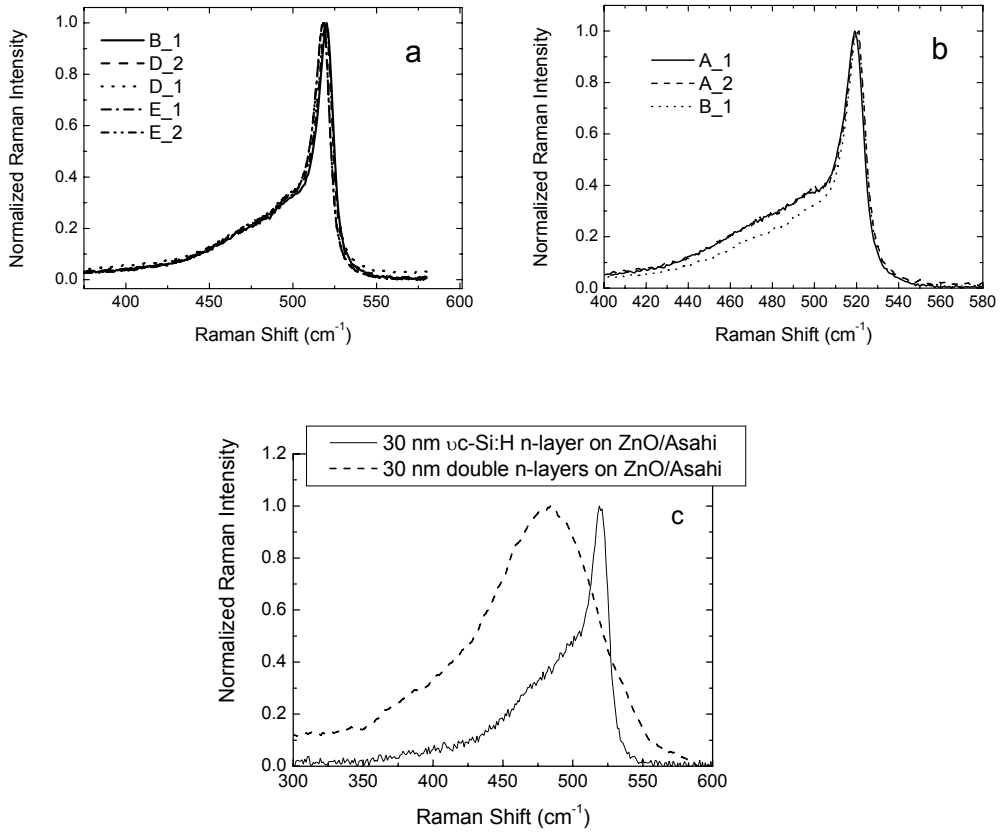

Fig.3.11 Raman scattering spectra on the p-side of: (a) the samples with a single n-layer, (b) the samples with a profiled n-layer. (c) Raman spectra of a ~30 nm thick double n-layers deposited on a ZnO/Asahi glass substrate (light grey line), and of a ~30 nm thick single n-layer on ZnO/Ag/Corning substrate (black line); the substrate signal has been subtracted.

3.4.2 Discussion: possible reasons for the V_{oc} deterioration for solar cells developed on rough Ag/ZnO substrates

3.4.2.1 Connection between J_0, n, and V_{oc}

As we will discuss in the following chapters, the V_{oc} of a thin film silicon p-i-n (including n-i-p) diode has a fundamental connection with the diode quality factor n and the dark saturation reverse current density J_0 [equation 5.3]. If there is no carrier transport barrier between the doped silicon layers and the contacts, such as the barrier found at the interface between ITO and the p-type μc-Si:H layer [see Chapter 5], the J_0 and n values deduced from the dark J-V characteristics give information on the quality of the silicon layers and their interfaces. In these cases, the increase of the diode quality factor indicates an increase of carrier recombination in the bulk of the i-layer.

3.4.2.2 Issues related to the influence of shunting paths on the value of V_{oc}

The high density of large voids observed in the TEM pictures of the samples made on rough substrates contribute to the low yield of working cells, as we have shown in section 3.3. But are they also responsible for the lower V_{oc} of those samples? To answer this question, quantification of the density of these shunting paths is necessary. It is known that the current that flows through the shunting paths has a linear correlation with the bias voltage, and it contributes to a large extent to the differential resistance (R_{sc}) deduced from the J-V characteristics of solar cells at zero bias voltage. This suggests us to use R_{scD} (R_{sc} deduce from the dark J-V measurement) to represent the density of those shunting paths[2]. To verify the validity of this representation, an R_{scD} versus *rms* roughness curve is shown in Fig.3.12. Clearly, R_{scD} decreases with the increase of the *rms* roughness. To estimate how much the influence from the i-layer recombination is, $R_{scdiode}$, which is deduced from the fitted diode Current Density – Voltage (J_{diode}-V) curve in the voltage range V > 0.2 V, was also shown. The n and J_0 of the J_{diode}-V curves are taken from the values shown in Fig.3.8b and Fig.3.8c. One can see, in the entire *rms* range, that the R_{scD} is more than 10 times smaller then $R_{scdiode}$, which confirms that the carrier recombination in the i-layer has a negligible influence on the R_{scD}'s of this set of sample.

Using this concept, namely R_{scD} is correlated to the areal density of the shunting paths in a cell, we study the R_{scD} dependence of V_{oc} for the two samples in Group A

[2] Besides the shunting paths, carrier recombination in the i-layer also contributes to the R_{scD}.

(Fig.3.13). It can be seen that for cells with R_{scD} below around 100 Ωcm^2, V_{oc} decreases linearly with decreasing R_{scD}, which indicates the dominance of shunting paths (with shunting resistance of R_{sh}) for those cells. For cells with R_{scD} higher than around 100 Ωcm^2, V_{oc} becomes saturated even though R_{scD} increases more than 2 orders of magnitudes, i.e. from around 100 Ωcm^2 to 2×10^4 Ωcm^2. The nearly 30 mV difference between the two saturated V_{oc} values, 0.54V and 0.57V for the higher and lower *rms* sample, respectively, indicates that R_{scD} is irrelevant to the V_{oc} difference between these two samples. That is to say, the difference in V_{oc} between these two samples is not due to the shunting resistance introduced by the different areal density of the observed shunting paths.

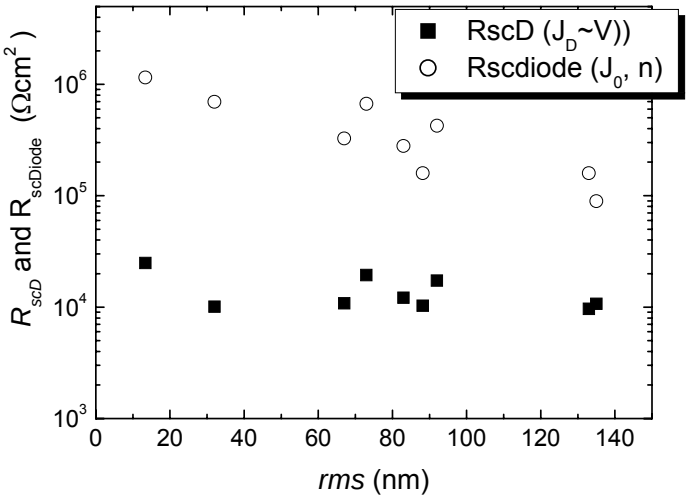

Fig.3.12 R_{sc} versus *rms* dependence for the best cell of the samples listed in **Table 3-3**.

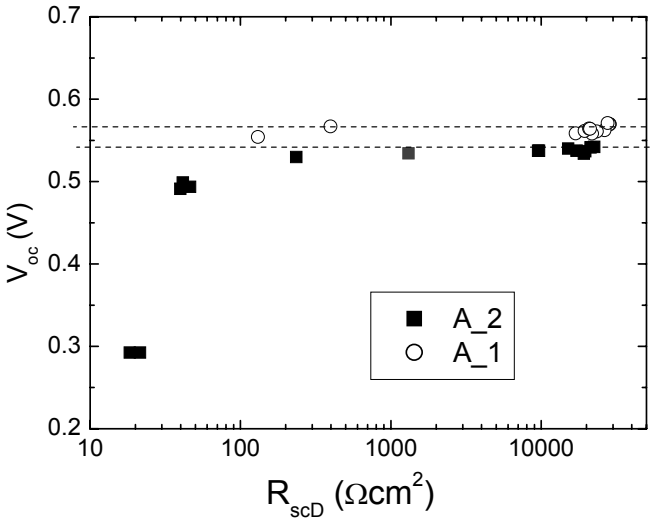

Fig.3.13 V_{oc} and R_{scD} dependence of the two cells in Group A.

3.4.2.3 Possible substrate *rms* roughness dependence of effective areas for J_0 calculation

The dark saturation current density J_0 were calculated by fitting the linear part of $\log(J_{dark}) \sim V$ curves, with an assumption that the effective area that electric current flowing through remains constant when the substrate surface roughness varies. However, the interface area through which carriers inject into the silicon layers are probably different in cells deposited on a smoother substrate than deposited on a rougher substrate. It is therefore possible that the relatively higher effective area of the cells on a rougher substrate increases the dark saturation current, which in turn results in a lower V_{oc} than on a less rough substrate. Since we have measured the substrate surface 3D profile by an Atomic Force Microscope (AFM), we can estimate the surface area of each substrate, and therefore, calculate to what extent this area enhancement influences the cell V_{oc}.

Fig.3.14 shows again the *rms* roughness dependence of J_0 (squares), but with additional data points where the J_0's were recalculated with the effective area integrated from the AFM picture for each substrate (triangles). Also shown in this figure are the J_0's obtained with a simulated area based on a pyramid assumption (illustrated in the inset of Fig.3.14) with the substrate lateral feature sizes and the *rms* heights as the input parameters (circles). Although the enhancements of the substrate effective area by a rough surface indeed result in a small increase on the J_0's, ~5% on average, it can be seen that the trend of increase in J_0 with substrate *rms* roughness is not at all influenced.

Further more, the fact that the diode quality factor *n* shows a similar trend with the substrate *rms* roughness (Fig.3.8c) confirms that the decrease in V_{oc} is not due to the substrate effective area variation; otherwise the *n* values would be more or less constant for this set of samples.

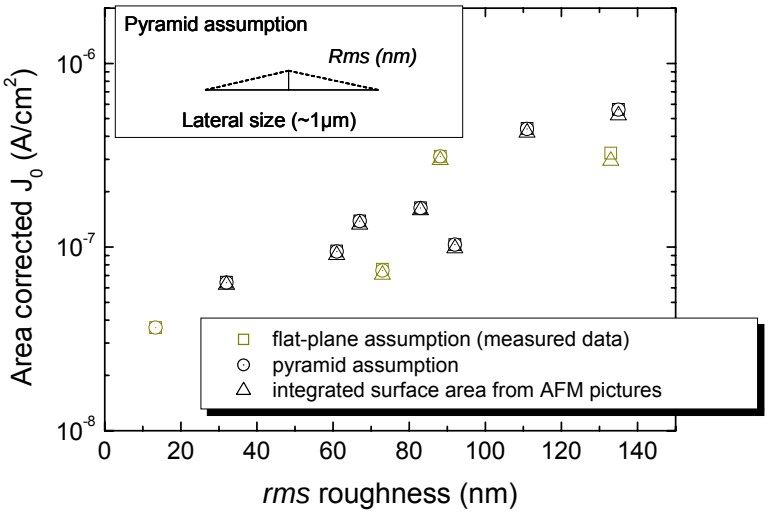

Fig.3.14 Substrate *rms* roughness dependence of the current density J_0, with the effective area estimated from flat-plane assumption (open squares, measured data), pyramid assumption (open circles) and the integrated surface area from the AFM pictures of Corning/Ag/ZnO substrate (open triangles).

3.4.2.4 Issues related to the possible differences in the crystallinity of the intrinsic μc-Si:H layers

The difference in crystallinity between samples in Group A (with double n-layer) and the samples in the other groups (B, C, D, E, with a single μc-Si:H n-layer) can be well explained by the influence of the seed layer (n-layer) on the growth of the μc-Si:H i-layer. In the past there has been a discussion on whether it is necessary to use a seed layer in a μc-Si:H solar cell (mostly for p-i-n cells) deposited on top of a doped μc-Si:H layer. The plots shown in Fig.3.8 and Fig.3.11 clearly demonstrate the strong influence of the crystallinity of the doped μc-Si:H layer on the development of intrinsic μc-Si:H layers. This indicates that control of the structure of the doped μc-Si:H is an important factor in the optimization of μc-Si:H solar cells. The conclusion drawn by some researchers that there is no need to use a seed layer for the growth of μc-Si:H i-layer has to be reconsidered in the context that the thin doped μc-Si:H layer (p or n type) already acts as a seed layer for the growth of intrinsic μc-Si:H.

As shown in section 3.2.1.3, the Raman scattering spectra did not show difference between samples in all the groups with substrate *rms* roughness (*rms*) variations in a wide range. This means that the observed correlation between V_{oc} and *rms* is not caused by the silicon crystallinity variations near the p/i region, including that of the p-layer and the top ~150 nm i-layer. To distinguish the difference in the crystallinity in the bulk of i-layers is, however, not possible at this stage. The best that we can do now is to compare the cross sectional XTEM pictures of the samples made on different substrates. Based on the pictures that we have obtained, we could not see any difference in crystallinity among samples in the groups B, C, D, E, and between samples within Group A. To completely rule out the possible influence of the crystalline volume fraction (X_c) variations in the bulk of the i-layer, further investigation is needed.

3.4.2.5 Possible influence from the p-type μc-Si:H layers

It can also happen that the p-layers which are intended to be μc-Si:H turn out to be amorphous in structure. This is due to the sensitivity of boron doped μc-Si:H to small variations in the deposition parameters and substrate conditions (see Chapter 5). Since the p-layer deposition conditions for this set of samples are the result of a thorough optimization, and all the samples have had a post annealing treatment in a N_2 atmosphere to improve the p/ITO/Ag top contact, the influence from this aspect is not considered to be an issue. Besides, the fact that Raman spectra obtained on samples in each group completely overlap also rule out the possible crystallinity difference in the structure of p-layer and p/i interfaces.

It is, however, possible that impurities, such as moisture, oxygen, or metals elements, can diffuse through the pinholes as were shown in the XTEM pictures, and cause changes in the electrical properties of the p/i interfaces. However, this is considered not to have been originated by the p-layer itself.

3.4.2.6 Summary of the factors influencing cell V_{oc}

Before going to the next session, we summarize our discussion on the possibilities that can influence the V_{oc} of the cells in this *rms* series in the list shown below.

Table 3-4 Summary of the factors influencing the V_{oc} of a μc-Si:H n-i-p solar cell.

	Possibilities	**Influences on V_{oc}**
1	Short-circuiting paths that are observed in the XTEM pictures of cells deposited on a rough Ag/ZnO substrate	Not for cells with R_{scD} > ~ 100 Ω cm^2.
2	Influence of the differences in effective areas on the dark saturation	No.

	current density	
3	Difference in the structure of p-type μc-Si:H and the p/i interface layers	No.
4	Difference in the electronic properties of the p-type μc-Si:H layer and the p/i interfaces	Not likely. The p-layer was optimized and the deposition was well controlled.
5	Difference in amorphous volume fraction in the i-layer	Possible, but not due to the p-side of the i-layers.
6	Difference in the electronic properties of the n-type μc-Si:H layer	Possible, n-layer may have different structure due to its possible discontinuity on a rough substrate.
7	In-diffused impurities, especially through the pinholes formed in the cells deposited on a rough substrate	Yes.
8	Difference in the electronic defect density of μc-Si:H i-layer	Yes.

We note that though the microvoids that are filled with conductive material is not the cause for the difference in cell V_{oc} as we have showed in section 3.4.2.2, unintentional doping caused by impurities such as moisture and oxygen diffused into those voids may very well influence the transport properties of the intrinsic μc-Si:H layer. This is the question to be answered by further experiments. In the following section I will focus our discussion on how the defects in the intrinsic μc-Si:H layer are formed due to the roughness of the substrates used.

3.5 Silicon crystal growth on a Ag/ZnO coated substrate

From the XTEM pictures shown in Fig.3.10 and the pictures published by other groups (for instance by Meier et al. [5] and Nasuno et al. [6]), it is clear in the first stage of deposition that the silicon crystallites tend to grow almost perpendicular to the substrate local surface. The continuous increase in film thickness is accomplished by the formation of crystallites elongated in the same direction as those that already exist within the film. As a result of this epitaxial-like film growth, columns are formed with their z-axes roughly perpendicular to the original local surface of the substrate.

3.5.1 Silicon growth on a flat surface

If the substrate surface is perfectly flat, the columns will continue developing in their original direction, with a tendency to increase in diameter as long as the micro-

environment around the film growing front allows for that. At least two factors will limit the expansion of the silicon crystal columns in the lateral direction. First, the silicon containing precursors, mostly believed to be SiH_3, must have enough mobility on the growing surface in order to find a suitable place to be connected to the silicon lattice. This is a general requirement for the formation of silicon crystallites in the growth of silicon thin films. Second, there must be enough space for the widening of these columns, i.e., the density of the columns must not be too high. Based on our study on μc-Si:H deposited by hot-wire CVD on a flat substrate (Corning 1737 glass) with $R_H \sim 0.95$ and at a substrate temperature around 250 ºC, if the deposition parameters are held constant, this second factor is almost solely determined by the density of nucleation sites formed already in the initial stage of film growth. For example, in most μc-Si:H materials deposited on an a-Si:H surface, large cones are formed near the substrate. This is due to the low nucleation density formed on (or in) the a-Si:H under those deposition conditions. With the increase of layer thickness, these silicon cones develop along the layer growth direction and can finally become columns by colliding with each other at a distance far from the substrate (~0.5 μm or more), as is shown in Fig.3.15. The films containing both columns and cones are figuratively named as having a "pencil-box" structure [7]. Using a highly crystalline thin μc-Si:H layer, or a "seed layer", normally deposited with a high hydrogen dilution ratio [8] , the density of nucleation sites can be greatly modified, and therefore the diameter of the silicon columns (the "pencils"), can be largely decreased. Based on this understanding, Bailat et al [7] proposed a nuclei density model to generally describe the R_H [defined as $H_2/(H_2+SiH_4)$ gas flow ratio] dependence of cell V_{oc}, in which the importance of the changes in the average amorphous volume fraction in this heterophase region (where the cones appear) is stressed. We comment here, however, that this nuclei density model is not sufficient to describe the general dependence of V_{oc} of μc-Si:H cells on R_H, since in their model the crystallinity difference in the bulk of the i-layer was not taken into account, as Bailat et al described themselves. One can easily see that this is indeed the case in the *rms* roughness series presented here. The two samples in Group A have a higher amorphous volume fraction in their n-layer than the samples in the other groups (Group B, C, D and E), which will likely result in some elongation of the incubation phase (the heterophase) of the intrinsic μc-Si:H layer near the n/i interface. According to the nuclei density model, this would be the reason for the higher V_{oc} observed on these two samples. However, we also observe a lower Raman crystallinity (X_c) of these two samples (Fig. 10a and Fig. 10b) which is similar to that of the i-layers deposited with a lower R_H ratio. Since the excitation laser impinges from the p-side of the n-i-p stacks and the laser light can not penetrate even half of the i-layer thickness, contributions from the silicon atoms in and near the n-layers can not be observed in the Raman patterns. The higher V_{oc} of these two samples can then be better explained by the higher amorphous volume fraction in their i-layers, using the effective Eg $\sim X_c$ model.

3.5.2 Silicon growth on a rough Ag/ZnO surface

For μc-Si:H developed on top of a rough Ag/ZnO substrate, some additional factors are involved. Firstly, the properties of the substrate material, such as the chemical reactivity and lattice structure, will influence the initial growth of silicon. Since we are discussing Ag/ZnO substrates with the ZnO layers grown all under identical conditions, influences from this aspect will be limited. But we have to keep in mind that due to the conductive nature of this type of substrate, there will be differences in the local electromagnetic field near the substrate surface compared to the situation when a flat and insulating glass substrate is used. This influence from substrate has to be considered for the PECVD deposited layers, namely the n- and p-type μc-Si:H layers deposited before and after the μc-Si:H i-layer. For the HWCVD deposited i-layer, the influence from the electro-magnetic properties of substrate is considered to be negligible, due to the lack of strong electron-magnetic field during deposition.

Since, as we have shown previously, that the n-layer also acts as a seed layer for the growth of μc-Si:H i-layer in the n-i-p stack, the possible variation of the n-layer structure brought about by the roughness of the substrate surface has to be considered. In a high frequency (RF or VHF) plasma environment, a stronger electromagnetic field is present at the higher points (the tips) than other places on the substrate surface. The result of this is a larger chance of forming silicon nucleation sites on a tip than in a valley of the substrate surface. Within the resolution limit of the TEM pictures we obtained for this set of samples, we cannot always observe directly the difference in the density of small crystallites in such a thin n-layer. However, since we are concerned mostly with the influence of this possible structure inhomogeneity of the n-layer on the growth of intrinsic μc-Si:H, it is of the same interest to study the density of nucleation sites inside the i-layer where the silicon crystal columns start developing (where the tips of the "pencils" are located). The TEM pictures containing both rough and flat regions were studied for this purpose. One of the pictures is shown in Fig.3.17, from which one can indeed see that fewer crystallites on the flat region at the substrate/ silicon interface (dashed white arrow) than on a rougher region (solid white arrows). The μc-Si:H crystalline columns that develop on top of the flatter surface also show a larger width than those developing on top of the rougher regions. Although this rather clear difference was not always observable in all the TEM pictures, it seems there is a trend that silicon cones are more densely distributed near the high point of the substrate. This observation indicates that at least under these deposition conditions, the structure inhomogeneity of the PECVD deposited n-layer can have an influence on the development of the μc-Si:H i-

layer, even though there is no strong electromagnetic field at all during the growth of a hot-wire deposited i-layer.

How the V_{oc} is influenced by this rather local difference is another issue. The difference in the cone densities may result in a higher amorphous volume fraction near a valley or a flatter area than near a rougher area. But this difference will be averaged out on a larger scale. Moreover, this micro-size difference in crystallinity exists only near the n-side of the i-layer; in the bulk of the i-layers, we cannot find any crystallinity difference between these samples from their XTEM pictures. As we pointed out earlier, also no difference is observed in the Raman spectra of the samples deposited under identical conditions on substrates with different surface roughness (samples in group B, C, D and E). Therefore, the crystallinity in the p-side of the i-layer is in general the same. If there is any influence in this respect, it can only originate from the n-side of the structure. We note, for this set of samples, that it is often observed that even in a valley of a substrate surface still nucleation sites are formed. A sharp decrease in the nuclei density is only observed in valleys with very small opening areas, ~100 nm in diameter.

3.5.3 Two types of collisions of columnar silicon and the formation of the low density stripes

On a rough substrate, the development of the silicon columns growing perpendicular to the local substrate surface will be limited by the adjacent columns developing in different directions (perpendicular to the local substrate surface where those columns originate). In the region where these columns collide, silicon atoms are no longer periodically arranged; amorphous phases are formed accompanied with a large number of structural defects. In a bright field TEM picture, these defective regions (with lower atom densities) appear to be brighter than the surrounding area, if they are not covered (shaded) by the neighbouring silicon columns.

Two types of collisions need to be distinguished at this stage. One is the collision between columns growing in more or less the same direction, which is typically observed in the bulk of μc-Si:H materials deposited on a flat substrate; they do not show particular dependence on substrate surface morphology. The other is the collision between columns of clearly different directions, which are most frequently observed in materials deposited on a rough substrate. For convenience, we call the first phenomenon type 1 collisions, and the second phenomenon type 2 collisions. In the TEM picture of a material with only type 1 collisions, we normally do not observe white stripes as shown in Fig.3.10a-c; instead, the boundary of the collided columns appear to be very narrow, the width being generally more than an order of magnitude less than the thinnest part of TEM specimens

so that it is often hard to observe them. A TEM picture containing such collisions is shown in Fig.3.15.

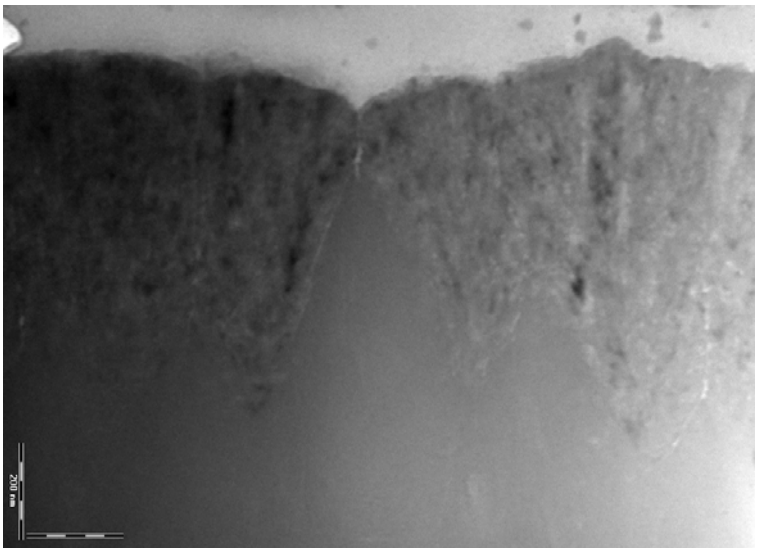

Fig.3.15 TEM picture of a μc-Si:H material sample deposited on top of amorphous a-Si:H layer on Corning 1737 glass. The scale bar shown in the picture is 200nm.

For type 2 collision, however, stripes appear frequently, and there is a clear correlation between the appearance of these white stripes and the opening angle of the substrate surface texture. If we define the opening angle (δ) as the adjacent ZnO facets measured on the Si/ZnO interface profile on the cross-sectional TEM pictures, we can quantify this dependence for this *rms* roughness series based on these pictures. Fig.3.16 summarizes the influence of δ on the diameter of these white stripes. The diameter values were taken at the widest part of the stripes, most frequently near the valley where the stripes start to be visible. It appears that the width of the stripes tends to be larger when δ becomes smaller; and a clear threshold exists at approximately 110 degrees; at the places where δ is larger than that value, no stripes could be observed (Fig.3.16).

The mechanism behind the existence of this threshold for stripes formation can be explained based on the covalent bonding structure of the silicon network. Silicon atoms have four electrons in their outermost shell. Due to the sp_3 hybridization of atomic orbitals, tetrahedral coordinated strong covalent bonds are formed with a bonding angle of 109.47º. In the network of crystal silicon, the bonding angle and length (2.30Å) are strictly followed; any tiny variations in these values create stress in the lattice. Increases in the stress due to changes in the bonding angle and length will eventually result in the

breakage of the covalent bond and form a structural defect in the silicon lattice. In the case of μc-Si:H or a-Si:H, the situation is quite similar, except for some difference in the degree of tolerance to the variation of the silicon bonds.

In amorphous silicon, the bond angle and length can vary to such an extent that the conventional defined silicon lattice cannot extend larger than a few atomic distances. Earlier simulations on the bonding environment in amorphous silicon showed that a variance of around 10º (~10%) in Si-Si-Si bond angle can exist [9, 10], which means that the minimum angle of Si-Si-Si bond can be around 100º. More recently, Kugler *et al.* conducted a thorough survey based on the Cambridge Structural Database (CSD) (a large experimental data base), and reported bond angles of as low as around 90^{o} can exist in amorphous silicon [11, 12]. Knoesen et al observed stripe-like defects in XTEM pictures of a-Si:H materials made on rough TCO substrates, and the minimum opening angle for the observation of those stripes was shown to be around 90^{o} [13], this correlates very well with Kugler's report [11, 12].

For μc-Si:H material, the allowed variance in Si-Si-Si bond angle is much smaller than for a-Si:H. It is reasonable to assume that the bond angles are not to be much different from 109.47^{o}. This explains the ~110^{o} threshold value we observed in this set of samples.

The dependence observed between the width of the stripes w_v and the local surface opening angle δ can be explained by the existence of the local stress in the silicon network near the micro-valleys, which is caused by the unfavourable δ values. Due to the atomic etching mechanism on the film growing surface, silicon atoms weakly bounded to the silicon atomic network with a bonding strength lower than a certain value are etched away, resulting in a space where no silicon is present in the network.

Imagine some silicon containing precursors moving toward the region where the two columns are about to touch. The only way that they can permanently fill in the gap between the two columns is to build bonds with the silicon atoms on each column. Due to the unfavourable angle formed between the front surfaces of the two columns (denoted as δc), it is not possible for the silicon atoms to immediately bond with the atoms already existing on the column surface. Instead, a stack of many atomic layers are needed, in which weak bonds with the Si-Si bonding angles only slightly different than 109.5^{o} (denoted as α_{si}) have to be formed, in order to "absorb" the large initial difference between α_{si} and δ_c. Upon accumulating silicon atomic layers containing slightly relaxed bond angles, a-Si network can be formed in the valleys of the substrate, with the condition that the stress created in the atomic network due to this bond distortion do not exceed a limit. Over that limit, the silicon network can not hold anymore, due to the strong etching effect by radicals such as atomic hydrogen near the film growing surface.

As a result, voids are formed in the middle of the valleys, in which no silicon atoms can stay. Upon the increase of layer thickness, the voids elongate in the direction roughly perpendicular to the substrate surface, as long as the Si-Si bonding requirement around them are not fulfilled.

From Fig.3.10, it can be seen that the front surface of the growing silicon film propagate in a direction perpendicular to the substrate surface, and with the surface profile similar to that of the substrate. Therefore, the opening angle δ between substrate local surfaces maintain essentially unchanged with the increase of film thickness, namely, $\delta c \approx \delta$. Thus, the δ_c in the above discussion can be substituted by the substrate surface micro-angle δ. The smaller the δ is, the more weak bonds will be needed to connect the surrounding Si atoms in the valleys, therefore the more silicon atoms will be etched away, which in the end results in even wider and longer gaps that not filed with silicon atoms. The diameter of these micro-voids depends on the density of etching elements, namely atomic hydrogen, the amount of weak Si-Si bonds, which is related to the angle δ, and the local substrate surface condition, such as substrate temperature and the degree of hydrogen coverage.

In Fig.3.16, the δ values for the two points surrounded by a dashed circle were taken from the local opening angles of a Ag surface instead of from those of the ZnO surface, since the stripe-like voids for these points start from the ZnO layer already. This could also be explained with the model described above, i.e. the minimum of bonding angle required for the formation of continuous ZnO network is not met. From Fig.3.16, the value of this minimum is between 20 and 40 degrees. Further study is needed to clarify the micro-mechanism of this phenomenon for ZnO.

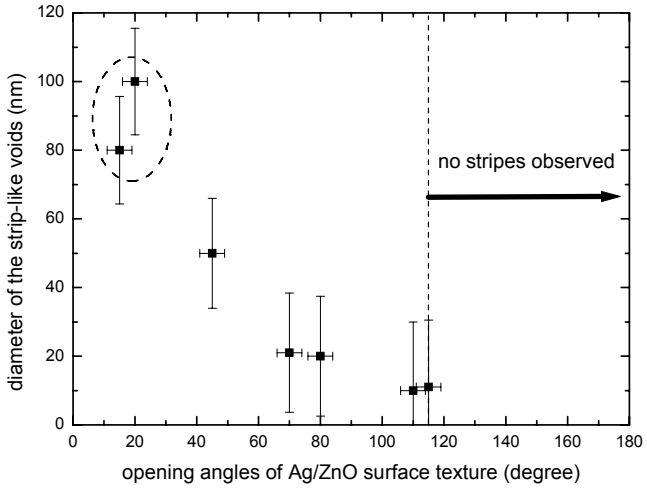

Fig.3.16 Correlation between the opening angle of the Ag/ZnO surface texture and the diameter of the micro voids (white stripes) determined from the TEM pictures of the sample series listed in Table 3-3.

Fig.3.17 XTEM picture of a µc-Si:H sample. Arrows and "T" letters indicate the origin and the width of columnar silicon, respectively. The dashed arrow indicates the place where silicon grows with a lower nucleation density.

3.6 More general discussion: a complete diagram for μc-Si:H n-i-p cell developed on rough Ag/ZnO substrate

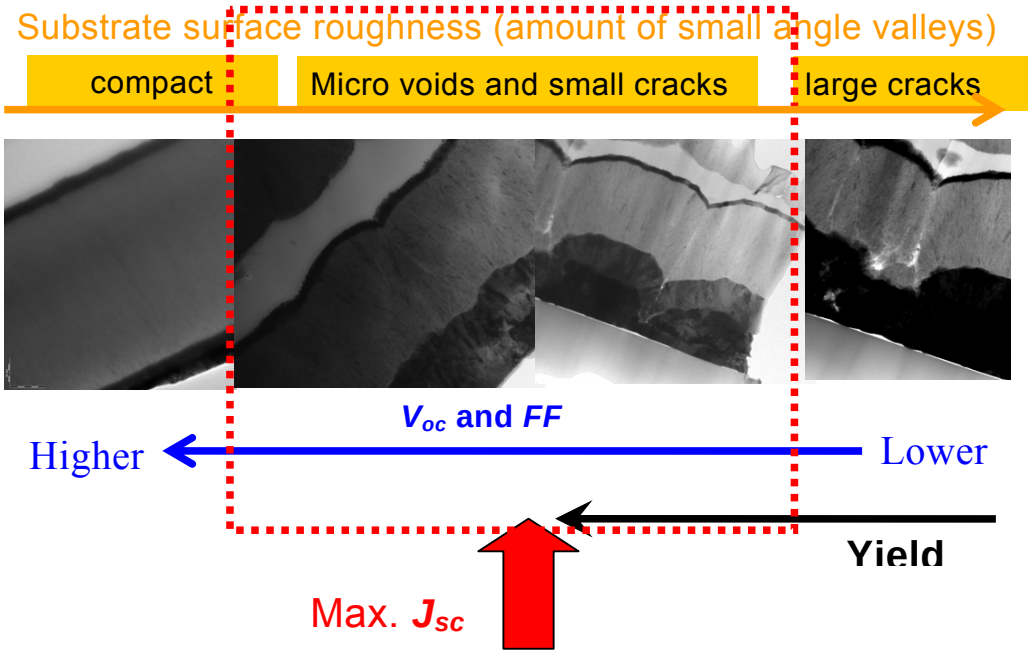

Fig.3.18 TEM pictures of μc-Si:H n-i-p solar cells deposited on (from left to right) flat, medium rough and very rough glass/Ag/ZnO substrate. The total thickness of the silicon layers for all the samples shown in this picture is around 1.3 μm.

Based on the discussion in section 3.3, 3.4 and 3.5, a diagram of a set of TEM pictures of μc-Si:H n-i-p solar cells deposited on (from left to right) flat, medium rough and very rough glass/Ag/ZnO substrates is shown in Fig.3.18. The total thickness for the silicon layers for all the samples shown in this picture is around 1.3 μm. Since the highest AM1.5 current density is obtained on cells made on a medium rough substrate [15], the best single junction μc-Si:H solar cell efficiency made in house is also obtained in that region (8.5% without encapsulation, see Chapter 4, a cell with a reverse hydrogen profiling). Further improvement in cell efficiency would not only require an enhancement of the optical trapping, but also a modification of the substrate surface morphology, in order to suppress the detrimental effect of rough substrate surface on the quality of silicon layers.

As a guide for the substrate development, we suggest that the local surface of the substrate should have an opening angle not much smaller than 110º, or the distances

between the adjacent micro-cliffs are wide enough so that the collision plane of the tilted silicon columns is far from interfaces or even beyond the thickness of i-layer. Meeting these criteria while maintaining the maximum light-scattering ability, an "ideal" substrate for thin film μc-Si:H solar cells can be found.

3.7 Conclusions

By studying the μc-Si:H n-i-p solar cell samples made on Ag/ZnO substrates with different *rms* roughness, we have gained the following knowledge.

1. Substrate roughness has a large influence on the growth mechanism of μc-Si:H.
2. In the case of rough Ag substrates with Ag layers deposited at a very high substrate temperature, >350 ºC in our experiments, and with a relatively large Ag layer thickness, the subsequent deposition of ZnO and Si layers fails to conformally cover the submicron-cavities formed by the large Ag crystal grains. As a result, pinholes with diameters larger than ~100 nm appear in the silicon layers, which are responsible for the low yield for samples deposited on this type of substrate.
3. For μc-Si:H cells developed on a Ag/ZnO substrate with a medium rough Ag layer, the yield of working cells is high, but the obtained V_{oc}'s are lower than cells grown on smoother substrates. Two most probable reasons are identified: (i). micro-voids formed in the silicon layers near the Si/ZnO interface are propagating into the Si i-layer, due to which impurities such as oxygen may be accumulated, which dopes the material; (ii). a higher electronic defect density is caused by the higher grain boundary density in the μc-Si:H layers when grown on a rough substrate due to collision of silicon columns. In both cases the morphology of the substrate surface plays an important role, and it is therefore essential to control it in order to further improve the efficiency of microcrystalline silicon thin film solar cells.
4. Low density voids with diameters of about a few to a hundred nm are identified in silicon layers near the Si/ZnO interface, and in ZnO layer near the ZnO/Ag interface, where the layers start growth. The voids generally develop along the deposition direction and extend into the bulk of the intrinsic layer or through the silicon layers up to the top surface of the n-i-p structure, with a trend to decrease in width. These voids are suggested to be the path where impurities move in and dope the materials. The widths of the voids are found to be dependent on the local opening angle of the substrate surface. For the

voids starting in the silicon layer, the lowest opening angle of the local ZnO surface for the formation of these voids are found to be approximately 110 degree, which is correlated to the tetrahedral coordinated silicon covalent bond angle.

5. As a guide for the further development, a complete diagram for the structure of μc-Si:H n-i-p cell developed on rough Ag/ZnO substrate with different roughness has been composed. Suggestions on the further optimization of substrates surface morphology are given.

References

1. R. H. Franken, *Transparent conducting oxide contacts and textured metal back reflectors for thin film silicon solar cells,* PhD thesis, Utrecht University, the Netherlands, 2006.
2. R.H. Franken, R.L. Stolk, H. Li, C.H.M. van der Werf, J.K. Rath, R.E.I. Schropp, J. Appl. Phys. 102, 014503 (2007).
3. M. K. van Veen and R. E. I. Schropp, Appl. Phys. Lett. 82 (2003) 287.
4. R.L. Stolk, H. Li, J.J.H. Strengers, C.H.M. van der Werf, J.K. Rath, R.E.I. Schropp, 20th European Photovoltaic Solar Energy Conf., Barcelona, Spain 6-10 June, 2005, pp1655.
5. J. Meier, S. Dubail, S. Golay, U. Kroll, S. Faÿ, E. Vallat-Sauvain, L. Feitknecht, J. Dubail, A. Shah, 12th IEEE PVSC proceedings, 2001, 26.1.
6. Yoshiyuki Nasuno, Michio Kondo and Akihisa Matsuda, Jpn. J. Appl. Phys. 40 (2001) L303.
7. J. Bailat, E. Vallat-Sauvain, L. Feitknecht, C. Droz, and A. Shah, J. Appl. Phys. 93 (2003) 5727.
8. J.K. Rath, F.D. Tichelaar, H. Meiling and R.E.I. Schropp, Mat. Res. Soc. Symp. Proc. 507 (1998) 879.
9. D.E. Polk, J. Non-Cryst. Solids 5 (1971) 365.
10. J.S. Lannin, Phys. Today 41 (1988) 28.
11. S. Kugler, L. Pusztai, L. Rosta, P. Chieux, R. Bellissent, Phys. Rev. B. 48 (1993) 7685.
12. S. Kugler and Z.Vârallyay, Phil. Mag. Lett. 81 (2001) 569.
13. D. Knoesen, R.E.I. Schropp, W.F. van der Weg, Mat. Res. Soc. Symp. Proc. 377 (1995) 597.

14. J.K. Rath, F.D. Tichelaar, and R.E.I. Schropp, Solid State Phenomena, special issue on "Polycrystalline Semiconductors V - Bulk Materials, Thin Films and Devices", 67-68 (1999) 465.
15. H. Li, R.H. Franken, R.L. Stolk. C.H.M. Van der Werf, J.K. Rath, R.E.I. Schropp, Mat. Res. Soc. Symp. Proc. 989 (2007) A18.3.

4

Improvement of µc-Si:H n-i-p cell efficiency with an i-layer made by hot wire CVD by reverse H2-profiling[1]

The technique of maintaining a proper crystalline ratio in microcrystalline silicon (µc-Si:H) layers along the thickness direction by decreasing the H_2 dilution ratio during deposition (H_2 profiling) was introduced by several laboratories while optimizing either n-i-p [2] or p-i-n [3] µc-Si:H cells made by PECVD. With this technique a great increase in the energy conversion efficiency was obtained. Compared to the PECVD technique, the unique characteristics of HWCVD, such as the catalytic reactions, the absence of ion bombardment, the substrate heating by the filaments and filament aging effects, necessitate a different strategy for device optimization. We report in this chapter the result of our method of using a *reverse* H_2 profiling technique, i.e. *increasing* the H_2 dilution ratio instead of decreasing it, to improve the performance of µc-Si:H n-i-p cells with an i-layer made with HWCVD. The principle behind this technique is thought to be a compensation effect for the influence of progressing silicidation of the filaments during the growth of µc-Si:H, especially when the filament current is held constant during

deposition. The dependence of the material crystallinity on thickness with and without H_2 profiling is discussed and solar cell *J-V* parameters are presented. Thus far, the best efficiency of μc-Si:H n-i-p cells made on a stainless steel substrate with a Ag/ZnO textured back reflector made in house has been improved to 8.5%, which is the highest known efficiency obtained for n-i-p cells with a hot-wire μc-Si:H i-layer.

4.1 Introduction

The application of solar cells with intrinsic hydrogenated microcrystalline silicon (μc-Si:H) as the absorber layer (i-layer) has shown promise for further extending the spectral range of thin film silicon based solar cells. Compared to the conventional plasma enhanced chemical vapour deposition (PECVD) technology [4], hot-wire CVD (HWCVD) can produce device quality μc-Si:H at a high rate without dust formation in the gas phase, therefore reducing the need of an extensive chamber cleaning process. At Utrecht University, we develop solar cells with an intrinsic μc-Si:H i-layer made by HWCVD on stainless steel substrates with a n-i-p structure, aiming to use them as the bottom cell of a triple junction solar cell [5]. Previous cells deposited on plain stainless steel at a high substrate temperature (> 400 °C) yielded a V_{oc} of only 0.41 V and a J_{sc} of 16.1 mA/cm^2 because of the very high crystallinity and the absence of a back reflector [6]. To quickly utilize our newly developed Ag/ZnO rough back reflector [7], the decision was made to first optimize the bottom cell with a μc-Si:H i-layer deposited at a reduced substrate temperature. In doing this, a careful review of the silicon growth mechanism was performed. Special techniques for the material optimization, such as the use of seed layers and defect density control by hydrogen profiling [2, 3], were employed. This chapter presents the result of μc-Si:H n-i-p cells with an i-layer deposited by HWCVD by employing a *reverse* H_2 profiling technique.

4.2 Experimental details

All silicon layers were deposited in the multi-chamber UHV PASTA system [8]. The intrinsic layers were deposited by means of HWCVD, whereas for the doped layers in the cell PECVD at 13.56 MHz was used. The cell structure was: SS/rough Ag/ZnO /n-type μc-Si:H /intrinsic μc-Si:H/buffer/p-type μc-Si:H/ITO/Au (gridlines), with an active cell area of 0.13 cm^2. HWCVD was performed using two straight tantalum wires (0.5 mm in diameter) that were about 4 cm from the substrate, through which a constant current of 10.5 A was passed, yielding a wire temperature around 1850 ºC in vacuum without source gas as measured with a pyrometer. No extra substrate heating was used, which

results in a substrate temperature of around 270 °C when the system is in an equilibrium condition. Raman spectroscopy at a laser wavelength of 514.5 nm was employed to measure the crystalline ratio of absorber layers and complete solar cells. The sample thickness for each silicon deposition was measured on accompanying glass substrates using a surface step profiler (Dektak). Average deposition rate for intrinsic µc-Si:H layers was calculated accordingly and was typically around 2 Å/s. The current density – voltage (*J-V*) characteristics of the solar cells were measured at 25 °C under AM1.5 100 mW/cm^2 white light generated by a dual beam solar simulator (WACOM). A 0.3 mm thick SS mask used for depositing the ITO top contact was also used during the measurement to have a precise definition of the cell area.

4.3 Results

4.3.1 Structural variation of µc-Si:H materials grown at a phase transition regime

Various µc-Si:H material samples have been made. Part of the data has been published earlier [9], from which a substrate dependence of the sample crystallinity could clearly be seen. Based on these results, a series of material samples with different i-layer thickness and with a range of constant hydrogen dilution ratios (R_H = 0.935, 0.943, 0.948, and 0.952, where R_H is defined as the hydrogen fraction of the total gas flow, $H_2/(H_2+SiH_4)$) were deposited on Asahi U-type TCO glass coated with a thin Ag/ZnO back reflector and a thin n-layer, in order to simulate the situation of the surface when the i-layer is grown in a cell. Except for the difference in R_H, all other deposition conditions were kept the same. Raman spectroscopy showed that, except for samples deposited at R_H = 0.935, all samples were µc-Si:H (Fig. 1). The crystalline ratio X_c, defined as the integrated area ratio between the crystalline Si TO peak and the a-Si:H TO peak $(I_{520}+I_{510})/ (I_{520}+ I_{510}+ I_{480})$, showed no sign of an increase with thickness for all the µc-Si:H samples between thicknesses of 500 and 1500 nm. Some layers even showed a *decrease* in X_c. This was against our expectation, since it is widely observed that the crystallinity of µc-Si:H material increases with thickness [10].

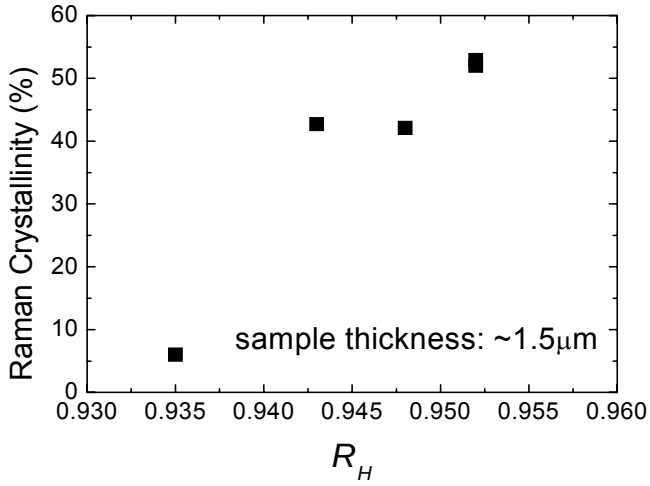

Fig. 4.1: Raman crystallinity of samples deposited on substrates with a textured back reflector (Asahi/Ag/ZnO/μc-Si:H n-layer) at different constant hydrogen dilution ratios R_H.

Moreover, we found, as shown in Table 1, for a 1.5 μm thick sample grown with two hydrogen dilution steps (sample set C), the first 1 μm at R_H = 0.952 and the next 0.5 μm at R_H = 0.943, that X_c showed much lower values than the samples grown with a constant R_H = 0.943 (sample set B). These observations indicate that some other parameters influence the i-layer growth. Since the filaments used for growing sample C had been used longer before starting the deposition, we believe an aged filament state is responsible for the observed lower X_c for this sample. A good measure of the filament condition is the filament resistance. As reported earlier by Van Veen *et al.* [9] and by D. Grunsky *et al.* [11], the resistance of the filament increases after each deposition, for every filament used. This is attributed mainly to silicidation of the filament during the catalytic reaction. Its catalytic ability therefore decreases with time.

Table 4-1 Raman crystallinity of μc-Si:H i-layers made on top of Asahi/ Ag/ZnO/n-type a-Si:H with different $\boldsymbol{R_H}$.

sample set	R_H	*Total thickness (nm)*	X_c *(%)*
A	0.952	500~1500	55 ± 5
B	0.943	1420±50	43 ± 5
C	first 1 μm at 0.952 and then 0.5 μm at 0.943	1420±50	29 ± 5

4.3.2 Control of µc-Si:H i-layer quality by *reverse* H_2 profiling.

The observations of the crystallinity of µc-Si:H decreases with thickness led us to design experiments in which the hydrogen dilution ratio during i-layer deposition is *increased* instead of decreased, so it is changed in the *reverse* direction of that normally used by other groups when developing µc-Si:H cells using the PECVD technique [2]. Fig. 2 shows the AM1.5 *J-V* characteristics of several µc-Si:H n-i-p cells; the cell output parameters are listed in Table 2. "Cold start" means that the i-layer deposition was started shortly after switching on the filament current (before the point where the chamber reaches a thermal equilibrium condition). Clearly, all cell parameters have improved dramatically by applying this '*reverse* profiling'. The cell efficiency has reached 8.5 %, which is the highest value reported so far for a µc-Si:H n-i-p cell with a HWCVD i-layer, and one that is in line with the best results reported for similar cells with VHF plasma-enhanced CVD i-layers [12].

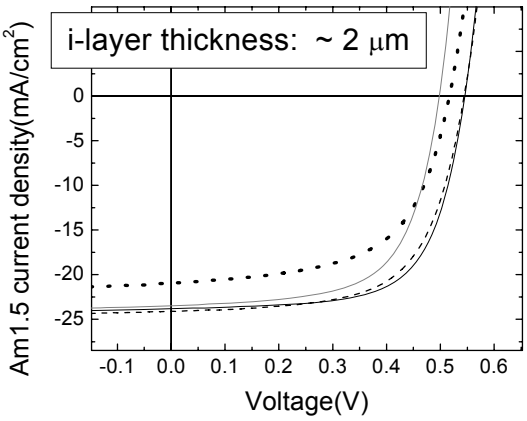

Fig. 4.2: AM1.5 *J-V* characteristics of µc-Si:H n-i-p cells on SS with a Ag/ZnO TBR. (1) Grey line: constant H_2 dilution at R_H = 0.953; (2) dotted line: constant H_2 dilution at R_H = 0.948; (3) dashed line: two step profiling, 1st half at R_H = 0.948, 2nd half at R_H = 0.952; (4) solid black line: with the same H_2 profile as (3), but with a cold start. The i-layer deposition rate is around 2 Å/s.

Table 4-2. AM1.5 output parameters of the µc-Si:H n-i-p cells shown in Fig. 2.

Sample No.	*remarks*	*Efficiency [%]*	J_{sc} *[mA/cm²]*	V_{oc} *[V]*	FF
1	Without H_2 profiling (R_H = 0.953)	7.5	23.5	0.498	0.641
2	Without H_2 profiling (R_H = 0.948)	6.5	21.2	0.517	0.594
3	With two step H_2 profiling (R_{H1} = 0.948, R_{H2} = 0.952)	8.4	24.2	0.544	0.636
4	Two step H_2 profiling + cold start	8.5	23.4	0.545	0.668

4.4 Discussion

The decrease in X_c with increasing layer thickness for μc-Si:H materials deposited close to the phase transition from the amorphous to the microcrystalline regime was already observed in an earlier study by Van Veen *et al.* [13]. The difference between the present and the previous work is that we now used a slightly higher H_2 dilution ratio, i.e. the deposition starts at R_H = 0.948 instead of 0.935 [13]. Our results are in disagreement with the widely accepted phase diagram concept of Collins *et al.* based on studies on samples prepared by PECVD [10], clearly indicating the uniqueness of the HWCVD technique in depositing μc-Si:H material. Clear explanations for this phenomenon are not yet available, though filament aging is likely to play a key role. Further understanding requires a detailed knowledge of the reactions at the filament surface, as well as in the gas phase and on the growing sample surface.

Our results show that n-i-p cells with an i-layer made with R_H = 0.952 and a thickness of about ~2 μm do not suffer from a structural evolution [sample set A in Table 1] and, therefore, show a higher J_{sc} and a good *FF* (sample #1 in Fig. 2 and Table 2). The lower V_{oc}, < 0.5 V, is obviously related to the rather high X_c in the i-layer. A slight decrease in R_H (sample #2, R_H = 0.948) promotes V_{oc} a bit, but at the cost of the *FF* due to the already started structural evolution in the i-layer. More seriously, carrier collection in the i-layer is negatively affected, which, together with the lower (infra-) red absorption due to the lower X_c, results in a more than 2 mA/cm^2 decrease in J_{sc}. By using a two-step H_2 profiling (sample #3), the i-layer quality is maintained, and all cell parameters increase: the *FF* is back to ~0.64, the V_{oc} jumps to 0.544 V, and the J_{sc} increases to more than 24 mA/cm^2. The increase in V_{oc} can be attributed to the slight decrease in crystallinity compared to the cell with higher R_H; and the increase in J_{sc} is because of the better collection for the photogenerated carriers. By using a cold start the cell efficiency further increases, mainly because of the increase in *FF* (sample #4).

The use of the "cold start" is based on the idea that properly lowering the substrate temperature will increase the H residence time at the growing film surface, therefore resulting in a low defect density in the i-layer. The positive feedback from the experimental results hints that the defect density in the i-layer might be further reduced if we use a reduced substrate temperature (T_{sub}) during the entire layer deposition. The T_{sub} used for this study, ~270ºC in the equilibrium state, is quite high compared to that used by other groups [14]. This is mainly due to the relatively small filament-to-substrate distance of ~4 cm. As an advantage, the i-layer deposition rate is nearly 2 times higher than that obtained by the Jülich group for their reported best μc-Si:H cell with a HWCVD i-layer [14]. An increase in the filament-to-substrate distance will reduce the substrate temperature, but will also decrease the deposition rate. Other techniques, such as

substrate cooling or use of moving substrates, are more favourable. The latter has a great advantage for mass production, especially in roll-to-roll technology. Here we note that the absence of strong electromagnetic fields in the hot-wire CVD technique makes the design of a vacuum chamber with a moving substrate much easier compared to that of a conventional PECVD chamber.

4.5 Conclusion

In this chapter, we presented our results on using a *reverse* H_2 profiling technique to improve the i-layer quality in single junction μc-Si:H thin film solar cells with an i-layer made by Hot-Wire CVD. This design is based on our study of the structural evolution of HWCVD deposited μc-Si:H in the phase transition region between a-Si:H and μc-Si:H. Cells with an i-layer grown with this technique showed a record efficiency of 8.5 % for single junction n-i-p cells with a HWCVD μc-Si:H i-layer. This new method allows the development of μc-Si:H cells with higher efficiency at higher deposition rate.

References

1. Presented at 4th international Conference on Hot-Wire CVD (Cat-CVD) process, Oct.4-8, 2006, Takayama, Gifu, Japan, Thin Solid Films 2007, in press.
2. B. Yan, G. Yue, J. Yang, and S Guha, D. L. Williamson, D. Han, C. Jiang, App. Phys. Lett. 85 (2004) 1955.
3. A. Gordijn, J.K. Rath, and R.E.I. Schropp, Prog. in Photovoltaics.: Res. Appl. 14 (2006) 305.
4. A.A. Howling, C. Hollenstein, and P.J. Paris, Appl. Phys. Lett. 59 (1991) 1409.
5. R.L. Stolk, H. Li, R.H. Franken, J.J.H. Strengers, C.H.M. van der Werf, J.K. Rath and R.E.I. Schropp, J. Non-Cryst. Solids 352 (2006) 1933.
6. H. Li, R.L. Stolk, C.H.M. van der Werf, R.H. Franken, J.K. Rath and R.E.I. Schropp, J. Non-Cryst. Solids 352 (2006) 1941.
7. R.H. Franken, C.H.M. van der Werf, J.K. Rath, R.E.I. Schropp, 21st European Photovoltaic Solar Energy Conference and Exhibition, Dresden, Germany, September 4-9, 2006, 3AO.8.4.
8. R.E.I. Schropp, K.F. Feenstra, E.C. Molenbroek, H. Meiling and J.K. Rath, Philos. Mag. B 76 (1997) 309.
9. M. van Veen, *Tandem solar cells deposited using hot-wire chemical vapor deposition,* Ph.D thesis, Utrecht University, The Netherlands, 2003.

10. R.W. Collins and A. S. Ferlauto, Curr. Opin. Solid. St. M. 6 (2002) 425, and R.W. Collins, A.S. Ferlauto, G.M. Ferreira, Chi Chen, Joohyun Koh, R.J. Koval, Yeeheng Lee, J.M. Pearce, C.R. Wronski, Sol. Energ. Mat. Sol. Cell. 78 (2003) 143.
11. D. Grunsky, M. Kupich, B. Hofferberth, B. Schroeder, Thin Solid Films 501 (2006) 332.
12. B. Yan, G. Yue, J.M. Owens, J. Yang, and S. Guha, 4th World Conference on Photovoltaic Energy Conversion, Waicoloa, Hawaii, May 7-12, 2006.
13. M.K. van Veen, C.H.M. van der Werf and R.E.I. Schropp, J. Non-Crys. Solid. 338-340 (2004) 655.
14. S. Klein, F. Finger, R. Carius and M. Stutzmann, J. Appl. Phys. 98, 024905 (2005).

5

Current limiting barriers at the i/p/TCO region of n-i-p single junction solar cells

The importance of a good quality i/p/TCO region in thin film silicon solar cells (n-i-p or p-i-n) has long been discussed. However, practical difficulties of forming a well performed TCO/p/i region have never been solved. Barriers are often found in this region, which form puzzles for device optimization. In this chapter, we discuss the two barriers that were found in the ITO/p/i interfaces in single junction SiGe:H n-i-p cells, and study the influence of such barriers in the solar cell *J-V* properties.

The content of this chapter is arranged as the following: in the first part of section 5.1, we give a short description on the classical theory for the carrier transport through a TCO/p junction; then we give a review on the deposition techniques that used to deposit a thin boron doped μc-Si:H layers needed for thin film silicon solar cells, and show the practical difficulty of forming such a thin layer on top of a device quality amorphous silicon (alloys) layer. In section 5.2, extensive annealing experiments on proto-SiGe:H n-i-p cells are presented, and carrier transport barriers represented by typical S-shaped *J-V* characteristics are discussed. In Section 5.3, dark *J-V* characteristics taken before and after annealing are analyzed, in an attempt to compare light *J-V* characteristics with and

without the typical S-shape. In this last part, a discussion on carrier transport in p-i-n (n-i-p) cells is needed to gain insight in the underlying mechanisms that cause the S-shaped *J-V* characteristics.

5.1 Interfaces between boron doped microcrystalline silicon and its adjacent layers

5.1.1 Contact barriers at TCO/p interface of a n-i-p solar cell – classical theory

Most TCO materials in use today for thin film silicon solar cells are n-type degenerated semiconductors. Their electron Fermi level is so close to or even above the conduction band that we may simply consider their Fermi energy as being on the same level as the conduction band edge. Therefore, the TCO/p interface may be studied based on a metal/ semiconductor contact model [1]. Fig. 5.1. illustrates the equilibrium band diagram of an idealized TCO/p interface without considering the possibly existing interface, such as oxide, layer between these two sides. The p-type silicon layer (shown on the right side of the figure) is assumed thick enough so that the activation energy in the bulk can be considered as constant. At thermal equilibrium, the Fermi level is horizontally distributed through the interface. Due to the work function difference between these two materials, a band mismatch exists on both the conduction edge and valance band edge. A depletion region, with a characteristic length L_0, appears at the p side. Referring to Fig. 5.1. the barrier height can be written as

$$\phi_{bi} = q\chi_p + (Eg_p - Ea_p) - q\chi_{TCO} \tag{5.1}$$

where, χ_p, Eg_p and Ea_p are the electron affinity, band gap, and bulk activation energy of the p-type silicon, respectively; χ_{TCO} is the electron affinity of TCO. Because of the one-side abrupt junction assumption, the width of the depletion region can be estimated by

$$L_0 = \sqrt{\frac{2\varepsilon_p(\phi_{bi} - 2kT)}{q^2 N_p}}, \tag{5.2}$$

where ε_p and N_p are the permittivity and doping concentration of the p layer, respectively [1]. Assuming a barrier height of 1 eV and a typical p-layer doping concentration around 10^{18}cm^{-3}, L_0 is of the order of tens of nanometres at room temperature. Notice that this is about equal to the p-layer thickness in a typical thin film silicon solar cell.

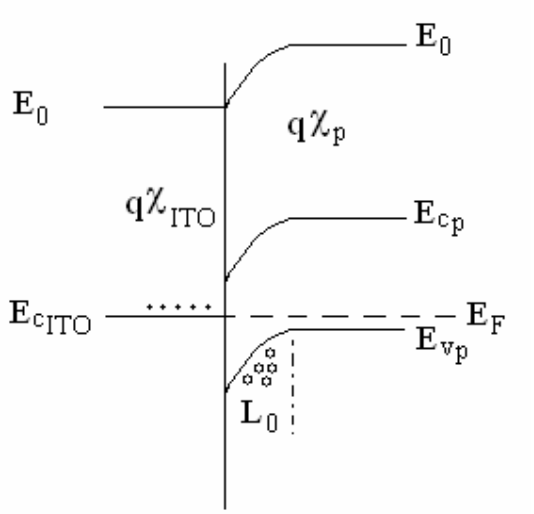

Fig. 5.1. Schematic diagram of a TCO/p interface in the equilibrium condition. E_0, E_c, E_v, and E_F are the vacuum level, conduction band edge, valence band edge and the electron Fermi lever, respectively.

Commonly used p-type silicon layers includes boron doped (p-type) a-SiC:H and μc-Si:H, both have a wide optical band gap which is necessary for a thin film silicon (n-i-p or p-i-n) solar cell to maintain a low optical absorption by this layer. Compared to the former, boron doped μc-Si:H has a lower electrical bandgap and much higher conductivity due to the high doping efficiency of dopants in such materials. As a result, the barrier formed between TCO and p-type μc-Si:H can be smaller and the width of depletion region in the p-μc-Si:H is much narrower, which is advantageous to hole transport. The electrical properties of boron doped a-SiC:H and μc-Si:H and their estimated contact barriers with ITO are listed in Table 5-1. Data for boron doped a-Si:H are also included, which will be discussed in the next subsection. In this table, the electron affinity of ITO was taken as 4.4 eV, and the data of silicon alloys are taken as the values commonly used for device simulations [2].

The data shown in Table 5-1 have been well chosen to fit both the theoretical estimation and the experimental data. In reality, however, the problem can be much more complicated due to the uncertainties from non-ideal interfaces and reduced layer qualities. In the following sections we discuss how, in practice, a shifted p-layer deposition condition influences the transport properties of photocarriers and the solar cell output performances. We start our discussion by an overview of p-type μc-Si:H deposition techniques and the structure dependence of p-layer properties.

Table 5-1. Properties of p-type Si materials and their estimated contact barrier height with ITO. Data are taken from [2] with a few modifications. The electron affinity of ITO is assumed to be 4.4 eV.

Contact materials	*p-a-SiC:H*	*p-μc-Si:H*	*p-a-Si:H*	*p-a-Si:H (low doping level)*
χ (eV)	3.7	4.1	3.8	3.8
Eg_p (eV)	2.0	1.1	1.8	1.8
Ea (eV)	0.5	~0.05	~0.4	~0.6
σ_d $(\Omega cm)^{-1}$	10^{-4}~10^{-5}	~1	10^{-4}~10^{-5}	10^{-8}~10^{-9}
ϕ_{bi} (eV) (with p-a-SiC:H)	0.8	0.8	0.8	0.6
N_p (cm^{-3})	3×10^{18}	9×10^{18}	3×10^{18}	1×10^{17}
L_0 (nm)	18	10	18	85

5.1.2 Structure of boron doped μc-Si:H

As we discussed in the previous chapters, the properties of μc-Si:H material made with plasma CVD and using the hydrogen dilution technique strongly depend on the substrate; its structure can also vary along the growth direction. When deposited on a foreign substrate, Si nucleation normally does not happen immediately; there is a short so-called incubation time in which silicon first grows with an amorphous structure. After this period, nucleation sites are formed at certain thickness, from which silicon columns or cones start growing. When the silicon columns or cones coalesce, a structure is formed such that basically no large structural changes are observe along the growing direction (though crystallinity may still increase to a certain extent with increasing thickness), as long as the deposition parameters remain constant. At about the thickness where nucleation starts, the material mass density becomes lower; the layer grows more porous. This can be seen from the bright field XTEM picture shown in Fig.5.2a in the region where the transparency is high, meaning that the density of silicon atoms is low. The three regions of a typical μc-Si:H material, i.e., incubation region, porous region, and the dense μc-Si:H region are schematically shown in Fig.5.2b.

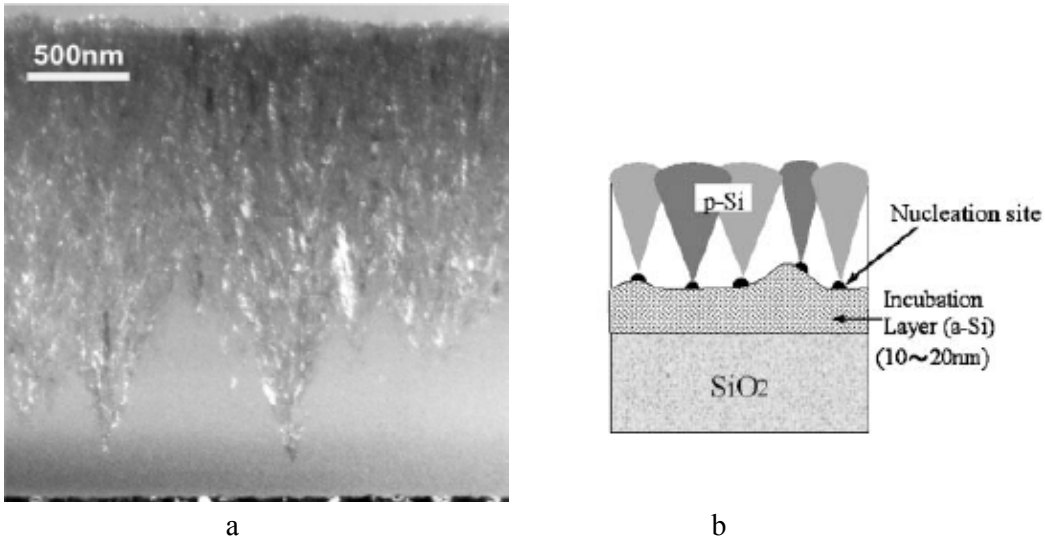

Fig.5.2. a. XTEM picture of typical μc-Si:H material deposited by PECVD on a SiO_2 surface; b. schematic diagram for the three different regions (after Kirimura *et al.* [3])

Depending on the substrate and deposition conditions, such as H_2 dilution ratio, reaction gas pressure and substrate temperature settings, the thickness of each region can vary in a wide range. In a low pressure, low substrate temperature (< 200 ^oC) and very high H dilution condition (gas flow $H_2/(H_2+SiH_4)>100$) typically used in obtaining p-type μc-Si:H by PECVD, the thickness of the first two regions are strongly reduced compared to that shown in Fig.5.2. However, with a thickness limit of only 10 ~ 20 nm for a p-type μc-Si:H layer in thin film silicon solar cells, to achieve an optimized p-layer crystallinity is not a easy task. Careful control on all the deposition parameters is needed.

With conventional dopant source gases, i.e. trimethylboron (TMB) or diborane (B_2H_6), it is difficult to completely avoid the amorphous incubation region in the p-layer and achieve a dense, single phase μc-Si:H p-layer. One of the reasons is that boron was found to hamper the crystalline growth in PECVD process [4]. Reasonable good quality μc-Si:H p-layers with a considerably reduced incubation phase can, however, be obtained by adjusting deposition parameters, using higher plasma frequencies, i.e., VHF, or other deposition methods, such as ECR-CVD [5] and Photo-CVD [6]. However, those techniques were found to be successful mainly on TCO substrates [7]. On top of device quality amorphous a-Si:H, silicon nucleation was found to be very hard [8]. A study performed with real time ellipsometry spectroscopy suggests that this is probably related to the difficulty in forming a proper compressive stress needed for the initial grow of μc-Si:H. [9].

Among all the approaches that have been proposed so far, the layer-by-layer technique (also known as chemical annealing) is very successful in making good quality thin μc-Si:H layers [10,11,12,13,14] and can probably completely overcome the amorphous incubation phase. In this process, amorphous silicon growth from a silane and hydrogen mixed gas plasma is alternated with hydrogen plasma treatments. The crystal nucleation is induced by the in-diffused atomic hydrogen in the sub-surface of the growing layer [14]. However, the application of this method is strongly limited by its time consuming process, since typically 10 to 20 cycles are needed for a 20 nm μc-Si:H p-layer and in each cycle a switch between gas sources and a pump-off of the used gas are normally needed , which makes it unfavourable for industrial application [14].

The difficulty of nucleation on the device quality amorphous silicon surface can probably be avoided also by using a BF_3 (boron trifluoride) as the dopant source gas instead of TMB. In a publication as early as 1986, Guha *et al.* [15] reported an improved multijunction n-i-p cell performance with thin μc-Si:H doped layers (both p and n layers). The improvement in the energy conversion efficiency was attributed to the use of fluorinated dopant gases which was believed to have enhanced the silicon nucleation at low substrate temperature [15]. Although some doubt had been aroused regarding the thick samples originally used for the characterization, proofs have been found by other groups that using fluorinated gases in the plasma may indeed introduce less trouble in silicon nucleation than using trimethylboron or diborane. Researchers at Penn State University, for example, performed an in situ spectral ellipsometry study on the p-μc-Si:H growing process on top of device quality hydrogenated amorphous silicon (a-Si:H) with three different dopant gases, i.e. B_2H_6, TMB and BF_3. Their results showed that BF_3 provides a broad range in parameter space, in which a dense, single phase μc-Si:H p-layer can be deposited on device quality amorphous silicon. Using TMB, one can also obtain μc-Si:H p-layers with reasonable good quality, but the space for obtaining such a layer with a thickness smaller than 20 nm is limited to a narrow range [16]. This difference in the deposition parameter spaces is attributed to 1) difference between bond energies of the B-F bond and the B-C bond; 2) opposite roles that fluorinated radicals and carbon containing radicals play in silicon nucleation process. As a result, when using BF_3, various doping levels can be used in combination with high plasma power density to obtain a thin, dense, single phase boron doped μc-Si:H layer; using TMB, however, low power and low doping levels with a much narrower range of TMB/SiH_4 gas flow ratio has to be used in order to obtain a μc-Si:H p-layer with the same thickness and quality.

However, most labs have been trying to avoid using fluorinated gases in their research due to the erosion problem to vacuum systems caused by F_2, one of the resultants of plasma reactions. Therefore, B_2H_6 and TMB are still the mostly used doping sources for obtaining μc-Si:H p-layers. Compared with B_2H_6, TMB is more favoured by

researchers working in the labs due to its long term stability. It was found, with conventional RF-PECVD and hydrogen diluted silane and TMB gases, that ~20 nm boron doped μc-Si:H could be achieved on top of amorphous silicon with a porous structure [17]. This finding later generated a technique that employs a low temperature high hydrogen content a-Si:H layer with a porous structure as a p/i buffer layer in the n-i-p cells. At this location, the inserted buffer layer works both as an electron back diffusion barrier and as a silicon nucleation promoter for the p-layer. Besides this technique, H plasma treatment on the i-layer surface is also found to be helpful in reducing the induction time needed to start the nucleation. Nevertheless, the difficulty in the controllability of the material quality caused by the narrow parameter space is not yet solved.

In the above discussion, the property of the substrate surface on which the p-layer is deposited plays a very important role. In Fig.5.3, the influence of substrates on the p-layer structure is illustrated. The figure shows normalized Raman spectra of a 25 nm p-layer sample grown on a Corning glass substrate (sample A), and on a 20 nm proto-Si:H i-layer deposited with HWCVD in identical conditions (sample B). The existence of a sharp 520 cm^{-1} peak (c-Si TO vibration mode) in the plot of sample A indicates its strong crystalline structure, whereas in that of sample B no crystalline Si peak is observed, indicating its purely amorphous structure.

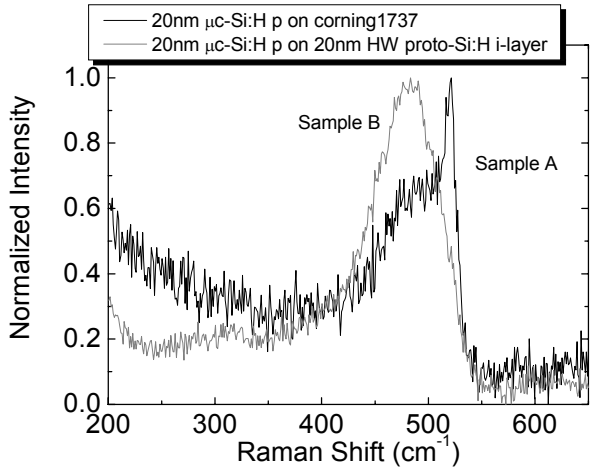

Fig.5.3. Raman scattering spectra of 20 nm p-layers made in a μc-Si: H condition on Corning 1737 glass (sample A, black curve), and on Corning 1737 glass with 20 nm HWCVD proto-Si: H layer (sample B, grey curve).

5.2 Influence of p-layer structure uncertainty on n-i-p cells: Observation of contact barriers in proto-SiGe:H n-i-p cell caused by the p-layer structure variation

In the previous section we have discussed the structure dependence of the electrical properties of p-type μc-Si:H material. We have also mentioned the influence of deposition techniques on the material quality. In the following sections, we will focus on the p-layers made by conventional RF-PECVD with a gas mixture of SiH_4, H_2 and TMB, the most commonly used fabrication process, and the influence of their properties on the output performance of n-i-p cells.

In a plasma reaction, a set of parameters, namely gas pressure, hydrogen dilution ratio, silane and dopant gas ratio, substrate temperature and plasma power density etc., form a parameter space that determines the material quality. We have discussed that the chemical and physical properties of substrates also influence the material quality. For the very thin p-type μc-Si:H material it is critical to remain in the narrow parameter space for obtaining desired layer quality. If the deposition parameters drift away from the optimized condition, material quality may end up in either of the three regions, namely the a-Si:H like incubation region, porous region, and dense μc-Si:H region. For plasma reactions involving TMB and high hydrogen diluted SiH_4, this is often the case. Since the internal field distribution in the cell critically depends on the electrical properties of doped layers and the interfaces they form with the adjacent layers, the complete cell parameter set, V_{oc}, FF, J_{sc}, diode factor n and reversion saturation current J_0, will then be influenced by this p-layer structure variation.

This influence, however, depends on the type of cells involved. In the triple cell structure we are discussing (see Chapter 7), where p-type μc-Si:H layers are used in all three subcells, the biggest influence was found to be on the middle cell, the proto-SiGe:H n-i-p cell. This section therefore discusses the structural effects of the p-layer on this cell.

5.2.1 Experiments

Proto-SiGe:H cells were grown in the n-i-p sequence and had the following structure: substrate/ n-a-Si:H / intrinsic proto-SiGe:H/ p-μc-Si:H/top contact. The substrate was Asahi U-type TCO glass coated with Ag and ZnO layers, which were sputtered without additional heating. All silicon layers of the cells were deposited by means of 13.56 MHz plasma-enhanced chemical vapour deposition (PECVD) in the multi-chamber UHV PASTA system. Transparent conductive oxide (TCO) layers, i.e. indium tin oxide (ITO) and zinc oxide (ZnO), were deposited in SALSA, a magnetron

sputtering system. The top contact was either ITO with Ag/Al metal grids or evaporated, semi-transparent palladium. The active cell area for the ITO contact was 0.13 cm^2; for the Pd contact it varied from 1 to 4 mm^2. Unless indicated otherwise, an ITO contact was used.

The intrinsic proto-SiGe: H layers were deposited at a calibrated substrate temperature of 195ºC with a thickness of about 150 nm, including an exponential germanium grading on the p- and n-side [19]. Boron-doped Si p-layers were deposited at 160ºC with a thickness of around 25 nm. Conventional 30 nm n-a-Si:H layers were used. A thin wide band gap intrinsic a-Si:H buffer layer is present between the p- and i-layer. The accuracy of the calibrated temperatures is ± 5ºC.

Annealing experiments on cells were performed in an oven with a N_2 gas inlet. A temperature of 180°C ± 5 °C was used for an annealing time of 20 minutes. P-layer samples on glass were annealed and measured in vacuum.

5.2.2 Results

A typical light *J-V* curve of a standard proto-SiGe:H n-i-p cell as it was at the start of the investigations in this section, is represented by the grey dashed line in Fig.5.4. The main characteristic of this curve is the big S-shape (a barrier), which leads to low values of V_{oc} and *FF*. To improve the cell characteristics, the material properties of the intrinsic layer were checked carefully. The major properties for samples made on Corning 1737 glass and with a thickness around 130 nm are as follows: the dark- and photo-conductivities are 1.4 x 10^{-10} $(\Omega\ cm)^{-1}$ and 1.7 x 10^{-6} $(\Omega\ cm)^{-1}$, respectively, the optical band gap (Eg) is about 1.5 eV, the activation energy (Ea) is 0.65 eV, and the minority carrier diffusion length, obtained by steady state photocarrier grating (SSPG) measurements, is 95 nm. These values are in good agreement with those of a device quality proto-SiGe:H material [19,20]. When the proto-Si:H material was tested in a series of solar cells with a p-i-n structure, no S-shape was observed. The best cells in this series showed V_{oc} and *FF* values of 0.71 V and 0.625, respectively. This means that it is highly unlikely that the S-shape is due to the i-layer, leaving the doped Si layers, the ITO and the interfaces to be studied.

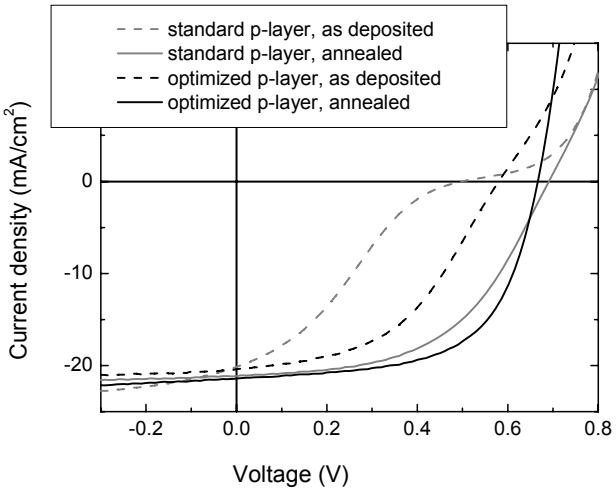

Fig.5.4. Light *J-V* characteristics of a proto-SiGe:H n-i-p cells with our standard p-layer (grey lines) and a re-optimized p-layer (black lines); the dashed lines represent the as-deposited cells, solid lines characteristics after annealing.

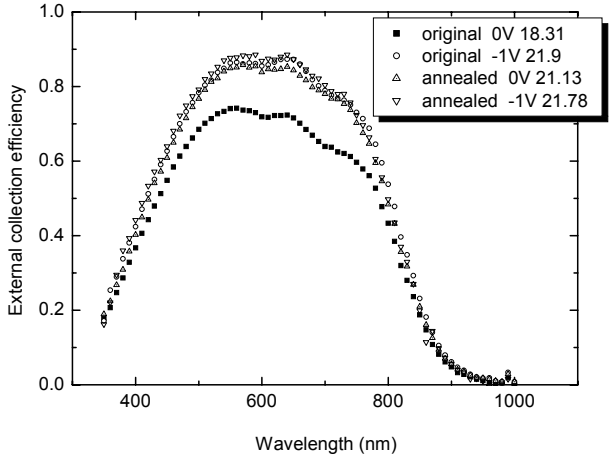

Fig.5.5. ECE measurements with and without -1V bias voltage on the same cell before and after annealing. Numbers are in mA/cm^2.

It was found that the S-shape can be removed by the post-deposition annealing process described in the experimental section. A *J-V* curve of an annealed cell is given by the grey solid line in Fig.5.4a. Notice that the complete cell structure was annealed, including the ITO/Ag/Al top contact. ECE measurements without bias voltage on the same cell before and after annealing (Fig.5.5) showed that the spectral response in the whole spectral range had increased after annealing.

Table 5-2 Overview of a series of annealing experiments on n-i-p cells with a proto-SiGe:H i-layer, in which the top contact material and moment of annealing were varied; Pd means palladium, as dep. means as-deposited, cold and hot ITO means ITO sputtered without and with substrate heating, respectively, where the calibrated substrate temperature was 180±15°C.

Experimental conditions	**Shape of the light *J-V* curve**
as dep. n-i-p +Pd	large S-shape
as dep. n-i-p + Pd + annealing	small S-shape
annealed n-i-p + Pd	small S-shape
as dep. n-i-p + cold ITO	large S-shape
as dep. n-i-p + cold ITO + annealing	small S-shape
as dep. n-i-p + hot ITO	small S-shape
annealed n-i-p + cold ITO	large S-shape
annealed n-i-p + cold ITO + annealing	small S-shape

Table 5-2 lists the experiments and results of a systematic annealing study on a series of n-i-p samples. It can be observed that: a) for all n-i-p cells made with "cold" ITO (ITO is sputtered without substrate heating), the *J-V* curves showed an S-shape, which can be largely removed by annealing; b) as-deposited n-i-p cells with a Pd contact show a big S-shape, cells annealed before Pd contacting only show a small barrier. It follows that annealing largely removes the S-shape.

5.2.3 Discussion

5.2.3.1 Annealing experiments:

The S-shape in the light *J-V* curves of the as-deposited n-i-p cells indicates that there is a barrier for the photocurrent. The photo-carriers cannot pass it without the help of an external voltage, as is shown by the grey dashed line in Fig.5.4a. The observed increase of the ECE in the whole spectral range after annealing (Fig.5.5) points at a possible internal field collapse in the as-deposited cell, at a charge carrier barrier at the p-side (holes) or n-side (electrons) of the cell, or at a combination of these options. Considering that the annealing temperature of 180°C is below the deposition temperature of the proto-SiGe:H i-layer and that the annealing time is far shorter than the i-layer deposition time, the origin of the S-shape and reduced charge carrier collection before

annealing must be located at the p-side of the cell. Otherwise, it should have been annealed out during the i-layer deposition.

From the series of annealing experiments as summarized in Table 5-2, it can be concluded that there are two barriers in the as-deposited cells that are topped with cold ITO. From the results of the cells with a Pd contact it is clear that one of these barriers is present within the n-i-p layer stack. As argued above, such a barrier is very likely located at the p-side of the cell, which means either at the p/i-interface or within the p-layer. Since the annealed n-i-p structure with the cold Pd contact works well, there is no obvious contact problem between Pd and the p-layer. The second barrier is induced by the cold ITO sputtering. This barrier can be resolved by either annealing the entire cell structure with ITO on top or by sputtering hot ITO.

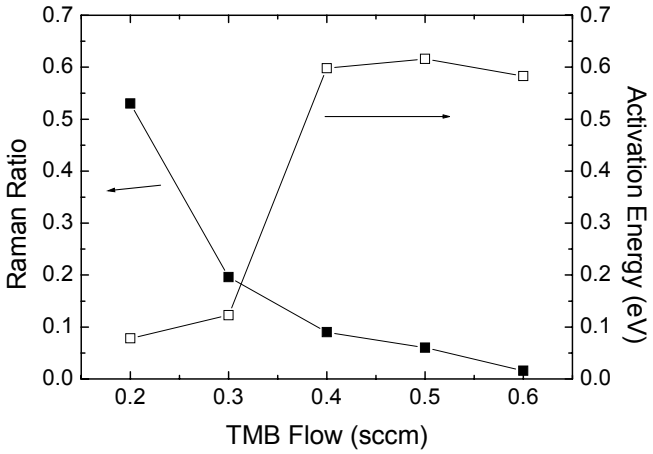

Fig.5.6. Raman crystalline ratio (solid squares) and activation energy (open squares) for p-layer samples on Corning 1737 glass with a thickness of 25nm ± 5 nm, that have been deposited with a range of TMB-flows. The layer thicknesses were determined by fitting of optical reflection-transmission spectra; the lines are a guide to the eye.

5.2.3.2 Study on the p-doped silicon and ITO material

A study on the p-layer material pointed out that the conductivity of our standard p-layer, which is deposited closely to the amorphous-to-microcrystalline phase transition and optimized for n-i-p cells with a proto-Si:H i-layer, was too low. Fig.5.6 shows the structural (Raman crystalline ratio) and electrical (activation energy) changes for a series of 25 nm ± 5 nm thick p-layer materials deposited onto Corning 1737 glass, for which the TMB flow was varied. From this, it is found that the p-layer of the cell, represented by the dashed and solid grey lines in Fig.5.4, was made with a too high TMB flow. As a

result, the layer was amorphous instead of microcrystalline. Consequently, the doping level of the layer is far too low, which cannot provide an internal field that is strong enough for efficient photocarrier extraction from the SiGe:H i-layer. Annealing experiments at 160°C on the amorphous p-layer on glass showed an increase of the conductivity, which is translated in the cell into a more efficient charge carrier extraction.

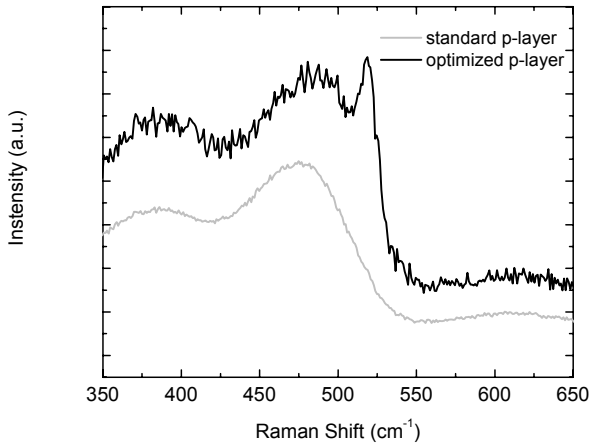

Fig.5.7. Raman spectra of n-i-p cells with a standard (grey line) and optimized (black line) p-layer; besides the p-layer, the cells are identical**.**

By optimization of the p-layer deposition, a highly conductive μc-Si:H p-layer was obtained. Results of Raman spectroscopy measurements on two cells, one with a standard and one with a newly optimized p-layer are shown in Fig.5.7. The measurements were performed from the p-side of the cells on the areas without top contact. It can clearly be seen that the cell with the optimized p-layer shows a strong peak near 520 cm^{-1}, which means it has a highly crystallized structure, whereas the spectrum of the standard p-layer does not.

Using this layer in a proto-SiGe:H n-i-p cell with Pd contact, no large barrier was observed. With a cold ITO/Ag/Al contact, however, a small barrier can still be seen (Fig.5.4a, dashed black line), which can be removed by annealing (solid black line). Some insight into the origin of this vanishing of the small barrier upon annealing comes from annealing of the optimized p-layer sample on glass. The conductivity of this sample, which had an initial activation energy of about 0.08eV, was found to have increased after annealing. From the schematic band diagram of the p/ITO interface in Fig. 5.1., it can be understood how this can improve a cell's *J-V* characteristics. The existence of the band discontinuity at the valence band edge of the p- and ITO layers causes a depletion region in the p-layer. In order to recombine with electrons at the ITO/p-layer interface, holes

have to pass this region. If the region is too thick, it can be a barrier to the hole transport; if it is sufficiently thin, the holes can tunnel though it. An increase of the p-layer conductivity due to annealing decreases the depletion region width, which facilitates the passing of holes and, consequently, improves the *J-V* characteristics. In addition to this explanation of the improved *J-V* curve upon annealing, changes of the ITO properties and the ITO/p-layer interface may also be involved. Because the ITO conductivity greatly exceeds that of the p-layer, an improvement of it is not likely to have a strong influence on the depletion layer in the p-layer. For a comprehensive understanding of the observations, a supplementary study is required.

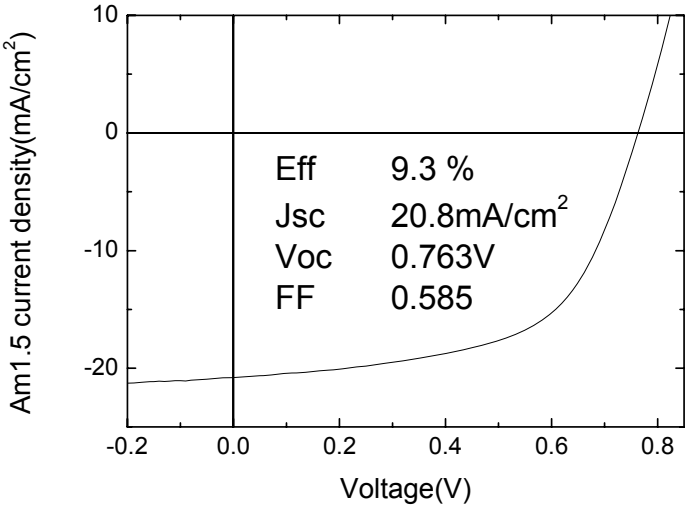

Fig. 5.8. AM1.5 *J-V* characteristics of a single junction n-i-p cell with a SiGe:H i-layer made by PECVD. I-layer band gap is around 1.6 eV.

For a cell stack with the newly optimized p-layer, which was annealed after being topped with a room temperature ITO/Ag/Al top contact, the following best cell parameters were measured: open circuit voltage: 0.667 V, short circuit current: 21.4 mA/cm2, fill factor: 0.61 and efficiency: 8.7%. Using the same type of p-layer and a ~1.65 eV bandgap proto-SiGe:H i-layer, an efficiency of 9.3 % was obtained, with an J_{sc}, V_{oc} and *FF* of 20.8 mA/cm^2, 0.763V, and 0.585, respectively. The AM1.5 *J-V* characteristics of the later cell are shown in Fig. 5.8.

5.2.4 Summary of this section

By performing systematic annealing experiments, an S-shape in the *J-V* characteristics of our proto-SiGe:H n-i-p configured cells was found to be due to the

influence of two barriers: one was located at the p/i interface, the other one was related to the room temperature sputtering of the ITO top contact.

Further analysis with Raman spectroscopy and activation energy measurements pointed out that the deposition conditions of the p-layer were not optimal and led to an amorphous, instead of a microcrystalline, layer. Optimization of the p-layer resulted in a large improvement of the *J-V* characteristics. Annealing was shown to improve the cell characteristics of both the cell with the standard and the one with the improved p-layer, which is likely due to an observed recovery of p-layer microcrystalline structure. By re-optimizing the p-layer deposition condition, the best cell with an i-layer bandgap of 1.55eV had an efficiency of 8.7%. Using the same type of p-layer and a ~1.65 eV bandgap proto-SiGe:H i-layer, an efficiency of 9.3% was obtained.

5.3 Dark J-V studies on the n-i-p cells with unoptimized p/ITO/Ag stacks

As it is reported in the previous section, an un-optimized p/ITO/Ag stacks may cause a detrimental effect on the light *J-V* characteristics of proto-SiGe:H (a-SiGe:H) cells. In this section, we further analyse the influence from the quality of p/ITO/Ag region on SiGe:H cell properties by means of dark *J-V* studies, and compare it with that observed on μc-Si:H and proto-Si:H n-i-p cells. As a benefit of this study, an insight of dark *J-V* (J_{dark}- V) characteristics of all three types of cells was obtained.

5.3.1 Short introduction about dark *J-V* characteristics

The solar cell dark *J-V* characteristics under forward voltages ($0<V<V_{bi}$, where Vbi is the build in voltage of the p-i-n diode) give information on current losses during the carrier transport within the cell structure, which includes all the metal and semiconductor layers and interfaces that are present in-between top and bottom contacts. Assuming the contacts on both sides of the cell to be Ohmic, we shall expect an exponential *J-V* relation as it is described in Chapter 2 with diode equation (2.11), with a characteristic diode quality factor *n* and saturation current density J_0. In the semi-logarithmic axes, this shall look like a straight line. From *n* and J_0, one can roughly estimate the V_{oc} with formula

$$V_{oc} = \frac{nkT}{q} \ln\left(\frac{J_{sc}}{J_0} + 1\right) \qquad (5.3),$$

assuming the series resistance is small and shunt resistance is large, so that both can be neglected. The differential diode quality factor n (V) (V>0) under dark condition can be deduced from the dark *J-V* measurement, namely

$$n(V) = \left[\frac{kT}{q} \frac{d \ln J_D}{dV} \right]^{-1} \qquad (5.4),$$

where k, T, q, J_D and V are Boltzmann constant, absolute temperature, elementary charge, dark current density and bias voltage respectively. Studying on the n (V) values allows one to obtain information on the limiting current transport mechanism in a pn (p-i-n) junction [21].

5.3.2 Effect of post deposition annealing on the dark *J-V* characteristics of proto-Si:H and μc-Si:H n-i-p cells

Before we further discuss the dark *J-V* of the problematic SiGe: H n-i-p cells, we first look at the J_{dark}-V curve of a μc-Si: H cell and a proto-Si: H cell. It was found that for many of the proto-Si:H and μc-Si:H n-i-p cells, post-deposition annealing also improves the cell output characteristics largely, though no S-shapes were observed in their original light *J-V* curves. Fig. 5.9 shows an example of the post-deposition annealing effect on the AM1.5 *J-V* characteristics of both types of cells.

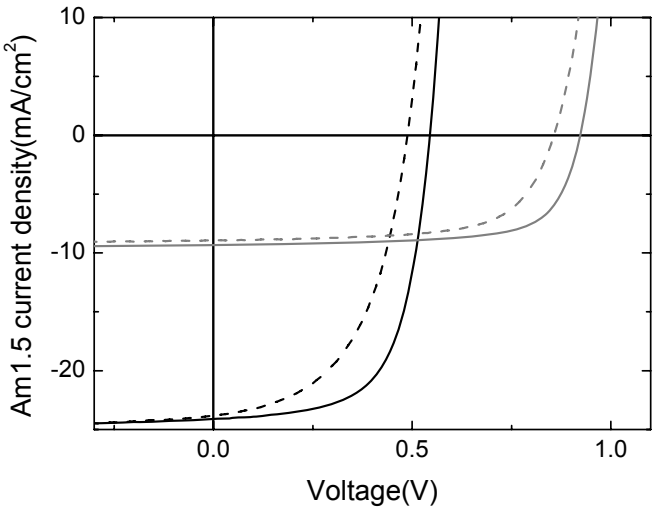

Fig. 5.9. AM1.5 *J-V* characteristics of a single junction a-Si:H (grey lines) and a single junction μc-Si:H n-i-p cell (black lines) before (dashed lines) and after post-deposition annealing (solid lines). The i-lays for both cells were not fully optimized.

5.3.2.1 Three regions in the forward dark *J-V* characteristics

Fig.5.10 shows a J_{dark}-V curve of a proto-Si: H cell with a comparable p-layer made at the same deposition condition. We note here that "comparable" means that the p-layer and the p/i interface buffer layers used in all three type cells (proto-Si:H n-i-p, proto-SiGe:H n-i-p and μc-Si:H n-i-p cells) were made at the same deposition condition.

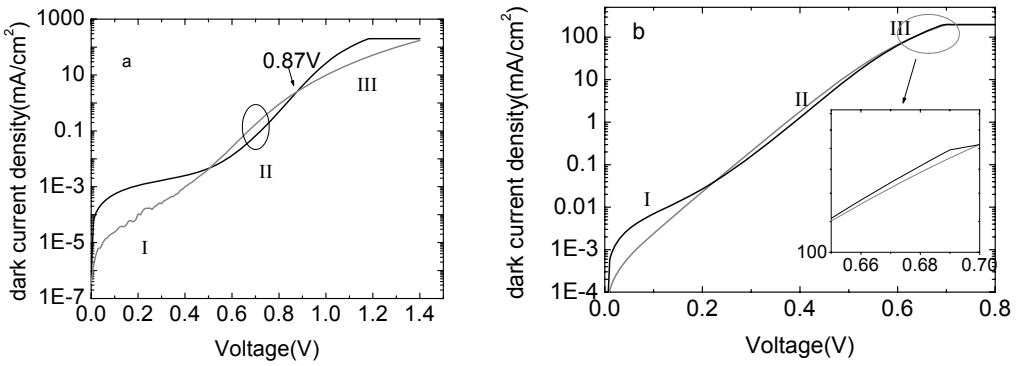

Fig.5.10. Dark *J-V* characteristics of a proto-Si:H n-i-p cell (a) and a μc-Si:H n-i-p cell (b). Both have a p-layer made at the same condition as that used in the proto-SiGe:H n-i-p cells. Grey line: before annealing; black line: after annealing.

Fig.5.10a and Fig.5.10b shows J_{dark}-V characteristics of a proto-Si:H n-i-p cell (a) and a μc-Si:H n-i-p cell (b). Both samples were deposited on stainless steel substrates with a Ag/ZnO rough back reflector. They represent for each type the typical behaviour of many hundred n-i-p cell samples that have been studied. The light grey and black curves indicate the J_{dark}-V of the same cell before and after annealing, respectively. From Fig.5.10a, one can see that after annealing (described in section 5.2.1) the changes in the J_{dark}-V curve can be observed in three regions, namely in the voltage range between 0V to around 0.5V (region I), between 0.5V and 0.87V (region II), and at the voltage above 0.87V (region III). Note that 0.87V is just about the V_{oc} of this sample measured under the AM1.5 sun light. In order to avoid the overheating of the solar cell by too high current flow through the device, the upper limit for the current density measurement was set at 200 mA/cm^2. Due to the built-in function of the source-measure unit (Keithley 238) used for this study, the voltage was fixed to the threshold voltage when the current exceeds this compliance limit. This results in a "saturated" current density in the J_{dark}-V plot. This current "saturation" caused the diminishing of the difference between the *J-V* curve of the annealed and as-deposited μc-Si:H cell in region III (Fig.5.10b). But in an enlarged graph, shown in the inset of Fig.5.10b, the current density enhancement for the annealed cell can be still seen. Except that the transition point from region II to region

III shifts to around 0.6 V, the shape of J_{dark}-V curve for the μc-Si:H sample is very much alike to that of the proto-Si:H cell (Fig.5.10a).

For clarity, we discuss here mainly the behaviour of the proto-Si:H n-i-p cell (Fig.5.10a). In region III, where the applied voltage is close and larger than the build-in potential (V_{bi}) of the n-i-p structure (which has a value close to V_{oc}), the dominating current losses are related to contact resistance, interface barriers and the i layer (dark-) conductivity. The first item, namely the contact resistance, results from the resistance of the ITO layer, contact resistance/barriers between ITO and Ag grids, and the resistance introduced by bad probing during the measurement. Since the contact between probes and Ag grids, and that between Ag and ITO were optimized and carefully checked for each measurement, the influence of annealing treatment on these two sources can be neglected. The ITO resistance includes two parts, namely the resistance for horizontally transferred current and that for vertically transferred current. Since the horizontal part is much more significant than the vertical part, we believe one can just characterize ITO properties by measuring its sheet resistance (horizontal) and neglect the influence of the other. This was done by both four probe resistance measurement and Room Temperature Hall measurement. The results did not show any systematic difference for samples measured before and after annealing [22].

Interface barriers, the second item listed, may come from that between i- and p-layers, p- and ITO layers, and ITO and Ag contact. Since the ITO and Ag contact has been optimized for all the depositions in our Group, we do not expect problems from this part. For the other two interfaces, we will soon discuss them in the following sub sections.

The i-layer conductivity, the third item that is related to the dark current density in region III, has its influence on the J_{dark}-V characteristics in the full voltage range. This gives the main difference between Fig.5.10a and Fig.5.10b, in which the μc-Si:H cell shows generally higher dark current than the proto-Si:H cell, due to the different mobility band gap of the two i-layer materials. But for each identical cell before and after the annealing treatment, this influence can be only observed when the i-layer quality is changed by the treatment. Considering the temperature of this treatment (160~170 ^{o}C) was lower than that used to deposit the p-layer (190ºC) and the treatment time was only around 20 minutes, it is unlikely that i-layer quality can become dramatically better. This of course has to be checked by further experiments. But before we go into that, we first look to the other parts in the J_{dark}-V curves shown in Fig.5.10.

In region II where the applied voltage is below around V_{bi} and is well higher than 0V, ~ 0.5V in this case, the dark current is mostly limited by the carrier recombination at the interfaces (p/i and i/n) or within the bulk of intrinsic layer where the internal field is the lowest compared to those in the other parts of the cell. The lowering of J_{dark} for the

cells after annealing indicates the reduction of the carrier recombination. This can either be due to the improvements of interfaces or i-layer quality, or the enhancement of the internal electric field.

In region I, where the applied voltage is close to zero, the shunting current can not be neglected anymore, due to the existence of cracks, pin holes or other shunting paths. Therefore in this region, the dominating current is a combination of shunting current and the carrier recombination current. The fact that J_{dark}-V plot after annealing shows increased values compared to the original plots indicates that at least one of these two currents has increased after the treatment. This can not be due to the increase of recombination current, since in that case the J_{dark} value in region II would also be increasing, and that is not the case. Therefore an enhanced shunting current is the cause for the observed increase of J_{dark} in region I.

The increase of shunting current might be due to an increase of the density of cracks introduced by the rapid temperature changes at the beginning and at the end of the annealing treatment. Conductive elements, such as B or P from the doped layers, Ag from top or bottom contacts and indium from the ITO top contacts may then diffuse through these cracks and increase the shunting current. Such elements may also move in the already existing shunting paths (the pin holes, for instance), which causes the same effect.

The effect of J_{dark} increases in region I after annealing was more enhanced when strong stresses exist in the cell, which is the case of μc-Si:H samples. For the samples we have measured, several hundreds μc-Si:H n-i-p cells, an increased shunting current (decreased dark R_{sc}) is observed after annealing. For the proto-SiGe:H cells that have been studied, also a few hundreds, the number of cells of which dark R_{sc} decreases after annealing was somewhat lower, but still at a very high level. The reason for that, we believe, is related to the much thinner i-layer, only around 100 nm, used for this type of cell. Rough substrates such as textured TCO glass with Ag/ZnO coating, unpolished stainless steel and stainless steel covered with rough Ag/ZnO, were widely used in this study, which enhanced the formation of shunting paths within the cell. Nevertheless, many proto-SiGe:H samples did not show any increases in dark R_{sc} after annealing, which indicates the much relaxed structure of this material.

5.3.2.2 Influence of post deposition annealing on each region of forward dark *J*-*V* characteristics of the solar cells

Now we turn back to the discussion on the causes of the improvement on solar cell properties upon annealing. Regarding the interface influences, changes from most of the interfaces can be taken out from our consideration. Those are the interfaces between

Ag/ZnO, ZnO/n and n/i. The reason is clear: during i-layer deposition, all the interfaces that may change with temperature have already changed. For the same reason, changes from any of those layers, Ag, ZnO and n type μc-Si:H can be also ruled out. What is left (not annealed during the i-layer deposition) are the p, i, ITO layers and the two interfaces in between.

For the p-layer, we have shown in the section 5.2 that its conductivity can change when doping level is increased as a result of annealing. Was this the reason for the dramatic improvement of the cell properties? We are not sure yet.

What we see from J_{dark}-V curve is the reduction of recombination current, which depends on parameters including: the band structure (band gap) of the i-layer and its alignment with that of p-layer, the densities of defects at the p/i interface as well as the bulk i-layer, the built-in potential (V_{bi}), which depends on the band structure of p, i, n layers and the p-layer doping level (if n-layer properties remain unchanged).

Changes of material bandgaps during the treatment is unlikely, since the annealing temperature was far lower than that needed for structural rearrangement of Si atoms. The possibility of decreases in defect densities in i- and p/i region, however, can not be ruled out. It is possible that the reduction of the p/i interface defect can be the cause for the lowering of carrier recombination current (Fig.5.10, region II) and the consequent increases of V_{oc} and FF (Fig.5.4). This might be the case, since the interfaces (including the p/i interfaces) are typically more defective. But we then need to figure out what can cause this improvement. It has been proposed that hydrogen may move during the annealing treatment on the a-Si:H based solar cells at a temperature as low as 200 ^{o}C. For a light soaked a-Si:H solar cell this could be the case, since during the light soaking, a high density of Si dangling bonds is created and these bonds can be reconnected with hydrogen during annealing. However, in the experiment we are discussing here the low temperature p/i buffer layer has actually much higher hydrogen content than any adjacent layers and does not have a chance to break their bonding with Si atoms yet. If H moves during annealing, it will only leave more dangling bonds in this region, which then increase the recombination current. But this is against our observation: the dark current density actually decreases. Therefore, it is unlikely that the movement of H atoms is the reason for the significant improvement of n-i-p cells.

5.3.2.3 Annealing experiment on μc-Si:H n-i-p cells before ITO depositions

To study if the annealing treatment has any effect on the p/i region, we performed the following experiment. Two μc-Si:H n-i-p cell samples were made on SS substrate, one was annealed before the ITO deposition, and one was not. ITO contacts were sputtered on both samples at room temperature. The IV data for both samples were

compared and are shown in Fig.5.11 (dark *J-V*) and Fig.5.12 (AM1.5 *J-V*). The pre-annealed cell, the one that had been annealed before the ITO deposition, shows the same *FF* and V_{oc} as the one without pre-annealing (Fig.5.12). Post-annealing treatment increased the V_{oc} and *FF* of both cells to values comparable to other µc-Si:H cells made at same conditions. To avoid the possible influence of i-layer thickness differences, Fig.5.11 only shows the dark *J-V* characteristics of the cells at a comparable position [23] on the two samples. One can see that the J_{dark}'s are almost exactly the same for the two cells in a wide range when V >0.2 V. Below 0.2 V, the cell with pre-annealed n-i-p structure shows a somewhat larger shunting current than the one without pre-annealing.

This experiment clearly indicates that the barrier which causes a low V_{oc} in the light *J-V* characteristics of the µc-Si: H cell is not related to the p/i interface or the p- and i-layer itself. Therefore, it is only related to the ITO/Ag or p/ITO interface. Moreover, the fact that the J_{dark}-*V* curves of both the as-deposited cells and the cells with annealed n-i-p structure overlap each other, and the fact that the J_{dark}'s of both cells decrease with the same amount in the medium forward bias voltage range (MFBV), or region II in Fig.5.11b, of the dark *J-V* plots after post-anneal prove that the model that we use to analyse the dark *J-V* curve of µc-Si:H cells is valid. Namely, recombination is the one of the main carrier transport mechanism in the MFBV region, the reduction of which, due to the enhancement of the internal electrical field by improved Ag/ITO/p region after annealing, leads to the large improvement of solar cell output properties. Since we sputter ITO layers under the same conditions for all three type of cells, this barrier most likely exist in all these cells. A careful study on the annealing experiments shown in Table 5-2 proves that the contact between Ag and ITO is not the cause of the barrier; the barrier is at the contact between p and ITO (deposited at the "cold" condition).

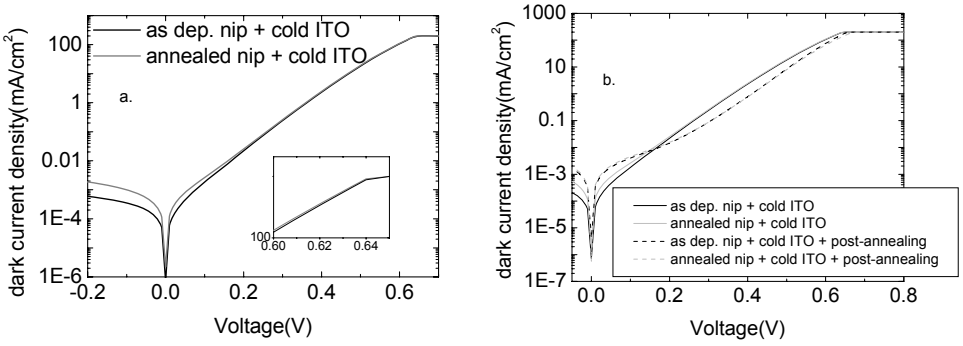

Fig.5.11. Dark *J-V* characteristics of two µc-Si: H n-i-p cells with identical deposition condition. Both were coated with room-temperature-sputtered ITO, and annealed (post-annealing) with top contact. One was also annealed before the ITO coating (grey lines).

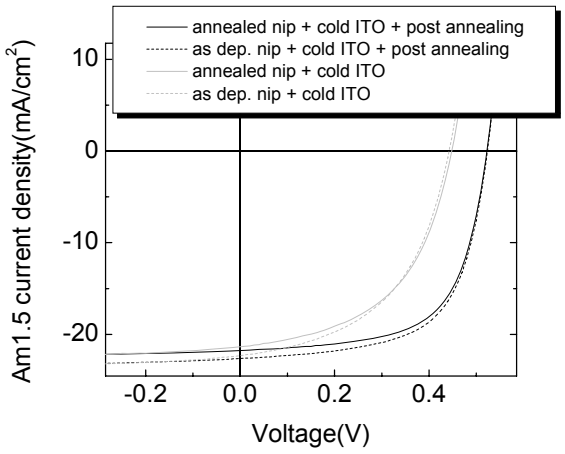

Fig.5.12. AM1.5 *J-V* characteristics of the μc-Si: H n-i-p cells shown in Fig.5.11.

5.3.3 Dark *J-V* study on annealed proto-SiGe:H cells.

Now we turn to the analysis of the dark *J-V* characteristics of proto-SiGe:H. Fig.5.13a shows the dark *J-V* characteristics of SiGe:H n-i-p cell with an unoptimized p-layer. Using semi-logarithmic axes, the *J-V* plot is curved for the cell before annealing. A weak exponential region can be observed at a voltage around 0.9 V, which gives a diode quality factor of about 2.9. After annealing, a plot with a clear exponential region is observed at a voltage around 0.3 V, with a reasonable *n* value of 1.7. The differential diode quality factor n(V) plots for this cell (also for the cell being discussed later) was calculated using the equation (5.4) and are shown in Fig.5.13b (and Fig.5.14b). In Fig.5.13b, the weak exponential region (near 0.9 V) of the *J-V* characteristics of the original cell (Fig.5.13a, solid line) appears as a valley. A bump can be clearly observed in the voltage range between 0.1 and 0.9 V. The *n* value that shall characterize the SiGe:H p-i-n junction (normally with *n* between 1 and 2) is not present, due to the too low injection current through the barrier existing at the p/ITO interface [24]. After the annealing treatment, the p/ITO contact is improved, and the carrier transport barrier near that region is largely removed. As a result, the exponential region in the dark *J-V* characteristics appears, and the curve looks “normal” again (Fig.5.13a, dotted line). The existence of a shoulder on the curve of the annealed cell at the voltage around 0.9V (Fig.5.13b, dotted line) indicates that the barrier is not completely removed by the post annealing treatment.

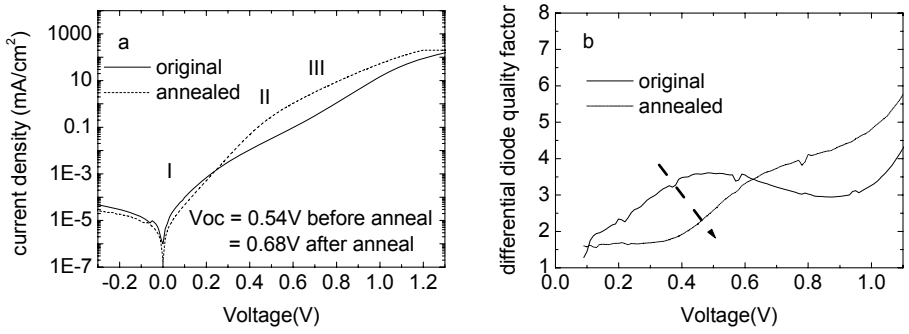

Fig.5.13. a. Dark *J-V* characteristics of a typical proto-SiGe:H n-i-p cell with unoptimized p-layer before and after annealing treatment. b. The $n \sim V$ plots of the same sample shown in a.

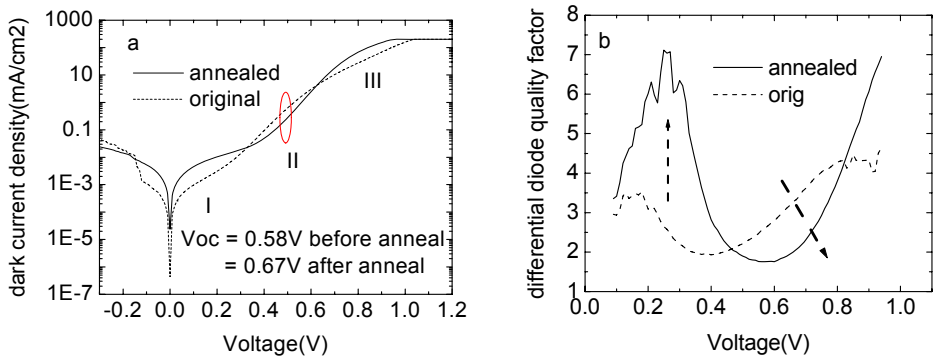

Fig.5.14. a. Dark *J-V* characteristics of a typical proto-SiGe:H n-i-p cell with optimized µc-Si:H p-layer before and after annealing treatment. b. The $n \sim V$ plots of the same sample shown in a.

Fig.5.14 shows the dark *J-V* characteristics of a SiGe:H cell with the re-optimized µc-Si:H p-layer. The J_{dark}-*V* plots in the semi-logarithmic axes (Fig.5.14a) clearly show a linear shape in the voltage range between 0.4 V and 0.6 V; *n* values of 1.9 and 1.7 are estimated for the cell before and after annealing (Fig.5.14b). *J-V* characteristics of this cell under AM1.5 sun light are shown in Fig.5.4 by dashed and solid black lines. Clearly, no S shape is present for the as-deposited cell, and the *FF* is improved further upon post-deposition annealing.

To see the difference more clearly, the J_{dark}-*V* curves for the annealed cells are re-plotted in Fig.5.15 by solid grey (cell with the un-optimized p-layer) and black (cell with the optimized p-layer) lines. The black dashed line is the fitted *J-V* curve for the latter without considering the influence of the shunting current.

The dramatic difference between the dark *J-V* characteristics of the SiGe:H cells with an un-optimized p-layer (represented by Fig.5.13) and with an optimized µc-Si:H p-layer (represented by Fig.5.14) may be explained by considering the different degree of

band discontinuity at the p/i interface. Throughout this research, we used medium bandgap proto-SiGe:H i-layers with Ge grading near the p and n sides of the i-layer. The deposition conditions for both the i–layers and the Ge grading layers are identical for the two cells shown in Fig.5.13 and Fig.5.14. Due to the unintentional change of the p-layer structure, the electrical properties of this layer, such as the doping level and the mobility bandgap, can be quite different, resulting in a different band alignment at the i/p interfaces of these two cells. It is likely that the cell with the unoptimized p-layer has a much larger band misalignment at the p/i interface than the cell with an optimized p-layer, resulting in a large potential barrier for carrier transport through that region. This may have two consequences: first, the electric field in the bulk SiGe:H i-layer becomes weak, which results in an enhanced dark recombination current in low forward bias voltage range (LFBV, 0 ~ 0.4V in Fig.5.13 and Fig.5.15); second, in the medium forward bias voltage range (MFBV, 0.4 ~ 0.65V in Fig.5.13a), dark current is no longer limited by the bulk recombination but by the transition current through this barrier, which appears as a shoulder in Fig.5.13b. The influence of this barrier on the dark current density extends further to the higher voltage, resulting in a much lower dark current density in HFBV, the drift current dominated region (Fig.5.15, V > 0.7 V). A higher R_{oc} is therefore observed on the AM1.5 *J-V* for this cell (Fig.5.4, solid grey line) compared to the one with an optimized p-layer.

From Fig.5.14, it is obvious that the annealed cell has a too high shunting current in the low forward voltage region (Fig.5.14a). On the n-V plot shown in Fig.5.14b, this is reflected by a large peak in the low forward bias voltage region (0<V<0.4V). The decrease of the shunting resistance upon annealing is likely due to the increase of shunting paths (cracks) resulted from the fast cooling treatment in the annealing process that was necessary to precisely control the annealing time for this study. Because of the existence of this large peak, the diode quality factor *n* may have been overestimated a bit. As a useful amending technique, the post annealing treatment is normally performed in a more gentle way. Therefore, the increase in the shunting current will be limited.

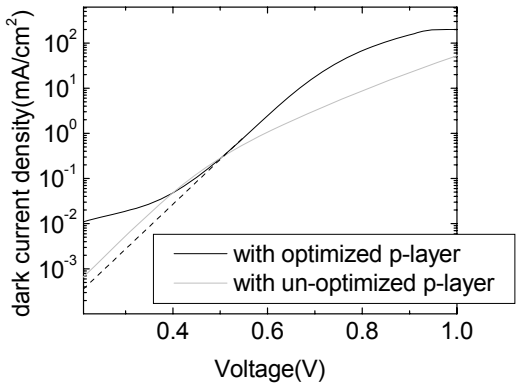

Fig.5.15. A re-plot of the dark *J-V* characteristics of the two annealed proto-SiGe: H cell shown in Fig.5.13 and Fig.5.14.

5.3.4 Summary of this section

The effect of annealing on three types of n-i-p cells, namely proto-Si:H, μc-Si:H and proto-SiGe:H n-i-p cells, was discussed by means of comparing their dark *J-V* characteristics before and after the annealing treatment. For the proto-Si:H, μc-Si:H samples and the SiGe:H samples with an optimized p-layer, three regions, namely the drift current dominated carrier transport region, i-layer recombination current dominated region, and shunting related region can be clearly recognized for the J_{dark}-V curves of the identical cells before and after annealing. For the cells that have been annealed with a ITO/Ag top contact, the J_{dark} in the recombination current dominated region are generally reduced, and are independent of the type of i-layer material. Study on the annealed μc-Si:H n-i-p cells before ITO deposition points out that this is likely due to the enhancement of the internal field in the i-layer which is caused by a reduction of the p/ITO barrier by the annealing treatment.

For single junction SiGe:H cells with an un-optimized p-layer, an extra current limiting mechanism exists which may be explained by considering a band mismatch at the p/i interface. This barrier can not be removed by the post-deposition annealing treatment; in the $n \sim$ V plot, it appears as a remaining shoulder start from a voltage below $\sim V_{oc}$.

Further, carefully performed dark *J-V* measurements have been proven to be a powerful tool in understanding the current limiting mechanism in thin film p-i-n (or n-i-p) diodes. More information can be attained if this measurement could be done in a higher

bias voltage range. A heat-sinking technique is then needed to avoid the sample being heated up by a too high current flow.

5.4 Conclusions

Carrier transport barriers were found in single junction thin film proto-SiGe:H, proto-Si:H and μc-Si:H n-i-p solar cells. By analyzing the results of detailed annealing experiments on proto-SiGe:H n-i-p cells, and on proto-Si:H and μc-Si:H n-i-p cells, the barriers are identified to be most likely located at the p/ITO interfaces of all the three types of cells and at the p/i interface of the proto-SiGe:H cells. The former can be removed by raising the ITO deposition temperature or by performing a post-deposition annealing treatment at a temperature below the p-layer deposition temperature; the later can not be removed by these treatments. A careful study on the dark *J-V* of identical cells before and after annealing treatment allowed us to gain insight in the carrier transport barriers near the top contact of an n-i-p structure. Studies of the $n \sim V$ plots have been proven to be an effective approach to identify the transport problems in such structures.

References

1. S. M. Sze, Physics of Semiconductor Devices, 2nd Edition. John Wiley & Sons, 1981.
2. http://www.cneu.psu.edu/amps/exampleParameters.html.
3. H. Kirimura, K. Kubota, E. Takahashi, S. Kishida, K. Ogata, Y. Uraoka, and T. Fuyuki, Jpn. J. Appl. Phys. 43 (2004) 7929.
4. K. Prasad, U. Kroll, F.Finger, A.Shah, J,L. Dorier, A. Howling, J. Baumann, M. Schubert, Mat. Res. Soc. Symp. Porc. 219 (1991) 383.
5. Y. Hattori, D. Kruangam, K. Katoh, Y, Nitta, H. Okamoto, and Y. Hamakawa, 19th IEEE PVSC, (1987) 689.
6. M. Konagai, H. Takai, W. Y. Kim, and K. Takahasi, 18th IEEE PVSC, (1985) 1372.
7. A. Dasgupta, A. Lambertz, O. Vetterl, F. Finger, R. Carius, U. Zastrow, H. Wagner, 16th Euro PVSEC, (2000) No. 477 VB 1/38.
8. J.K. Rath, R.E.I. Schropp, Sol. Energ. Mat. Sol. C. 53 (1998) 189.
9. H. Fujiwara, M. Kondo, and A. Matsuda, Mat. Res. Soc. Symp. Proc. 664 (2001) A1.2.1.
10. A. Asano, Appl. Phys. Lett. 56 (1990) 533.
11. H. Shirai, J. Hanna, and I. Shimizu, Jpn. J. Appl. Phys. 30 (1991) L881.
12. S. Hamma, P. Roca i Cabarrocas, Sol. Energ. Mat. Sol. C. 69 (2001) 217.

13. B. Park, R.V.R. Murthy, and S.G. Chamberlain, J. Vac. Sci. Technol. A 16 (1998) 902.
14. A.Gordijn, *Microcrystalline silicon for thin-film solar cells*, PhD thesis, 2005, Utrecht University, the Netherlands, 2005.
15. S. Guha, J. Yang, P. Nath and M. Hack, Appl. Phys. Lett. 49 (1986) 218.
16. Koh, Joohyun,. H. Fujiwara, R.J. Koval, C. R. Wronski, and R. W. Collins, J. Appl. Phys. 85 (1999) 4141.
17. J.K. Rath, and R.E.I. Schropp, Sol. Energ. Mat. Sol. C. 53 (1998) 189.
18. H. Li, R.L. Stolk, C.H.M. van der Werf, R.H. Franken, J.K Rath, R.E.I. Schropp, J. Non-Cryst. Solids 352 (2006) 1941.
19. R. Jimenez Zambrano, F.A. Rubinelli, W.M. Arnoldbik, J.K. Rath, R.E.I. Schropp, Sol. Energ. Mat. Sol. C. 81 (2004) 73.
20. A. Gordijn, R. Jimenez Zambrano, J.K. Rath, R.E.I. Schropp, IEEE T. Electron. DeV.49 (2002) 949.
21. Maarten van Cleef, amorphous crystalline silicon heterostructures and solar cells, PhD thesis, Utrecht University, 1998.
22. not published, R. Franken, Utrecht University.
23. For a short description on the cell configuration on each substrate, please refer to section 2.2.2.2.
24. J. Deng and C.R. Wronski, J. Appl. Phys. 98, 024509 (2005).

6

Photogating effect observed in microcrystalline silicon solar cells and its applications in cell optimization

As we discussed in the previous Chapters, quantum efficiency measurement is of great importance in solar cell characterization. Under the standard condition a solar simulator or a light source with a similar irradiation spectrum is used as a bias light, in order to form a proper internal electric-field distribution profile as it is under the standard working condition, i.e. under AM1.5 sun light. Due to the relatively weak current generated by the monochromatic light compared to that by the strong bias light, a lock-in technique is normally used to obtain a high signal to noise ratio. It is sometimes also beneficial to test the cell under a non-standard condition, for example using a coloured bias light instead of the standard white light, since this may give information that is normally hidden. By performing this experiment on μc-Si:H single junction n-i-p cells, we observed an interesting phenomenon - the photo-gating effect [1].

6.1 Introduction

Photogating: short description of its history

The name "photo-gating" refers to the observation of anomalously high quantum efficiency values in amorphous silicon p-i-n structure. It was proposed by the group at Pennsylvania State University in 1992 [2], but the effect was first reported in the 1980s already [3]. The main characteristics of this effect are the observation of anomalous high values in the spectral response for red or blue wavelengths when the external collection efficiency is measured under blue or red bias light condition respectively.

So far, the reports about the photogating effect observed on thin film Si p-i-n structure were all with an amorphous silicon (a-Si:H) absorber, especially a-Si:H that was degraded by light soaking. [2,3,4,5]. Enhanced quantum efficiency was also observed on CdS/CdTe solar cells [6,7,8]. Observation of a significant photogating effect has not been reported on μc-Si:H based p-i-n structures.

In this Chapter, we first report the observation of a strongly enhanced quantum efficiency for a μc-Si:H n-i-p cells measured with a coloured bias light, and show the experimental data of the dependence of this enhancement on the bias light intensity. Then we discuss the physics of this effect with computer simulation using computer code D-AMPS (Analysis of Microelectronic and Photonic Structures + New Developments)[9] and find the correlation between the simulation result and the experimental result. Further, we show the influence of cell deposition parameters on the observation of this effect, and discuss the use of this effect in solar cell optimization. To be consistent with the convention used in the UU group, we use the term external collection efficiency (ECE) instead of the more ambiguous term QE [10]. Because of the unnaturally high values of the ECE for cells discussed in this chapter, we introduce the term "apparent collection efficiency" (ACE) to describe these values.

6.2 Experimental details

The cells involved in this study have a n-i-p structure: substrate/ rough Ag/ ZnO back reflector/ n-type μc-Si:H/ intrinsic μc-Si:H/ buffer/ p-type μc-Si:H/ ITO/ Au (gridlines), with an active cell area of 0.13 cm^2. All silicon layers were deposited in the multi-chamber UHV PASTA system. Intrinsic i-layers were deposited by the Hot-Wire CVD technique near the phase transition region between microcrystalline silicon and amorphous silicon. Two 0.5 mm tantalum (Ta) filaments were used. The filament current was adjusted to be 10.5 A, with a calibrated filament temperature around 1850 ^oC, which results in a naturally heated substrate at a temperature around 250 ^oC on a glass substrate, and 270 ^oC on a stainless steel substrate [11]. Doped layers (p-type and n-type) were

deposited by plasma CVD in separated chambers. The substrates used were either Ag/ZnO coated Asahi U-type TCO glass, or Ag deposited at high temperatures (for proper roughness) with a ZnO coating made in house by sputtering.

Structural characterization was done by Raman scattering spectroscopy on samples deposited on the same type of substrates and appropriate stacks of under-layers (Asahi/Ag/ZnO/profiled n-layer). A spectral response setup with the possibility to apply bias light and bias voltage was used for measuring the external collection efficiency (ECE) of the solar cells. A Xenon lamp was used as the source both for the monochromator and for the bias beam. A short-pass filter KG1 was used in the bias beam to filter out the extra infrared light. To obtain blue and red bias light, a short pass filter BG23 and a long pass filter RG570 were used, respectively. The photon flux of the light, as measured by a calibrated silicon photodiode, was around 5×10^{15} $cm^{-2}s^{-1}$ for the bias beams and $3\times10^{13}cm^{-2}s^{-1}$, for the monochromatic beam. The intensity of the unfiltered white bias light (with the KG1 filter) was around 100 mW/cm^2 and was kept constant. Bias light intensity variations were realized by using a set of neutral density filters in the beam path. Current Density - Voltage (*J-V*) characteristics were measured with a dual-beam solar simulator (WACOM) at 25 ºC. To avoid the misinterpretation due to differences between the J_{sc} from *J-V* measurement and the integrated J_{sc} from ECE measurement, the former J_{sc} values was corrected to the integrated J_{sc} using the ECE plot obtained under the standard white light measurement and the tabulated AM1.5 spectrum[3] [12].

6.3 Experimental result

6.3.1 Observation of enhanced External Collection Efficiency (ECE)

Typical ECE curves of a cell exhibiting enhancements when using coloured bias light are shown in Fig. 6.1. Curves marked with squares and down triangles are the measurements performed under the standard conditions, i.e. in the dark and under white bias light respectively, and with 0V bias voltage. Integrated current density with respect to tabulated AM1.5 solar spectrum gives a value for the short circuit current density J_{sc} of 19.24 mA/cm^2, which is among the typical J_{sc} (ECE) for an around 1 μm thick n-i-p μc-Si:H cell on a Asahi/Ag/ZnO substrate. Under the blue bias light condition (Fig. 6.1, circles), an enormously enhanced ECE in the long wavelength region of the spectrum (wavelength from 550 nm to 1000 nm and above) with a peak value ~1.61 at around 700

[3] This correction is only used for the data shown in this chapter. For the difference between integrated short circuit current density from ECE measurement and the J_{sc} from AM1.5 J-V measurement, please refer to chapter 2.

nm wavelength is observed. Simultaneously, the curve in the short wavelength region (wavelength <550 nm) shows a lower ECE value than that obtained under the white bias light. The integrated current density amounts to a value of 32.7 mA/cm^2, which is 70% higher than that measured under the white light. With the red bias light (Fig. 6.1, up triangles), an enhanced blue response and slightly decreased red response are observed. The current-voltage measurement with the solar simulator (Fig. 6.2, dotted line) gives the following solar cell parameters: J_{sc} 19.24 mA/cm^2, V_{oc} 0.47V, *FF* 0.531 and *Eff.* 4.80%, indicative an inefficient collection of photogenerated carriers.

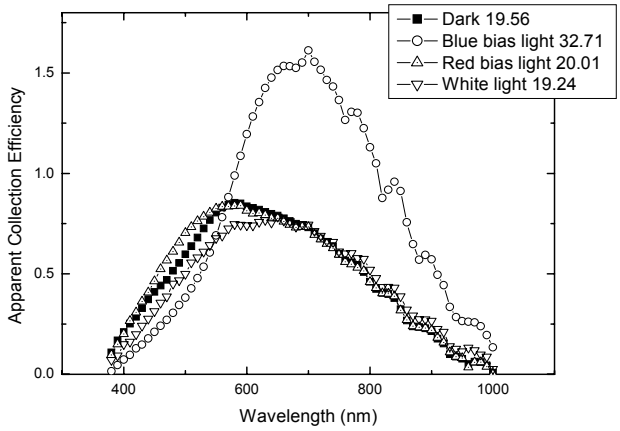

Fig. 6.1: ACE of a cell showing strongly enhanced values when using coloured bias light during the measurements. Solid squares: the cell is measured in the dark (Dark); open circles: measured with blue bias light; up triangles: with red bias light; down triangles: with white bias light (white light). The numbers in the legend show the integrated current density under AM1.5 illumination. The current density values shown in the legend are in mA/cm^2.

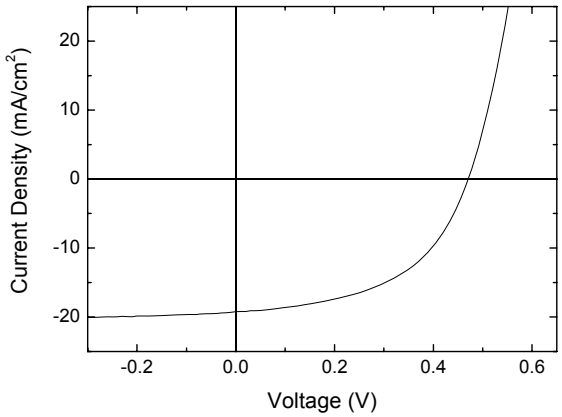

Fig. 6.2 Current Density-Voltage characteristics of a µc-Si:H n-i-p cell made on an Asahi/Ag/ZnO substrate. The ACE curves for this cell are shown in **Fig. 6.1**. Current density values were corrected using the integrated short circuit current density value (J_{sc}^{SR}) from the spectral response measurement (under white bias light) and the tabulated AM1.5 solar spectrum.

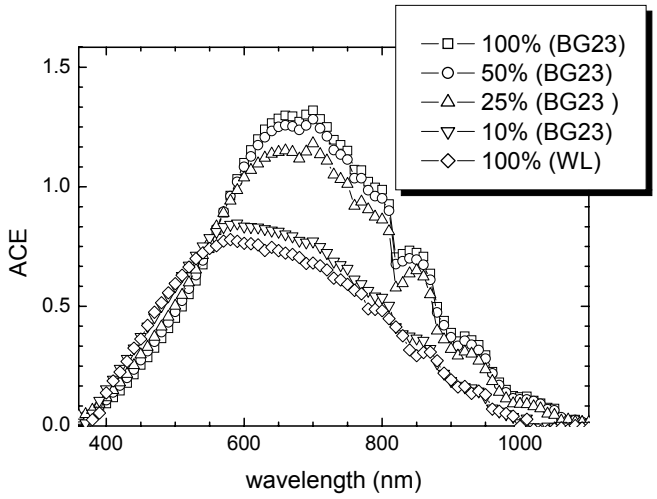

Fig. 6.3 Bias light dependence. (nn %): transmittances of neutral density filters; BG23: type of the blue filter used in the bias beam; WL: white light, no colour filter was used.

6.3.2 Light intensity dependence of the external collection efficiency

The observation of the strongly enhanced ECE values hints that besides the current generated by the monochromatic probe light, there must be some extra current that is also collected by the lock-in amplifier. Without active electronic-optical

conversion effect, the external collection efficiency shall not be greater than unity as this is against the energy conservation law. The fact that the ECE plots measured under the standard conditions show normal values suggests that the extra current in the red region of the spectrum may be related to the blue bias light used. To test this hypothesis, various neutral density filters were put into the bias light path in combination with the blue filter BG23. These ECE results are shown in Fig. 6.3. Clearly, the height of the ECE peak value decreases with decreasing applied bias light intensity, indicating that the enhanced response is indeed related to the blue bias light used.

To study the physical origin behinds this phenomenon, we employ the computer device simulation.

6.4 D-AMPS Analysis

The computer code D-AMPS was used to study this effect. D-AMPS stands for analysis of microelectronic and photonic devices (AMPS) core plus new developments. The computer code AMPS was developed at the Pennsylvania State University [13]. The new developments refer to new physics that were recently incorporated into AMPS by Dr. F.A. Rubinelli at INTEC, Universidad Nacional del Litoral, Argentina [9]. Using this program, we need to keep in mind that both substrate (n-i-p) and superstrate (p-i-n) solar cells are defined as p-i-n cells, since light are impinging from the p-side in both cases.

6.4.1 Principle of ECE measurement

Before we further discuss the strongly enhanced ECE in more detail, it is worth describing briefly the ECE measurement in the presence of bias light. In such experiments, a weak chopped monochromatic probe beam (wavelength λ) of photon flux $\phi_{ML}(\lambda)$ is incident on the sample in conjunction with a much stronger DC bias light (BL) of photon flux ϕ_{BL}. The external collection efficiency (ECE) is then obtained by synchronously detecting the AC component $\Delta J(\lambda)$ of the resulting photocurrent density with a lock-in amplifier. Thus,

$$ECE = \Delta J(\lambda)/e\phi_{ML} \qquad (6.1)$$

where e is the electron charge. The assumption implicitly contained in this measurement is that all the photocarriers in $\Delta J(\lambda)$ are from the probe light. As we discussed in the previous section, this assumption must not be valid in our case, otherwise the ECE value could not be greater than unity.

6.4.2 Input parameters for D-AMPS

A n-i-p cell with the structure Ag/ZnO/n type μc-Si:H/ intrinsic μc-Si:H/ p type μc-Si:H/ITO was used throughout this simulation work. The input parameters used were based on previous research done by J. Strengers et al on μc-Si:H n-i-p cells [14]. Important parameter values, such as effective band gap, defect density distribution, carrier mobilities of the intrinsic μc-Si:H materials were adjusted in a certain range, in order to produce fits to the experimental results. Three amphoteric-like Gaussians, D^+, D^0, D^-, were used to simulate the density of midgap states in the μc-Si:H layers (One Gaussian with amphoteric states equals the sum of one donor Gaussian and one acceptor Gaussian). The correlation energy U was assumed to be 0.2eV. The areas, widths, and heights of the Gaussians are shown in Table 1. DB Values for the doped layers are based on experimental results and on typical values from the literature. Note that the DB density parameters used by Jaap were on the low range of those shown in this table (~10^{14} cm^{-3}) [14]. Table 2 shows the other essential parameters. The back and front contacts: Ag, ITO and ZnO were treated only optically, but the band offsets between p/ITO interfaces and ZnO/n interfaces were taken into account in the treatment of the electrical transport. The optical properties of these two layers, n (λ) and k (λ), are obtained from the reflection and transmission spectra obtained on materials deposited on polished crystalline silicon wafers.

Table 6-1 Amphoteric-like Gaussians used to describe the defect density distribution in the intrinsic μc-Si:H layer.

Amphoteric-like Gaussians	*Density of states (cm^{-3})*	*Peak pos. of donor Gaussian from Ev (eV)*	*width(eV)*
D^+	10^{14}~10^{16}	0.3	0.1
D^0	10^{14}~10^{16}	0.6	0.1
D^-	10^{14}~10^{16}	0.9	0.1

Table 6-2 AMPS input parameters for the Si layers for a μc-Si:H p-i-n structure.

Input parameter	*p*	*i*	*n*
Thickness (nm)	20	0.1 to 10 μm	27
Effective band gap (mobility gap/optical gap) (eV)	1.4/1.2	1.25/1.2	1.4/1.2
Effective density of states N_c, N_v (cm^{-3})	3×10^{19}	3×10^{19}	3×10^{19}
Electron/hole mobility (cm^2/Vs)	40/4	50/5	40/4
Carrier capture cross section ($\sigma_{CH/NE}$) (cm^2)	$5x10^{-14}$/ $5x10^{-15}$	$(5\sim50)x10^{-15}$/ $(5\sim50)x10^{-16}$	$5x10^{-14}$/ $5x10^{-15}$
Tail Characteristic energy ED-EA (meV)	0.01	0.01	0.01

6.4.3 Simulation results: sensitivity study

Simulations were first performed for a cell illuminated only by blue bias light. Mid gap defect states in the intrinsic layer were assumed to be homogenously distributed along the thickness direction. The i-layer thickness was kept at 1300 nm, the value measured with a thickness profiler on the studied sample. Properties of the doped layers and front and top contact were assumed constant. The effective band gap, the defect density distribution, and the electron and hole mobility of the i-layer were varied, aiming at obtaining an enhanced ACE.

It was found that the carrier mobilities and the midgap defect density are the most sensitive parameters leading to enhanced ACE values. Fig. 6.4 shows the simulated ACE curve at different values of hole mobility (μ_p) and electron mobility (μ_n). It can be seen that a change in μ_p (a) and μ_n (b) can greatly influence the magnitude of the simulated curve. For a given defect density value (10^{16} cm^{-3}), the ECE value significantly increases when decreasing μ_p; while it decreases when decreasing μ_n.

In Fig. 6.5, the ACE peak values, at around 620 nm wavelength, are plotted against μ_n (a) and μ_p (b) mobilities, while keeping their counterpart (μ_p and μ_n, respectively) unchanged. The defect density was varied between 10^{15} and 10^{16} cm^{-3} with a homogeneous distribution profile as it is indicated in the legend of Fig. 6.5. Besides this difference, for a given mobility range a minimum defect density value is found to exist. This means below this limit, the carrier mobility has to be adjusted to a value that is physically unacceptable in order to observe an enhanced ACE. From Fig. 6.5, for the currently discussed device configuration and the input parameters under the homogeneous defect distribution assumption described above, and the intensity of blue bias light used (set as the same as the experimental light intensity), the minimum defect density value for observing enhanced ACE is between 10^{15} and 10^{16} cm^{-3}.

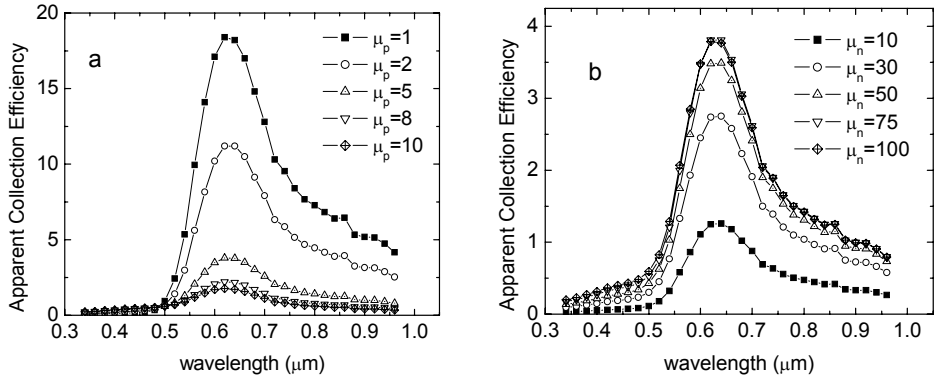

Fig. 6.4 Simulated ACE spectra for the n-i-p cell with a homogeneous defect density profile along i-layer thickness (~10^{16} cm^{-3}). (a) μ_n is fixed at 100 cm^2/Vs, hole mobility (μ_p) is given as 1, 2, 5, 8, and 10 cm^2/Vs; (b) μ_p is fixed at 5 cm^2/Vs and μ_n is varied as 10, 30, 50, 75 and 100 cm^2/Vs.

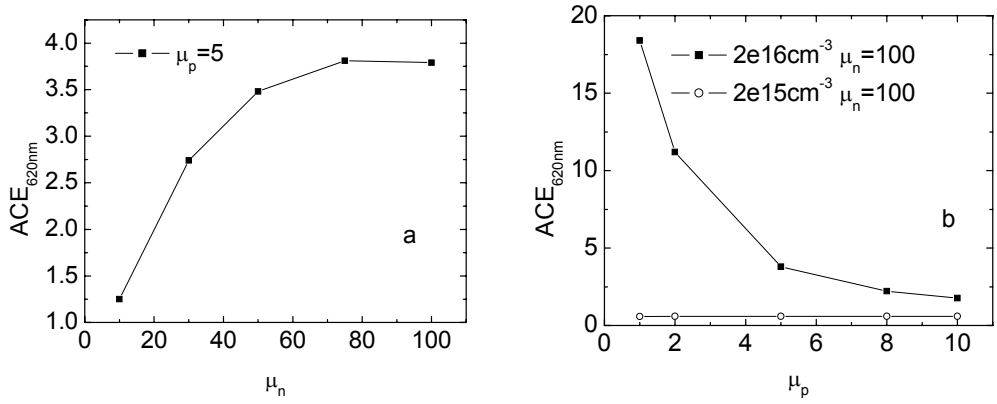

Fig. 6.5 Dependence of the apparent collection efficiency at 620 nm wavelength on the hole mobility μ_p (a) and electron mobility μ_n (b). The values of their counterpart (μ_p and μ_n, respectively) are kept unchanged and shown in the legend area.

6.4.4 Analysis: electrical field distribution

Due to the existence of electrical defects, the internal electric field in the intrinsic layer of a p-i-n cell is not homogenously distributed. This can be seen in Fig. 6.6a, the simulated internal electrical field profile under the short circuit condition. In the equilibrium state (solid line), a strong electric field exists in the region close to the p/i and i/n interfaces. In the middle part of the i-layer, however, the field is weakened by several orders of magnitudes. When the cell is illuminated, considerable amount of photogenerated carriers will be trapped by the shallow defects in the i-layer; the inhomogeneous spatial distribution of these trapped charges will modify the electrical

field distribution in the cell. This can be seen in Fig. 6.6b from the dashed curve in the space charge distribution plots when the sample is measured under the white bias light. As a result, the shape of the field distribution profile (Fig. 6.6a, dashed line) changes slightly compared to the curve under the dark conditions, and the minimum shifts to the rear side of the cell.

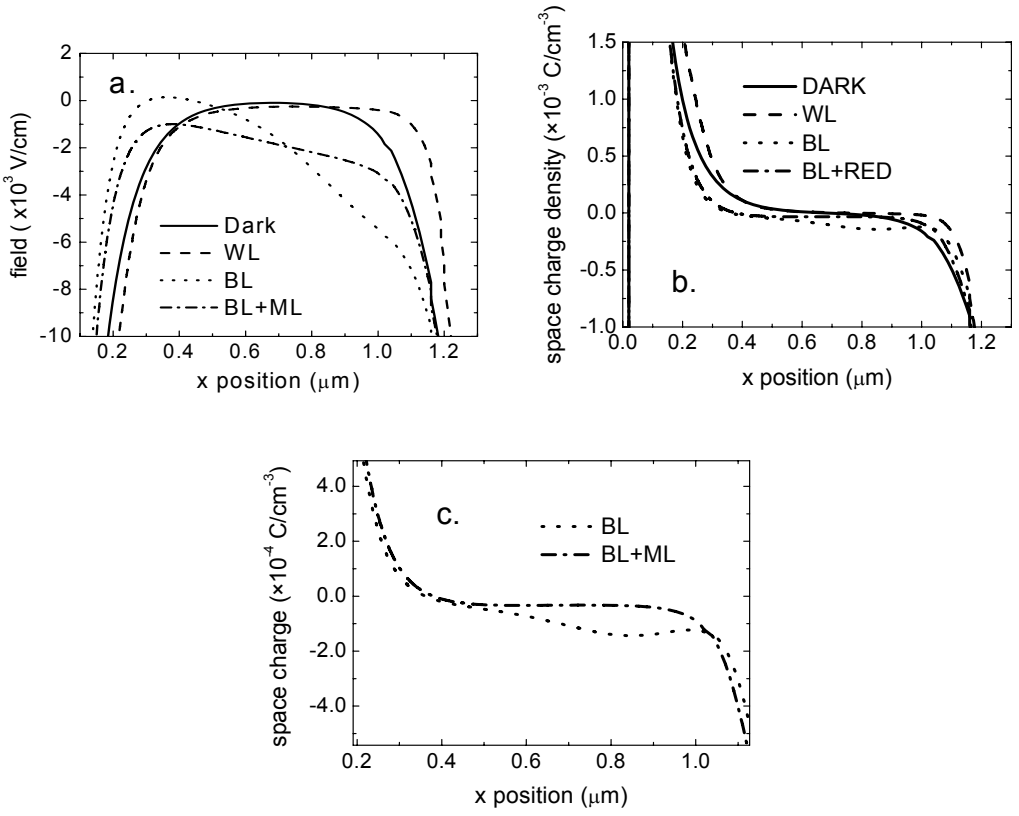

Fig. 6.6 The electric field (a) and space charge (b and c) distribution in the short circuit condition for i-layer only. WL: AM1.5 bias light; BL: blue bias light; ML: red monochromatic light. c) is the enlarged version of figure (b) with only BL and ML light impinging on the cell.

When the cell is illuminated with a strong blue bias light (AM1.5 spectrum with a blue filter, photon flux in the order of 1×10^{15} cm^{-2}), almost all the incident photons are absorbed in the front part of the cell, due to the high absorption coefficient of the intrinsic μc-Si:H to short wavelength light. As a result, a much weakened electric field is presented in the front part of the i-layer, with a minimum close to zero; the field in the rear side of the cell is, however, increased compared to the dark and white light condition (Fig. 6.6b, dotted line). This is a result of the fixed boundary condition acting on the

electric potential, i.e. the integral of the electric field over the whole device must be equal to the external applied bias that in these experiments is set equal to zero.

When a chopped monochromatic red probe beam (ML) with a photon flux in the order of 1×10^{13} cm^{-2} is superposed on the strong blue bias beam (BL), the photons are nearly homogenously absorbed in the i-layer due to the low absorption coefficient of the μc-Si:H for the red light. This can again modify the space charge distribution profile, but it will have the largest influence in the rear part of the i-layer. In the front part, the space charge density is dominated by the blue bias light, which is about 2 orders of magnitude stronger than the monochromatic probe beam. This can be seen in Fig. 6.6c, an enlarged space charge distribution profile where only the 3rd (BL) and 4th condition (BL+ML) of Fig. 6.6b are plotted. This modulated space charge distribution results in a modulated field distribution profile which is in phase with the incident monochromatic probe beam, as is shown in Fig. 6.6a by the dashed dotted line. It can be seen that the previously weakened electric field in the front part of the i-layer by the DC blue bias light is now enhanced, although the magnitude is not large. Due to the overwhelming absorption of the strong bias light, the small change in the electric field has a strong influence on the carrier transport kinetics. As a result, a decrease of recombination rate in the front part of the cell is observed (Fig. 6.7), which is in phase with the modulated monochromatic light; simultaneously, some photocarriers generated by the DC bias light drift to the front contact (Blue bias light) and are collected by the lock-in amplifier.

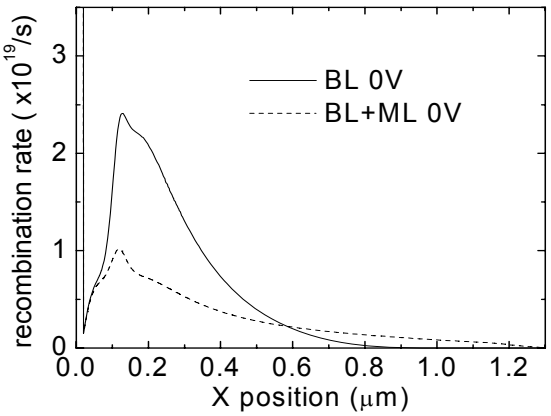

Fig. 6.7 Recombination rate profile when only the blue bias beam (BL, solid line) and both BL and a weak red probe beam (BL+ML, dashed line) are presented. Photon flux: $\phi_{BL}=1\times10^{15}$ cm^{-2} and $\phi_{mL}=1\times10^{13}$ cm^{-2}.

The mechanism of the enhanced ECE values is similar to the photogating effect observed in an amorphous silicon p-i-n structure and a Schottky barrier structure. The difference in the present case from the previous observations is that the input parameters in our simulations were chosen to fit μc-Si:H solar cells. This is mostly represented by

the higher carrier mobilities and the narrower mobility band gap, compared to those of the amorphous silicon material. Structural characterization done by Raman and XRD spectroscopy indeed shows the microcrystalline nature of the studied cells and material.

6.4.5 Light intensity dependence

Since the photogating (PG) effect is related to the bias light, the stronger the bias light is, the weaker the field minimum shall be, therefore, the more carriers will be gated out by the probe beam. This was indeed observed in our experiment. From Fig. 6.3, the experimentally observed dependence of ACE on the bias light intensity, an increase of bias light intensity indeed lead to an increase of the ACE peak height.

Simulations also show that, with a decrease in the monochromatic beam intensity, the PG effect is enhanced, as shown in Fig. 6.8a. Experiments are therefore performed with 3 different probe beam intensities by adjusting the opening area of an extra diaphragm in the probe beam path. The results are shown in Fig. 6.8b. It can be seen that the ACE peak indeed increases when decreasing the monochromatic beam intensity.

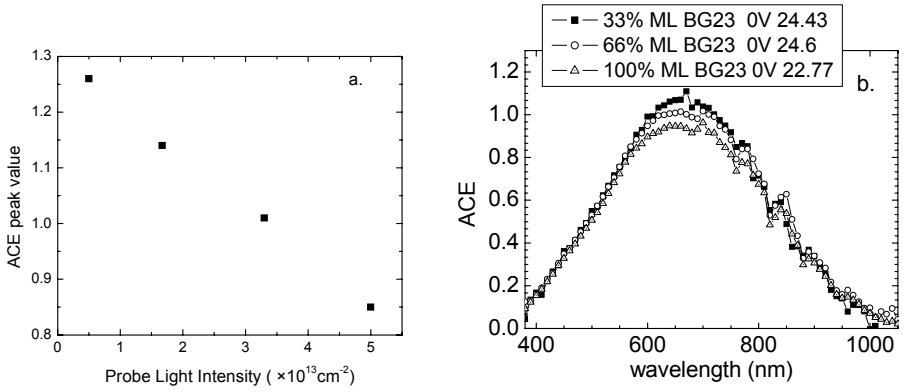

Fig. 6.8 Monochromatic light intensity dependence. (a) simulated result (b) experimental result.

The weakening of the PG effect with increasing the monochromatic light intensity can be explained as following. With the presence of both a DC bias light (BL) and an AC monochromatic light (ML), the internal field profile is always modified by the sum of I_{BL} + I_{ML} (I denote the intensity of the light). Assuming the average intensity of the monochromatic light is I_{ML0}, the DC component of the internal field is then determined by I_{BL} + I_{ML0}. Due to the opposite influence of this two coloured beams on the field distribution, the higher the red ML intensity is, the stronger the field minimum will be (in the case of $I_{BL} > I_{ML}$), as it is shown in Fig. 6.6a by the dotted dashed line, and the less

carriers will be gated out. Therefore, a reducing in the ACE peak with increasing the ML intensity is observed.

6.4.6 Thickness dependence

Based on the principle of the PG effect described above, we know that for a given defect density, the magnitude of the PG effect depends on the internal field distribution. Therefore, for cells made with the same material, variations of the i-layer thickness, which will likely result in a change in the internal field distribution, may influence the magnitude of the ACE (enhanced ECE) values. Simulations were therefore performed for cells with different i-layer thickness. With the defect density, μ_n, μ_p and other parameters kept unchanged, the i-layer thickness were varied from 500 nm to 5000 nm. The results are shown in Fig. 6.9a where the peak values of the ACE curves are plotted along the y-axis and the i-layer thicknesses in nm along the x-axis. It can be seen, for the given material parameters, that there is an optimal thickness for observing the PG effect. Detailed simulation study points out that for a cell with a very thin i-layer (thickness far below the optimum), a strong internal field is formed in the i-layer accompanied with a largely reduced carrier recombination and a strong drift current in the i-layer. A small modulation on the field strength due to the presence of a monochromatic light is not able to introduce a significant change in the output current. As a result, a decrease in the ACE peak height is observed. On the other hand, when the i-layer is too thick (much thicker than the optimum thickness), the released photocarriers due to a weakening of electrical field caused by the modulated monochromatic light mostly recombined at the deep state before reaching to the contacts. This also results in a decrease in the output current, therefore ACE peak height.

This is then tested in the μc-Si:H cells with identical p and n layers but with the i-layer thickness varies from 700 nm to 1300 nm. The results are shown in Fig. 6.9b. It is observed that within the thickness range studied here, the PG peak values indeed increase with the i-layer thickness.

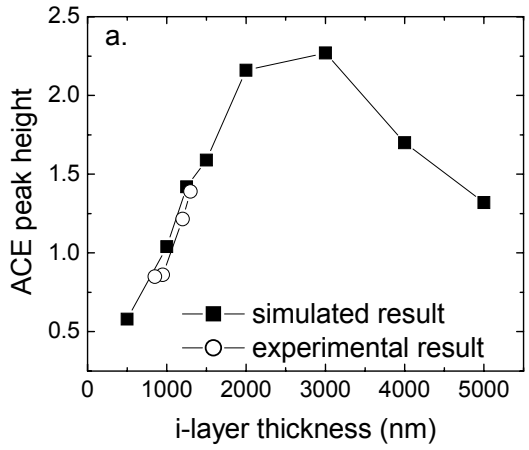

Fig. 6.9 Thickness dependence. Squares: Simulated result; circles: experimental result.

6.5 Discussion

The consistency of AMPS simulation with the experimental results indicates the large similarity of the unusually enhanced ACE of μc-Si:H solar cells with the photogating (PG) effect previously observed in an a-Si:H p-i-n structure [2]. We therefore propose to extend the name to describe the observed effect in the μc-Si:H cells.

D-AMPS analyses points out that a lowered electrical field and the existence of a high density of trapping state in the intrinsic layer are the key factors for observing a strong PG effect. In a μc-Si:H cell with good i-layer quality, the PG effect shall not be significant, due to the much lower electrical defect in such layers. However, our experiments show that this is not always the case. The ECE measurements on single junction μc-Si:H n-i-p cells with coloured bias light showed that a strong PG effect can be often observed on cells with a un-optimized buffer/p/ITO region. As we argued in Chapter 5, it is very likely that the internal field in such cells collapses due to the carrier transport barrier in this region; a post deposition annealing treatment can largely remove this barrier, and therefore results in a re-enhancement of the electrical field. The ACE curves obtained on those cells before and after the annealing treatment indeed show a dramatic difference in the significance of the PG effect. One such example is depicted in Fig. 6.10, where ACE of a sample previously showed a similar behaviour as that presented in Fig. 6.1 before annealing are plotted. Clearly, compared to the ACE measured before the annealing treatment, the strong enhancement in the long wavelength region under the blue bias light (as in Fig. 6.1, with a ACE peak as high as 1.61) has been largely reduced (shown in Fig. 6.10, with a ACE peak of ~ 0.87), and its J_{sc}^{SR} (21.13

mA/cm^2) is only slightly larger than that measured under the white bias light (20.67 mA/cm^2). These figures strongly support the validity of our explanation on the internal field enhancing effect of the post-annealing treatment (chapter 5) on such cells.

One important detail of the sample shown in Fig. 6.10 is that the i-layer in this cell was deposited at a constant R_H of 0.952. Raman and XTEM analyses on cells made on the same type of substrate and at the identical deposition conditions did not show crystallinity evolution in its i-layer [15]. Fourier Transform Photocurrent Spectroscopy (FTPS) analyses on this sample give an upper-limit value for the i-layer defect density of 3×10^{15} cm^{-3}. AM1.5 *J-V* measurement after the post deposition annealing treatment shows an efficiency of 8.41%, with the J_{sc}, V_{oc} and *FF* of 23.6 mA/cm^2, 0.543 V and 0.656, respectively. This measurement was performed with the ITO mask on the X-Y table and without J_{sc}^{IV} to J_{sc}^{SR} correction. It is the highest efficiency obtained for μc-Si:H n-i-p cells with a hot-wire i-layer made with a constant R_H setting.[4]

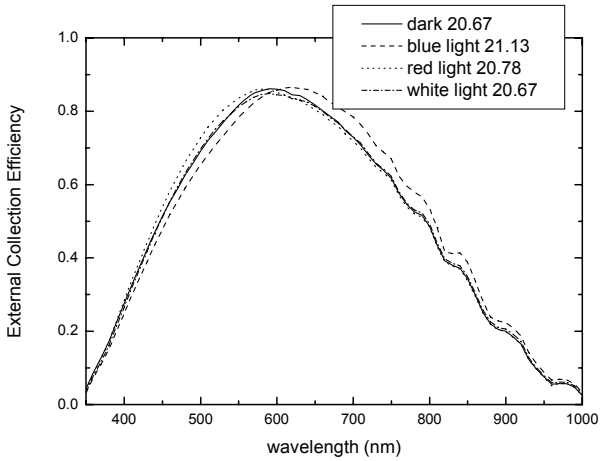

Fig. 6.10 ACE of a cell after the post-deposition annealing treatment. The ACE curves measured before the treatment are similar to that shown in Fig. 6.1.

[4] A μc-Si:H n-i-p cell made on textured stainless steel foil with a 2 μm i-layer deposited with a two-step reverse H_2 profiling technique showed a efficiency of 8.5% (see chapter 4).

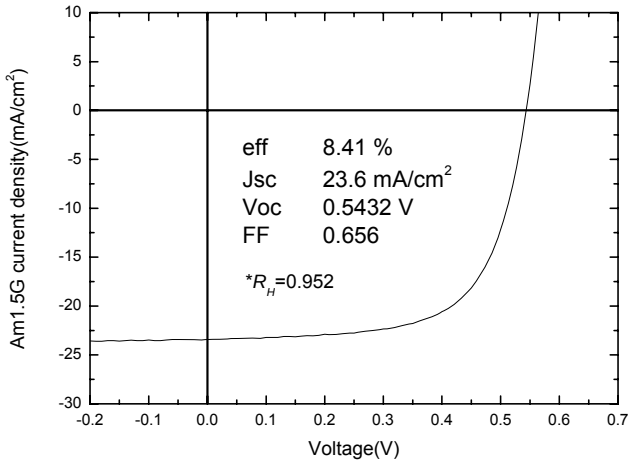

Fig. 6.11 AM1.5 *J-V* characteristics of a µc-Si:H n-i-p cell made on an Asahi/Ag/ZnO substrate. The measurement was done with the ITO mask. The ACE of this cell are shown in Fig. 6.10.

Further, the observation of PG effect in µc-Si:H solar cells with a HWCVD i-layer made near the phase transition regime proves that carrier transport in such a cell is to a large extend determined by the internal electrical field in the i-layer. This is a direct evidence for the importance of drift current in such devices. The study on this effect can be further extended to µc-Si:H cells with an i-layer made with other deposition techniques such as VHF PECVD or MWCVD in order to extend the knowledge on the transport mechanism of this multi-phase material. One important feature of the PG effect is that both field modulation and the carrier transport are in the vertical direction to the substrate surface. This makes it unique compared to other characterization techniques.

6.6 Conclusion

Observation of enormously enhanced external collection efficiency (ECE) under a blue bias light was for the first time reported on µc-Si:H single junction solar cells (with HWCVD i-layer). Thickness and light intensity dependence of this effect are consistent with the computer simulated results, and are similar to the photogating effect that was previously observed in an amorphous p-i-n structure. We therefore propose to extend the name "photogating" to describe the observed effect in the µc-Si:H cells.

The existence of this effect further proves that carrier transport in a µc-Si:H solar cell with a hot-wire i-layer made near the phase transition regime is to a large extent determined by the internal electrical field. To have an maximum energy output from µc-Si:H solar cells, carefully control on the quality of each doped layer and their interfaces

in order to have an optimized internal field in the i-layer are of equally importance as that of improving the electrical quality of the intrinsic μc-Si:H layer.

References

1. A simplified version of this chapter was published in 21st European PVSC conference, Dresden, Germany, 4-9 September 2006, paper 3DV3.51.
2. J. Y. Hou and S. J. Fonash, Appl. Phys. Lett. 61 (1992) 186.
3. H. P. Maruska, M. C. Hicks, T. D. Moustakas, and R. Friedman, IEEE T. Electron. Dev. ED-31 (1984) 1343.
4. F. A. Rubinelli, J. Appl. Phys. 75 (1994) 998.
5. S. Bae, S. J. Fonash, J. Appl. Phys. 79 (1996) 2213.
6. M. Gloeckler and J. R. Sites, J. Appl. Phys. 95 (2002) 4438.
7. G. Agostinelli, D. Batzner, M. Burgelman, Proc. 29th IEEE PVSC conf. (2002) 744.
8. S. Hegedus, D. Ryan, K. Dobson, etc. Mat. Res. Soc. Symp. Proc. 763 (2003) B9.5.1.
9. F.A. Rubinelli, J.K. Rath, and R.E.I. Schropp, J. Appl. Phys. 89 (2001) 4010.
10. A more detailed discussion on the terms SR, EQE, ECE is given in section 2.3.2 of this thesis.
11. M. K. van Veen, R.E.I. Schropp, J, Appl. Phys. 93 (2003) 121.
12. 'AM1.5 Global' spectrum is taken from table 2c, column 1 and 6 from the article 'Spectral solar irradiance data sets for selected terrestrial conditions' by R. Hulstrom, R. Bird and C. Riordan, Solar Cells 15 (1985) 365.
13. P. Chatterjie, P. J. McElheny, and S. J. Fonash, J. Appl. Phys. 67 (1990) 3803.
14. J.J.H. Strengers, F.A. Rubinelli, J.K. Rath, R.E.I. Schropp, Thin Solid Films 501 (2006) 291.
15. For the Raman and XTEM pictures for cells made at this condition, please refer to those shown in Chapter 3.

7

Multijunction n-i-p thin film solar cell made on stainless steel foil with hot-wire CVD deposited silicon absorber layers

Combining all the knowledge that we have gained during the development of single junction solar cells, tandem and triple junction n-i-p cells were developed at the Utrecht University. This chapter summarizes our effort to improve the quality of tunnel-recombination junctions (TRJ) between the adjacent subcells (Section 7.1), the effect of current matching on the *FF* of a tandem cell (Section 7.2) and present the result of optimization on n-i-p triple junction solar cells (Section 7.3). In the end of this chapter, room for further increasing the triple cell efficiency is discussed.

7.1 Improvement of the tunnel-recombination junction in n-i-p micromorph tandem silicon solar cells [1]

Hot-wire chemical vapour deposition (CVD) is suitable for the preparation of thin film silicon layers of high optoelectronic quality. At Utrecht University this technique has been applied previously for depositing the intrinsic layers of n-i-p configured single-

and multi-junction solar cells on plain stainless steel. Despite their relatively good cell parameters under AM1.5 illumination, the spectral response without bias illumination ('dark SR') of the tandem cells was not in agreement with expectation. This was due to dark current conduction through the bottom cell. This section shows how in the case of micromorph tandems the insertion of a 5 nm n-doped amorphous layer between the μc-Si:H n- and p-layer of the TRJ, together with a reduction of the n-layer thickness, leads to a correct dark SR. In addition, the V_{oc} and *FF* of the cells improve, the values of the best cell being 1.40 V and 0.74, respectively. In those cases where the dark SR behaved anomalously, we believe that a dark current conduction path is formed, because the bottom cell is damaged by the deposition conditions of the top cell n-layer. A thinner n-layer means a shorter exposure time and, therefore, less damage. The n-a-Si:H interlayer can serve as a protective layer that reduces or prevents damage to the bottom cell, possibly by being a barrier against hydrogen diffusion.

7.1.1 Introduction

Hot-wire CVD (HWCVD) is suitable for the preparation of device quality intrinsic [2, 3, 4] and doped [5,6] materials. At Utrecht University, single junction n-i-p cells with PECVD (13.56 MHz) doped layers and HWCVD intrinsic a-Si:H [2], μc-Si:H [7] or poly-Si [8] as well as tandems and triple cells with combinations of these materials, have been made. For single junction cells without enhanced back reflector, until recently (2004) the highest efficiencies obtained were 7.2% [2], 4.8% [7] and 4.4% [8] for cells containing intrinsic a-Si, μc-Si:H and poly-Si layers, respectively. In the case of tandem cells, the highest efficiencies are 8.5% for a-Si:H/a-Si:H [9], 7.0% for a-Si:H/μc- Si [5] and 8.1% for a-Si:H/poly-Si [10] cells. The best triple cell, with intrinsic a-Si:H in the top cell and μc-Si:H in the middle and bottom cells, had an efficiency of 9.1% [5]. All cells were deposited on plain stainless steel, so they were not equipped with an enhanced (textured) back reflector.

So far, the spectral response measured without bias light (which will be referred to as "dark SR") of our n-i-p tandem cells was usually showing the response of the top cell, indicating that the cells under these specific monochromatic measurement conditions are top cell limited. For a properly working tandem cell, the dark SR should equal the lowest of the two sub cell responses at each wavelength. Previous investigations [5] have shown that the behaviour of the cells in the dark and under light-biased SR measurements is related to the thickness of the n-layer in the tunnel-recombination junction (TRJ). Thinner n-layers lead to SR results that are more in agreement with expectation. Therefore, the reason for the unexpected dark SR results is likely related to the conditions of the n-layer deposition.

In this section, investigations to improve our tandem cells are presented. Micromorph cells with HWCVD intrinsic layers having different TRJ-configurations were examined. All TRJ's were composed of a μc-Si:H p-layer and a double n-layer, consisting of a μc-Si:H n-layer and a thin n-doped a-Si:H layer. Cells with various n-layer structures were characterized by means of IV- and SR measurements. The reason for having used a micromorph cell instead of an a-Si:H/a-Si:H cell for optimization is that this cell structure is later used as the top and middle cell of our triple cells.

7.1.2 Experimental details

All cells studied in this section are micromorph n-i-p configured cells. Plain stainless steel is used as a substrate material and back contact. No (textured) back reflector was used. All silicon layers of the cells were deposited in the PASTA system [11], a multi-chamber ultrahigh vacuum system with separate chambers for intrinsic, n-doped and p-doped layers. All deposition rates mentioned in this section were derived from reflection-transmission measurements of layers on glass, the thickness of a layer taken equal to the corresponding deposition rate multiplied by the deposition time.

The intrinsic layers were deposited by means of HWCVD. Two tantalum filaments were used with a filament current of 10.5 A for both intrinsic materials. Undiluted silane was used as a source gas for the a-Si:H deposition, at a gas flow rate of 90 sccm and a pressure of 20 μBar. At a substrate temperature of about 250 °C, this results in a deposition rate of about 10 Å/s [9]. The material has a Tauc gap of 1.8 eV. For all cells, the thickness of the a-Si:H i-layer was 200 nm.

The μc-Si:H was deposited with a hydrogen dilution of 0.95 at a pressure of 50 μBar, resulting in a deposition rate of about 2.1 Å/s [5] at a deposition temperature of 250 °C. This material, which is slightly away from the amorphous to microcrystalline transition, has a crystalline ratio of 40%. Sample 1 (see "Results" section), which was our best tandem cell on plain stainless steel, is used to mark the starting point for this experiments. The μc-Si:H i-layer of this cell was grown at a hydrogen dilution of 0.93. For all cells the μc-Si:H i-layer was 1.5 μm thick.

The doped layers of the cells were deposited by means of PECVD at a discharge frequency of 13.65 MHz. Both the a-Si:H and the μc-Si:H n-layer [12] were deposited at a substrate temperature of 200 °C, whereas the μc-Si:H p-layer [13] was deposited at 160 °C. The growth rates of the μc-Si:H n- and p-layers are 0.16 Å/s and 0.33 Å/s, respectively. Both p-layers in the tandem cells have a thickness of 26 nm; the bottom cell μc-Si:H n-layer is 77 nm thick. The thickness of this n-layer was previously optimized for n-i-p cells directly grown on plane stainless steel. In two of the deposited samples (see Table 7-1 in the "Results" section), the μc-Si:H n-layer was deposited at a higher

plasma power, which resulted in a higher growth rate of 0.23 Å/s. The a-Si:H n-layer in the TRJ was deposited at 0.71 Å/s.

At both i/p interfaces a 2.5 nm buffer layer of wide band gap intrinsic a-Si:H is incorporated to enhance the nucleation of the µc-Si:H p-layer [10]. After the deposition of the bottom cell p-layer, the cell is exposed to air to permit the formation of a defect-rich SiO_x interface layer at the p/n interface. This interface provides sufficient charge carrier recombination [14] and in addition, enhances the nucleation of the µc-Si:H n-layer. The solar cells are defined by 4 × 4 mm^2 reactively evaporated ITO pads with a thickness of about 80 nm, topped with a gold grid that sets the active cell area of the cells to 0.13 cm^2.

IV-measurements on the cells were performed by means of a WACOM dual source solar simulator. For the SR-measurements monochromatic light and bias light from a filtered Xenon lamp are used.

7.1.3 Results

Table 7-1 lists the n-layer structures that were used in the TRJ of the studied cells. In the following, the different types of TRJ's will be referred to with the corresponding sample no.

Table 7-1 Structure of the different double n-layers that were used in the TRJ of the studied cells

*These n-µc-Si:H layers were deposited at a higher plasma power

Sample no.	TRJ Structure
1	p/ SiOx/ 77 nm n-µc-Si
2	p/ SiOx/ 2.5 nm n-a-Si:H/ 31 nm n-µc-Si
3	p/ SiOx/ 5 nm n-a-Si:H/ 31 nm n-µc-Si
4	p/ SiOx/ 5 nm n-a-Si:H/ 33 nm n-µc-Si*
5	p/ SiOx/ 23 nm n-µc-Si/ 5 nm n-a-Si
6	p/ SiOx/ 5 nm n-a-Si:H/ SiOx/ 33 nm n-µc-Si*

Figs.1a-d show the top cell (red bias light), bottom cell (blue bias light) and dark SR for samples 1-4. For sample 1 it was necessary to apply a bias voltage (of 0.94 V) to measure the bottom cell response. For the samples 2-4 only the usual bias light was sufficient. In Fig. 7.1a it can be seen that the dark SR for sample 1 follows the top cell response, whereas it should at each wavelength equal the lowest subcell response. Upon a strong reduction of the n-layer thickness (77 nm down to 31 nm) and the insertion of a 2.5 nm a-Si:H interlayer between the µc-Si:H p and n-layer (sample 2), the dark response

lies closer to expectation. Increasing the thickness of the interlayer to 5 nm (sample 3) results in a dark SR that is, apart from some 'leakage', equal to the expected response (Fig. 7.1c). Decreasing the deposition time of the µc-Si:H n-layer by using a higher plasma power (sample 4) results in a dark SR that adequately equals the lowest subcell response at all wavelengths. Cell parameters for the best cell of samples 1-4, obtained from IV-measurements, are given in Table 7-2.

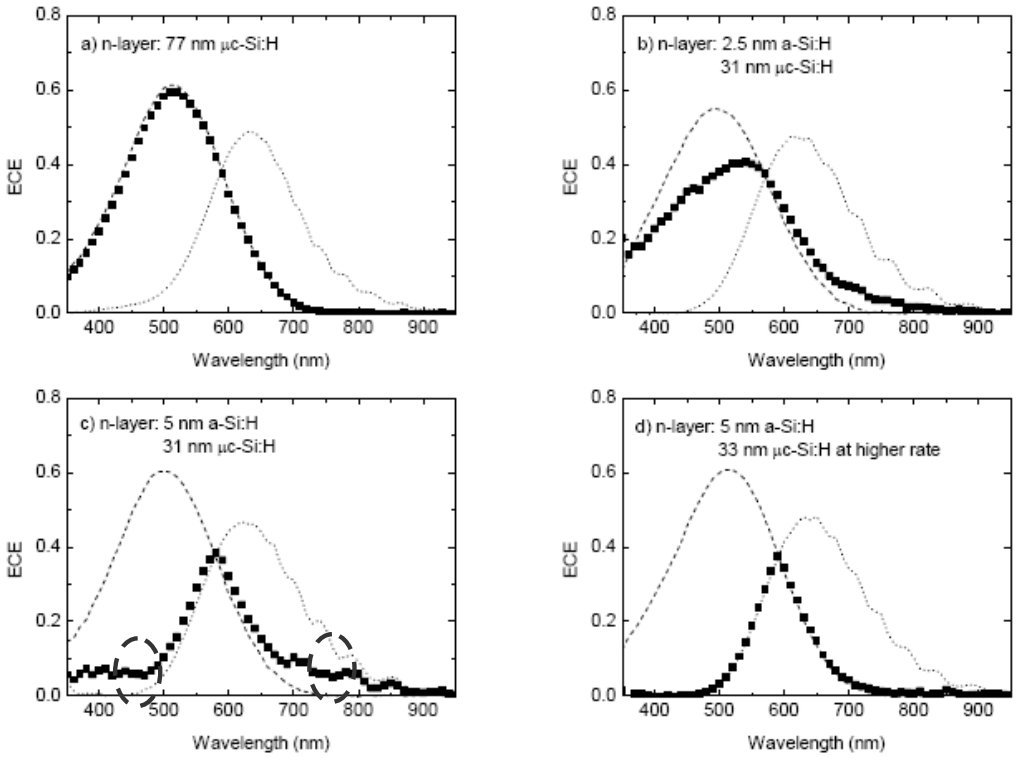

Fig. 7.1 a) – d): The ECE curves of dark (connected squares), top and bottom cell (solid lines) of samples 1-4, respectively. The regions marked by the dashed circles in fig. c) indicate what we call "leakage".

Table 7-2 Cell parameters of the best cells of samples 1-4 from Table 7-1.

No	V_{oc}(V)	*FF*	R_{sc}(kΩcm^2)
1	1.31	0.67	2.2
2	1.30	0.63	2.2
3	1.40	0.72	3.0
4	1.38	0.74	5.5

It can be seen that the V_{oc} and *FF* of the cells with a 5 nm a-Si:H interlayer have significantly improved with respect to the reference cell, whereas the *FF* of the cell with the 2.5 nm interlayer (sample 2) has greatly decreased.

7.1.4 Discussion

The observation that the dark SR of the cell with the conventional TRJ (sample 1) is limited by the top cell means that the top cell current can be matched at all monochromatic wavelengths by the bottom cell, also at those wavelengths where the bottom cell response is lower than that of the top cell. This looks like 'leakage' through the bottom cell. This 'leaking' current is also responsible for the fact that the bottom cell SR of the cell cannot be measured without the application of a bias voltage. In previous research a top cell limited dark SR was also observed for a-Si/a-Si:H [9] and a-Si:H/poly-Si tandems [10], showing that the presence of bottom cell leakage does not depend on the bottom cell i-layer material. In the case of a-Si:H/a-Si:H tandems, reduction of the n-layer thickness from 77 to 31 nm showed improvement: the top and bottom cell responses could be measured without the necessity to apply a bias voltage and the dark SR was closer to what it should be. The deviating behaviour of the measured dark SR was, however, not eliminated entirely. From the improvement it seems that a decrease of the n-layer thickness reduces the leakage through the bottom cell.

Generally, and also in the case of sample 1, the AM1.5 IV-parameters of the cells with a leakage path in the bottom cell are relatively good. From this it follows that a leakage path through the bottom cell does not necessarily lead to a bad cell operation under normal light conditions.

The origin of the leakage path is unclear. Possibly, it is formed, because the hydrogen-rich plasma used to deposit the n-layer induces damage to (part of) the bottom cell, e.g. the i/p interface or the i-layer. This would explain the influence of the n-layer thickness on the outcome of the previous SR measurements. A thicker n-layer means a longer exposure time of the bottom cell to the hostile deposition conditions, inducing more damage. At a certain point, a 'leakage' mode will be formed, which, once sufficiently large, will lead to deviations in the dark SR. For a thicker n-layer the deviation will increase, finally leading to a top cell limited dark SR. A longer exposure time will lead to a top cell limited dark SR and, finally, to a bottom cell response that can only be measured by combining the usual bias light with a bias voltage.

In this view, the amorphous interlayer can be regarded as a protection layer that reduces or prevents damage to the bottom cell. It may act as a barrier against hydrogen diffusion into the i-layer. From the dark SR of samples 2-4 (Fig. 7.1b-d) it can be seen that the interlayer needs to be thick enough to give protection: for a 5 nm layer the dark SR is close (sample 3) or equal (sample 4) to the expected response, whereas for a 2.5 nm layer the dark SR is in between the correct response and the top cell limited case (Fig. 7.1a). This intermediate dark SR shows that the 2.5 nm interlayer already reduces the

charge leakage through the bottom cell. The leakage that remains upon the insertion of a 5 nm interlayer (sample 3) disappears almost completely when the deposition time of the μc n-layer is reduced to 0.75 times its initial value (sample 4, which has about the same n-layer thickness as sample 3 in a shorter deposition time, because of the use of a higher plasma power). The reduction in charge leakage from cell 1 to 4 is reflected in the increase of R_{sc} from 2.2 to 5.5 kΩcm^2.

From Table 7-2 it follows that the sample with the 2.5 nm interlayer has nearly the same V_{oc} as the one without interlayer. When the interlayer is 5 nm, thick enough to result in a correct dark SR, V_{oc} increases to values as high as 1.40 V. The *FF* of the samples with a 5 nm interlayer is also significantly better than that of the sample without one.

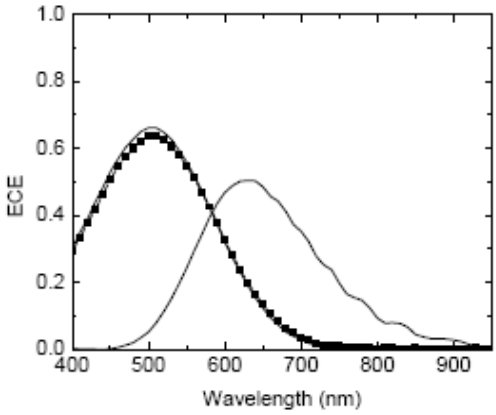

Fig. 7.2 Dark (connected squares), top and bottom cell (solid lines) SR of sample 5.

In literature the use of double and even triple n-layers (a-Si:H/μc-Si/a-Si) in the TRJ of both p-i-n and n-i-p multijunction cells has been reported to result in a high V_{oc} [15, 16, 17]. Pellaton Vaucher *et al.* [16] attributed the beneficial effect of an a-Si:H n-layer at the n/i-side of the TRJ in a-Si:H/a-Si:H p-i-n tandem cells on V_{oc} to a better energy band continuity at the i/n interface of the top cell. Because the μc-Si:H n-layer in samples 2-4 was grown on top of an a-Si:H layer without an air break, the top of the μc-Si:H layer may still be quite amorphous, which could explain the higher V_{oc}. To investigate this, we deposited samples 5 and 6, the TRJ's of which are listed in Table 7-1.

In sample 5, the 5 nm amorphous interlayer is deposited on top of a μc-μc TRJ with a μc-Si:H n-layer thickness of 23 nm. If an improved n/i interface causes the increase in V_{oc} of samples 3 and 4, the cells of this sample should have a high V_{oc}. From IV measurements, the best cell V_{oc} was found to be only 1.25 V, meaning that the improvement of V_{oc} does not dominantly result from a reduction of the band discontinuity at the n/i interface. The SR of a cell of sample 5 is given in Fig. 7.2. It can be seen that

the dark SR is top cell limited. This shows that even for a µc-Si:H n-layer thickness in the TRJ of 23 nm, which takes the same deposition time as the 33 nm high power n-layer of sample 4, direct deposition of the n-layer on top of the bottom cell results in the formation of the 'leakage' mode. The different from sample 1 was that the bottom cell response could be measured without the use of a bias voltage. In agreement with the mentioned previous work, this shows that the damage had decreased with the reduction of the n-layer thickness.

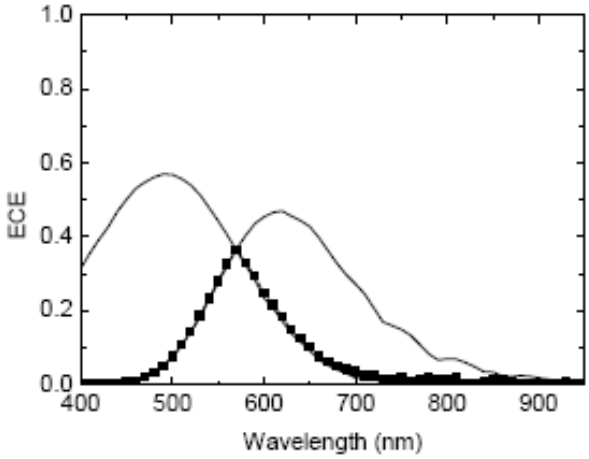

Fig. 7.3 Dark (connected squares), top and bottom cell (solid lines) SR of sample 6.

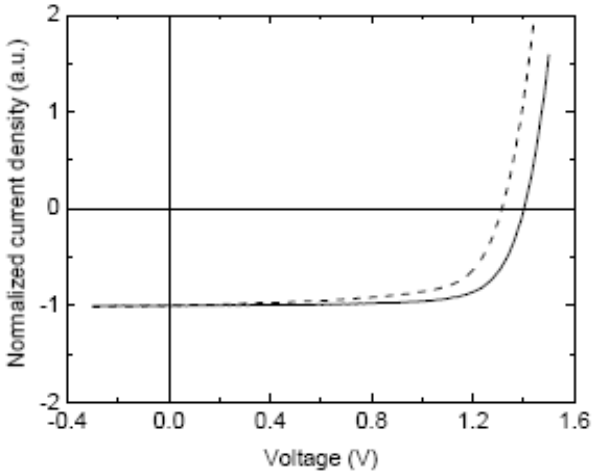

Fig. 7.4 Normalized light IV-curves of sample 1 (dashed line) and sample 6 (solid line).

During the preparation of sample 6, two air breaks were used during the deposition of the TRJ. Besides the conventional air break at the p/n interface for the generation of sufficient recombination centres, there is one after the deposition of the n-a-Si:H interlayer, meant to enhance the nucleation of the µc-Si:H n-layer. A similar double air

break has been used successfully in the TRJ of VHF plasma p-i-n a-Si:H/a-Si:H tandems fabricated in our group [13]. The dark SR of the cell, shown in Fig. 7.3, closely follows the lowest sub cell response, as was also observed for sample 4. The value of R_{sc} for this sample is even higher than that of sample 4: 12.1 kΩcm^2, which is in agreement with the almost zero leakage that follows from the dark SR. The best cell of sample 6 had a V_{oc} of 1.40 V and a *FF* of 0.74, making its TRJ the best of all TRJ's explored in this section. Fig. 7.4 shows the normalized IV-curves of samples 1 and 6. The improvement of the cell is obvious. The extra air break should lead to a higher crystallinity of the n-layer at the n/i interface and, consequently, to a larger band discontinuity. Obviously, for our cells this does not lead to a decrease of $V_{oc,}$ but to a slight improvement of the cell parameters. The best cell V_{oc} and *FF* of sample 6 are close to the best values for micromorph cells in literature [18, 19, 20].

To test the effect of a damaged bottom cell i/p interface on the SR of a tandem cell, F.A. Rubinelli et al. performed computer simulation with D-AMPS [21] based on our experimental data and on the fittings performed previously on the single and tandem a-Si:H and μc-Si:H solar cells [22,23,24]. By putting a 20 nm defective (~5 × 10^{18} cm^{-3}) a-Si:H layer in the bottom cell i-layer near the i/p interface, a dark SR matching the light SR of the top cell was observed, similar to that shown in Fig. 7.1a [21]. The extra current, or the leaking current, was explained to be a result of thermally generated e-h pairs in the highly defective thin regions, in which the electron quasi Fermi-level can even lay below the hole quasi Fermi-level. These thermally generated carriers can not be distinguished from the e-h pairs created by the light source (in this case the probe monochromatic beam), and therefore appear to be an extra current of the dark SR.

The effect of the existence of a thin defective region (DR) in the other part of the i-layer and in the p type μc-Si:H layer was also explored. The simulation results showed that the enhancement of dark SR decreases when the DR is shifted farther from the i/p interface in the i-layer and practically disappears when it is at the i/n interface [21]. In order to produce the same effect with the DR inside the p-layer (boron doped μc-Si:H), an unrealistic dangling bond defect density of 5 × 10^{19} cm^{-3}, higher than the ionized dopant density, has to be used [21]. These results suggested that a defective region near the i/p interface, which is formed during the deposition of μc-Si:H n-layer of the top cell, is responsible for the "leaking current" of the dark SR.

7.1.5 Summary and conclusions

In this section, the effect of adding a thin n-a-Si:H layer to the completely μc-Si:H TRJ of our micromorph n-i-p cells has been studied. Dark current conduction through the bottom cell of cells with only μc-Si:H n- and p-layers, which manifests itself by dark and

bottom cell SR measurements that deviate from normal cell behaviour, is most likely due to damage induced to the bottom cell during the top cell μc-Si:H n-layer deposition. Upon reduction of the n-layer thickness, which means a shorter exposure of the bottom cell to the n-layer deposition conditions, less 'leakage' in dark SR is observed. A combination of a thinner μc-Si:H n-layer and the insertion of a 5 nm n-a-Si:H layer between the μc-Si:H layers of the TRJ reduces the 'leakage' to almost zero. The amorphous layer could act as a barrier against the diffusion of hydrogen into the bottom cell during the μc-Si:H n-layer deposition.

The almost complete reduction of charge leakage is accompanied by an improvement of $V_{oc,}$ *FF* and R_{sc}. For the most successful TRJ, with the structure p-μc-Si/air break/n-a-Si:H/air break/n-μc-Si, the values for these parameters were 1.40 V, 0.74 and 12.1 kΩcm^2, respectively. In the improvement of the cell, the energy band continuity at the n/i interface was found not to be the dominant reason for the observed effects, in contrast to suggestions made by Pellaton Vaucher et al.

7.2 High Quality Hot-wire Microcrystalline Silicon for Efficient Single and Multijunction n-i-p Solar Cells [25]

In this section, the potential of hot-wire chemical vapour-deposited (HWCVD) microcrystalline silicon (μc-Si) for use in solar cells is explored. Incorporation of the material in the current limiting bottom cell of two tandem cells on plain stainless steel resulted in *FF* values as high as 0.77, which is much higher than the highest single junction *FF*. A combination of experiments, calculations and computer simulations was employed to identify causes for the observed high tandem cell *FF* values. Both the light intensity and the spectral composition of the bottom cell illumination in a tandem were found to contribute to an increase of the bottom cell *FF*. The fact that the operational voltage of a tandem cell is higher than that of the current-limiting subcell, was calculated to lead to a tandem *FF* that can be far higher than that of the limiting cell. Computer simulations with the D-AMPS computer code show that the current mismatch in a tandem cell reduces the recombination in the current-limiting cell, possibly by slightly enhancing the internal field of that cell.

7.2.1 Introduction

Intrinsic microcrystalline silicon (μc-Si) is very suitable for use in highly efficient single and multijunction thin film silicon solar cells. For single junction μc-Si:H p-i-n cells, efficiencies around 10% have been reported [26,27], whereas tandem and triple

junction cells with a μc-Si:H absorber in the bottom cell have yielded 14.1% [28] and 15.0% [7], respectively.

Using hot-wire chemical vapour deposition (HWCVD), we have developed μc-Si:H material close to the amorphous-to-microcrystalline phase transition, which has a high optoelectronic quality [5,29] and is an intended bottom cell absorber layer in n-i-p-configured triple junction solar cells. Single junction n-i-p cells on plain stainless steel with this material as an intrinsic layer, showed V_{oc} and *FF* values as high as 0.54 V and 0.72 [30], respectively. For bottom-cell limited tandem cells with this material as their bottom cell intrinsic layer, we observe *FF* values that are larger than the best single junction value [30, 31]. In this section, we present possible causes for this observation, making use of experiments, calculations and computer simulations.

7.2.2 Experimental details

All solar cells described in this section have HWCVD intrinsic and PECVD (13.65 MHz) doped layers and were deposited in a multi-chamber ultra-high vacuum system following an n-i-p sequence. Intrinsic protocrystalline silicon (proto-Si, deposition rate 10 Å/s) [5] was deposited from undiluted silane, whereas μc-Si:H (deposition rate 2.1 Å/s) [5,29] was obtained with a hydrogen dilution ratio of 0.95 (H_2-flow/total flow). For the deposition of both materials, which was performed at a substrate temperature of around 250°C, tantalum wires were used. A 0.13 cm^2 active cell area was defined by an indium tin oxide top contact with an evaporated gold grid. A detailed description of the cell structure can be found in [31]. Current density-voltage (*J-V*) measurements were performed by means of a calibrated dual source solar simulator, which has an illumination intensity of AM1.5. Spectral response (SR) measurements of single junction cells were performed with a Xenon lamp, which acts as a source for both the monochromatic probe beam and the bias light.

Computer simulations were performed with the D-AMPS computer code [33], extended by F.A. Rubinelli (INTEC, Universidad Nacional del Litoral, Santa Fe, Argentina).

7.2.3 Results and discussion

Since our HWCVD μc-Si:H material was intended for use as a long wavelength absorber layer in multijunction solar cells, it was tested in two tandem cell stacks, which were deposited on plain stainless steel [30,31]. In the first one, which will be referred to as tandem I, a bottom cell with a 1.5 μm μc-Si:H i-layer was completed with a top cell having a 0.20 μm HWCVD proto-Si layer. In the second one, tandem II, both cells had

µc-Si:H i-layers with top and bottom cell thicknesses of 1.0 and 2.0 µm. The V_{oc}, *FF* and top and bottom cell current densities of both tandems are shown in Table 7-3. From this, it is clear that both tandem cells are current-limited by the µc-Si:H bottom cell. The current mismatch in tandem II is much stronger than that in tandem I, which is due to the fact that the former was originally designed as the middle bottom stack of a triple junction solar cell [31]. Furthermore, the *FF* of both tandem cells is considerably higher than our highest observed single junction *FF* of 0.72, which, in addition, was achieved for a considerably thinner i-layer of 1.0 µm [30]. The V_{oc} values are equal to the expected sum of the subcell V_{oc}'s.

Table 7-3 V_{oc}, *FF* and the top and bottom cell current densities of tandem I and II; the current densities were calculated from the measured spectral response

	V_{oc} (V)	*FF*	Jtop(mA/cm^2)	Jbottom(mA/cm^2)
Tandem I	1.38	0.75	7.23	6.30
Tandem II	1.04	0.77	9.11	4.42

The higher *FF* of the tandem cells compared to that of the best single junction cell must be related to the difference in cell structure between a single junction and a tandem cell: the current- limiting bottom cells are now topped with a complete cell, instead of a metal oxide top contact. As a consequence, the illumination intensity of the bottom cell in a tandem structure is lower than that of a single junction cell.

To investigate the effect of this on the *FF*, a series of *J-V* measurements at different illumination intensities was performed on single junction cells [30]. Neutral density filters were used to attenuate the AM1.5 spectrum from our solar simulator and a red-light transmitting filter (Schott RG630) was employed to simulate the illumination experienced by the µc-Si:H bottom cell in a tandem structure. Fig. 7.5 displays the results for a cell with a 2.0 µm i-layer. It can be seen that the *FF* increases upon a reduction of the light intensity, which is an indication of drift-driven charge carrier transport [30]: recombination is reduced because of a lower volume generation rate of charge carriers, which is reflected in a higher *FF*. The differential resistances at short and open circuit conditions (R_{sc} and R_{oc}, respectively) increase with a decreasing light intensity. For the simulated bottom cell illumination conditions, the highest *FF* increase is observed. This can be explained by a more homogeneous charge carrier generation profile: the shorter wavelengths, which are fully absorbed near the i/p-interface of the cell and generate a high charge carrier density in that region, are filtered out. As a result, the recombination rate near this interface reduces, which has a beneficial effect on the *FF*. In addition, the volume generation of charge carriers by the red-filtered light is lower than that by neutrally-filtered light with the same total photon flux, because the latter light on average consists of wavelengths that are less well absorbed in the solar cell.

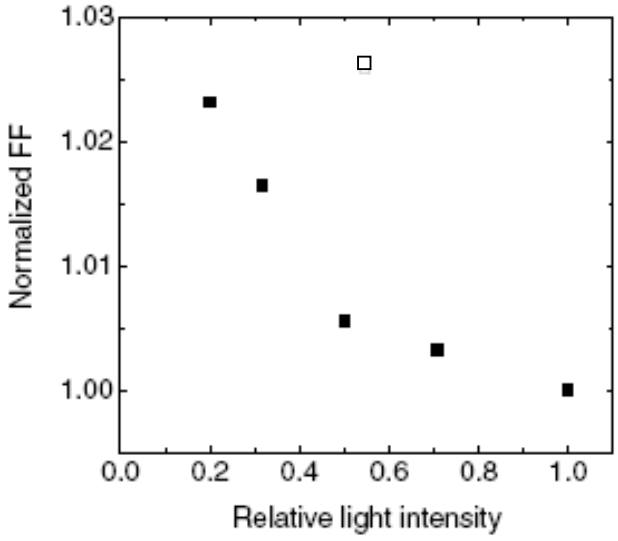

Fig. 7.5 *FF* value of a 2.0 µm µc-Si:H single junction cell on plain stainless steel, measured under filtered AM1.5 illumination and normalized to the value at AM1.5 intensity. Filtering was performed using neutral density filters (closed squares) and a red light transmitting cut-off filter (Schott RG630, open square). The light intensities are relative to AM1.5.

A second difference between single junction and tandem cells is the fact that a tandem cell operates at higher voltages than any of its single junction cells. In a current-mismatched tandem cell, the *J-V* characteristics are determined by the subcell that limits the output current. The *J-V* curve of the tandem cell can in that case be considered as the *J-V* curve of its current-limiting cell, shifted to a higher voltage by a value equal to V_{oc} of the non-limiting subcell. Fig. 7.6a shows such a shift for tandem cells with a current-limiting µc-Si:H bottom cell and either a µc-Si:H or a proto-Si top cell. The *J-V* curve of the bottom cell is the measured curve for the red-filtered illumination of the 2.0 µm single junction µc-Si:H cell discussed above. Shifting this along the voltage axis by 0.55 and 0.85 V, which are typical V_{oc} values for a µc-Si:H and proto-Si top cell, yields the tandem cell *J-V* curves. In the figure it can be seen that the maximum power point (mpp) of the tandem cells lies at a higher J value than that of the bottom cell curve. The V values of the point are located further away from V_{oc} than the value of the bottom cell, but the relative difference, which is of importance for the *FF*, is smaller. As a result, the *FF* values calculated from the tandem curves, being 0.74 (µc-Si:H top cell) and 0.77 (proto-Si top cell), are larger than that of the 'bottom cell' of 0.63. As is shown in Fig. 7.6b, the calculated tandem *FF* increases with the top cell V_{oc} and flattens off at higher

V_{oc} values. For the experimental situation, this means that the potential *FF* of tandem cells will increase with an increasing V_{oc} of the non-limiting cell.

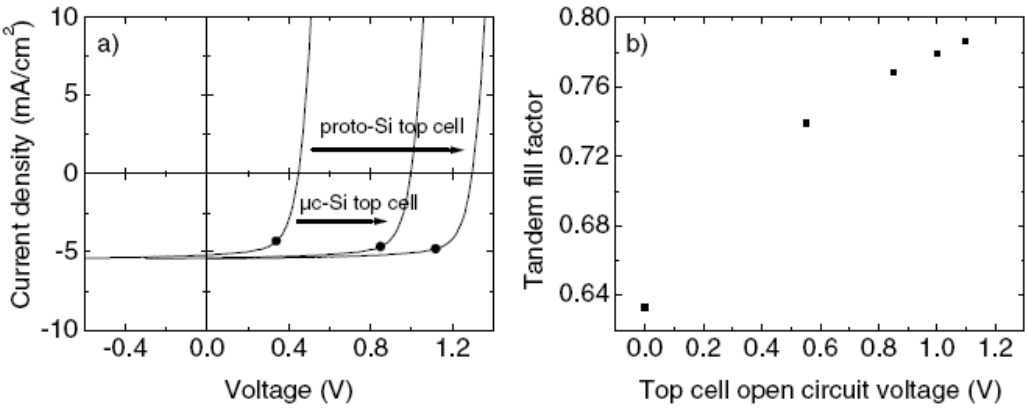

Fig. 7.6 (a) Construction of a tandem cell *J-V* curve by shifting the *J-V* curve of the limiting subcell (in this case a µc-Si:H bottom cell) along the voltage axis by the V_{oc} of the top cell (in this case 0.55 V for a µc-Si:H top cell and 0.85 V for a proto-Si one). The black dots indicate the MPP (maximum power point), and (b) *FF* values calculated from the constructed *J-V* curves versus top cell V_{oc}.

It should be noted that the presented construction of the tandem cell *J-V* curve does not account for the higher internal resistance (series resistance) of tandems with respect to single junction cells. The measured tandem cell R_{oc} values (12-14 Ωcm^2) are somewhat higher than that of the bottom cell *J-V* curve in Fig. 7.6a (10 cm^2), which means that the expected tandem cell *FF* is lower than the calculated one. Because the tandem cell V_{oc} is 2-3 times higher than that of the current-limiting bottom cell, the tandem cell *FF* will, however, still be higher.

To investigate the effect of current mismatch on the *FF* of tandem cells in more detail, we performed computer simulations on an a-Si:H/µc-Si:H tandem cell structure. Starting from a nearly matched structure, which has i-layer thicknesses of 0.15 µm for the top and 2.75 µm and for the bottom cell, the bottom cell thickness was varied to yield top- and bottom-cell limited cases. Because of the constant top cell thickness, the illumination of the top and bottom cell is the same for all simulations and does, therefore, not influence observed changes in tandem cell *FF*. From the resulting *FF* values, displayed in Fig. 7.7a, it follows that the *FF* is minimal for the matched case and increases upon current mismatch. In Fig. 7.7b, it can be seen that the recombination rate in the top cell decreases with an increasing thickness of the bottom cell, whereas the bottom cell recombination increases. For mismatched tandems, the recombination rate in the current- limiting cell is less than the rate in the current-matched case. In the case of the bottom limited cells, this can be ascribed to the fact that the bottom cell i-layer is

thinner than for the matched tandem, which leads to a stronger internal field and a shorter average travelling distance of the charge carriers. For the top-limited cells the situation is different: the top cell thickness and, therefore, the internal field generated in the top cell by the doped layers, is the same for all cells. The reduction of the recombination rate can be a result of the accumulation of holes in the bottom cell near the tunnel recombination junction (TRJ) [33]. This accumulation, which is due to the mismatch of the top and bottom cell currents, leads to a weakening of the internal field in the non-limiting bottom cell, which enhances the recombination rate in this cell. At the same time, the internal field in the top cell may be somewhat strengthened, which reduces recombination. This effect becomes stronger for a stronger current mismatch. Consequently, the *FF* of the tandem cell increases, which is the trend for the top-limited cells in Fig. 7.7a. The same effect can also be present in the case of the bottom-limited cells, where it adds to the strengthening of the field that results from the thinner i-layer.

The three discussed *FF* enhancement effects in current-mismatched tandem cells can side-by-side play a role in determining experimental tandem cell *FF* values. Irrespective of which one is dominating, all three are linked to the properties of the current-limiting cell, which determine the response on the effects and, thus, the tandem cell *FF* that will be observed.

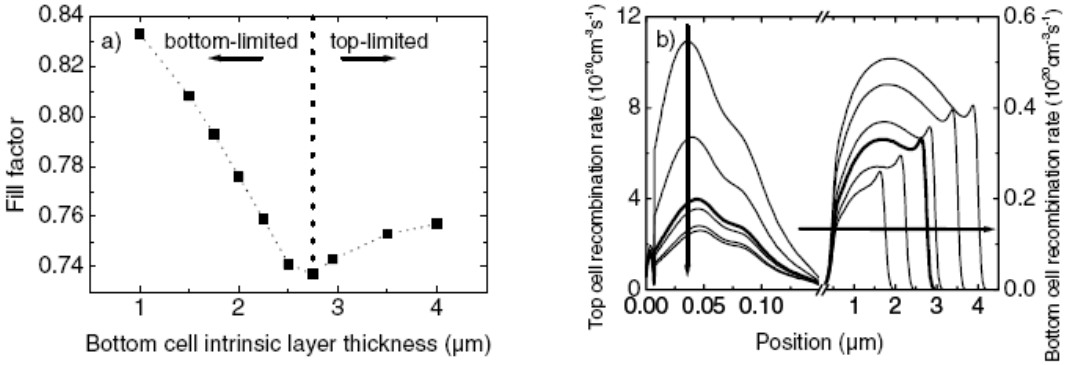

Fig. 7.7 (a) simulated *FF* of a-Si:H/µc-Si:H tandems obtained for a fixed top cell thickness of 0.15 µm and various bottom cell thicknesses, and (b) top and bottom cell recombination rates under mpp operation for various bottom cell thicknesses. The thick curve indicates the matched case; the arrows indicate in which direction the bottom cell thickness increases.

7.2.4 Summary

Two bottom-cell limited tandem cells, a proto-Si/µc-Si:H and a µc-Si/µc-Si:H one, incorporating HWCVD absorber layers, were prepared. The respective *FF* values of these

cells under AM1.5 illumination were 0.75 and 0.77, which is higher than the best value for a single junction cell with the same μc-Si:H intrinsic layer material. To gain understanding about this, factors governing the *FF* in bottom-cell limited tandem cells were investigated. It was found that the illumination conditions of bottom cells in tandems increase the bottom cell *FF*. Calculations show that the fact that a tandem cell operates at a higher voltage than any of its subcells leads to a tandem cell *FF* that is higher than that of the current-limiting subcell. Computer simulations suggest that a mismatch of the subcell currents induces a small enhancement of the internal field in the current-limiting subcell, which increases the sub cell's *FF* and, thereby, the tandem cell's *FF*.

7.3 Improvement of the efficiency of triple junction n-i-p solar cells with hot-wire CVD proto- and microcrystalline silicon absorber layers [34]

7.3.1 Introduction

Making use of the single junction proto-Si:H and proto-SiGe:H n-i-p cells originally developed by M. van Veen et al [5] and R. Jimenez Zambrano et al [39], and implementing the further improvement on solar cell p/ITO/metal interfaces [40], efficiencies of single and multijunction n-i-p cells developed on opaque substrates was further improved. In this section, we summarize the results of the improved single junction μc-Si:H bottom cell and the triple junction cell within the frame of this research, and discuss the room for further improvement of solar cell efficiency.

7.3.2 Experimental details

The structure of the triple junction solar cell is stainless steel/rough Ag/ZnO/ μc-Si:H n-i-p bottom cell/proto-SiGe:H n-i-p middle cell/proto-Si:H n-i-p top cell/ITO/Au grids. The silicon layers were deposited in the PASTA multi-chamber ultra-high vacuum system. Doped layers and intrinsic proto-SiGe:H [43] were prepared using 13.56 MHz PECVD, whereas HWCVD was applied to fabricate intrinsic proto-Si:H [41] and μc-Si:H [5,30,38,44,45]. For the hot-wire deposition, two straight Ta filaments were used, through which a current of 10.5 A was passed, yielding a wire temperature of approximately 1850 ºC. The calibrated substrate temperature for stainless steel foil was 270 ºC. Proto-Si:H was deposited from undiluted SiH_4, whereas H_2-diluted SiH_4 with a H_2 dilution R_H (R_H is defined as the H_2-flow divided by the total gas flow) of around

0.95 was used for the μc-Si:H deposition. Detailed deposition parameters for each layer are listed in Table 2.1 of Chapter 2.

Two types of substrates were used: a Ag/ZnO TBR made on stainless steel (SS) foil in our laboratory [35] and a SS/Ag/ZnO substrate provided to us by United Solar Ovonic Corporation [44]. Indium-tin-oxide served as an anti-reflecting TCO top window; an evaporated gold grid on top facilitated a proper charge carrier collection. All metal oxide layers were obtained by magnetron sputtering in our SALSA system as well as the textured Ag of the TBR. All the cells experienced post-deposition annealing at a temperature around 160 ºC in a N_2 atmosphere [38, 43]. Unless mentioned otherwise, all the AM1.5 *J-V* data were obtained with the ITO mask [see section 2.3.1.2].

7.3.3 Results and discussion

7.3.3.1 Efficiency of single and triple junction solar cells with hot-wire i-layers

For single junction n-i-p structured μc-Si:H cells, implementation of a textured back reflector (TBR) [35], together with an optimization of the n-layer [36] and the use of a reversed hydrogen profiling technique for the deposition of i-layer [37], yielded a strong improvement of the cell efficiency compared to previous results.

Fig. 7.8 shows the spectral response (SR) curves of two single junction μc-Si:H cells, both with 2.0 μm thick HWCVD absorber layers. The dashed curve was obtained for a cell on plain SS, with an i-layer grown with a constant hydrogen dilution of 0.952. The solid curve represents an optimized cell on a TBR deposited in our lab [35]. For this cell, the n-layer was optimized, the i-layer deposition was started slightly below the equilibrium substrate temperature of 250 ºC ('dynamic start') and the hydrogen dilution was profiled: the bottom 1.0 μm was grown at a 0.948 hydrogen dilution, the top 1.0 μm at a 0.952 dilution. The optimization of the μc-Si:H cell has been discussed in more detail in chapter 4 [38]. The solar cell AM1.5 *J-V* parameters of the best cell are listed in Table 7-4, the AM1.5 *J-V* plot in Fig.4.2.

From Fig. 7.8, it can be seen that the SR of the cell on the TBR has increased throughout the measured wavelength range [29], which is due to a combination of enhanced light-trapping and a reduced reflection at the rougher front interface [48] of the cell. The resulting J_{sc} of 23.39 mA/cm^2 is good value for such a thin i-layer. The cell efficiency of 8.5% is a record value for a single junction μc-Si:H n-i-p cell with a hot-wire absorber layer. It is in line with the best results reported for similar cells made on the same type of substrate with VHF plasma-enhanced CVD i-layers [49].

Table 7-4: AM1.5 *J-V* parameters of the best microcrystalline single junction and triple cells.

Type of cell	V_{oc} *(V)*	*FF*	J_{sc} *(mA/cm²)*	***Efficiency (%)***
Single junction µc-Si:H n-i-p	0.55	0.66	23.4	8.5
Triple junction proto-Si/ proto-SiGe:H/ µc-Si:H	1.977	0.661	8.35	10.91

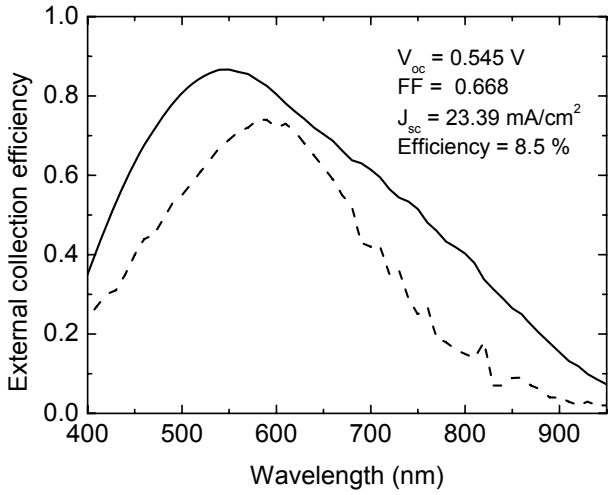

Fig. 7.8 Improvement of the SR of a 2.0 µm µc-Si:H solar cell on a TBR (solid line) with respect to that of a 2.0 µm cell on plain stainless steel (dashed line). The AM1.5 light *J-V* parameters of the cell on the TBR are shown.

Fig. 7.9a and b show the light *J-V* curve and SR of a proto-Si:H/proto-SiGe:H/µc-Si:H triple junction n-i-p cell on a substrate from United Solar. The implementation of a TBR, the use of proto-SiGe:H instead of µc-Si:H for the middle cell absorber layer and a better matching of the subcell currents have resulted in a cell efficiency of 10.91% (The *J-V* parameters of this cell are also listed in Table 7-4). This is more than twice that of the proto-Si:H/µc-Si:H/µc-Si:H triple junction cell on plain SS we obtained in the beginning of the triple project [30]. Meanwhile, the total active layer thickness has decreased from over 3.0 µm to about 2.3 µm, which means a reduction of more than 23% of total deposition time has been saved. The improvement of the µc-Si:H bottom cell quality and the use of proto-SiGe:H in the middle cell have increased V_{oc} from 1.77 V to 2.024 V. The SR shows that the subcell currents are matched quite well and the middle cell is current-limiting.

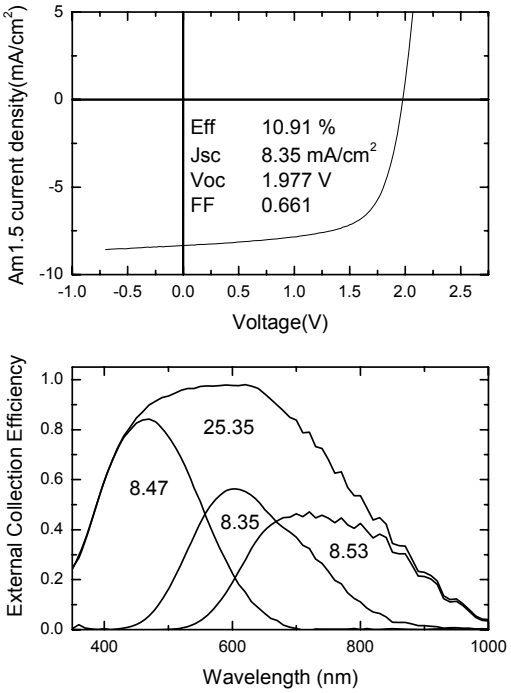

Fig. 7.9 a) AM1.5 light *J-V* curve and b) SR of a proto-Si:H/proto-SiGe:H/μc-Si:H triple junction solar cell on a TBR.

7.3.3.2 Light soaking result

The single junction sample shown in Table 7-4 was put into the light soaking setup to study the stability of this cell. Unfortunately, the cells on the upper edge of the substrate, including the best cell, were all damaged during sample handling; also, no proper (1% Al doped) ZnO target was available during the last part of this research, so that we could not make more cells on the best cell deposition condition or further optimize the i-layer deposition parameters to obtain a higher single cell efficiency. Table 7-5 summarises the average AM1.5 *J-V* characteristics of best 5 cells for those remained on that substrate, data were collected before light soaking, after 1500 hours soaking and after post-soaking annealing at 160 ^{o}C in a N_2 atmosphere.

From the data listed in Table 7-5, it can be seen that the sample shows excellent stability, with an average decrease of only 2.5% in their efficiency after 1500 hours light soaking. Similar to that observed previously by A. Gordijn on μc-Si:H p-i-n cells with a VHF i-layer, V_{oc} of the cells in this hot-wire sample also show a trend of increase (+2 mV), though the amount of difference is not large compared to the measurement error

bar (~ 1 mV). Upon post light-soaking annealing, the V_{oc} increases even further (+ 6 mV), accompanied by a clear drop in J_{sc} (-0.8 mA/cm^2). The *FF* of the cells after light-soaking show practically no difference than that measured before, though a slight increase might exist. The small increases of V_{oc} of μc-Si:H cells after light soaking have been postulated to be related to the transition of silicon nano-crystallites to an amorphous structure, which may result in an increase of effective bandgap in the i-layer. The reason that the V_{oc} increases the most after post light-soaking annealing instead of during the 1500 hours light-soaking is, however, not clear. Since the cell was light-soaked without encapsulation, the possibly change in the ITO/p/i region has to be taken into account the succeeding research.

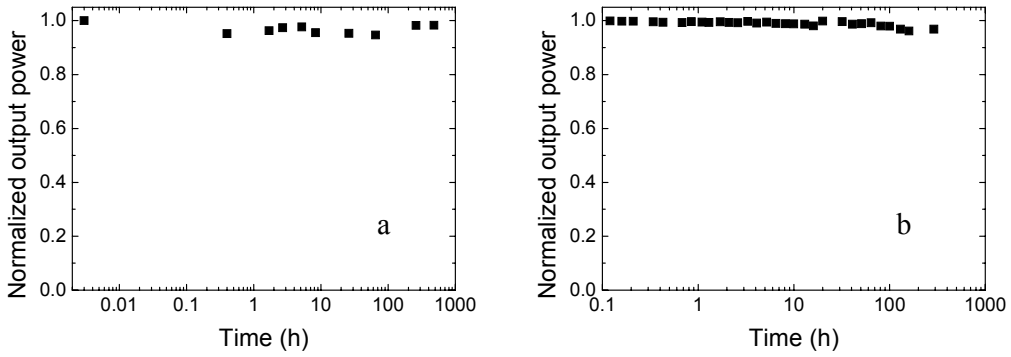

Fig. 7.10 a) Normalized light-induced performance evolution for a 2 μm thick μc-Si:H n-i-p cell, and b) Normalized light-induced performance evolution for a 2.5 um thick proto-Si/proto-SiGe/μc-Si:H triple junction n-i-p solar cell.

Table 7-5 *J-V* of average best 5 single junction μc-Si:H cells before and after AM1.5 light soaking for 1500 hours at 50 ^{o}C .

	Eff.(%)	J_{sc} (mA/cm^2)	V_{oc} (V)	*FF*	Roc (Ωcm^2)	Rsc (Ωcm^2)
As deposited (annealed after deposition)	8.2	23.2	0.538	0.657	2.6	631
Before soaking	8.1	23.1	0.535	0.653	2.7	592
1500hrs light-soaked	8.0	22.7	0.537	0.654	2.7	594
Annealed after soaking	8.1	22.4	0.544	0.661	2.7	531

Fig. 7.10b shows the degradation kinetics of the triple cell shown in Table 7-4, after around 300 hrs light soaking, the cell shows approximately 3% degradation, which is among the best performance for cells having similar structure. Longer degradation experiments are necessary for the succeeding study.

7.3.3.3 Room for the further improvement of triple cell efficiency

Although our μc-Si:H single junction n-i-p cells with a hot-wire i-layer have shown comparable efficiency to that of cells deposited on the similar substrate with a VHF i-layer [49], the triple cell result is still lower than that of the world best values. This is due to a few reasons:

1. The morphology of the substrate surface is not yet optimal, as we discussed in Chapter 3.
2. Though annealing can considerably improve the quality of TCO/p/i region, the ITO and boron doped μc-Si:H layer can still be optimized, which shall further improve the carrier collection of single and multiple junction n-i-p cells.
3. The proto-SiGe:H used as the i-layer of middle cell needs further optimization. Experimental data showed that, a structure transition from proto-SiGe:H to μc-SiGe:H happens while further increase the thickness of this layer. As a consequence, current density of the middle cell is limited, which resulted in a lower current of the whole triple junction cells [51]. One of the solutions for that is to shift the deposition parameters a bit further away from the phase transition regime (the proto-regime) and optimize the i-layer accordingly. This is the subject to be further studied.

7.3.4 Summary and conclusions

Solar cell characteristics and spectral responses were presented of thin film silicon n-i-p solar cells with hot-wire chemical vapour-deposited absorber layers. For a single junction cell with a 2.0 μm μc-Si:H intrinsic layer on a ZnO/Ag TBR, sputtered onto SS, an efficiency of 8.5% was obtained, with a $V_{oc,}$ J_{sc} and FF of 0.545 V, 23.39 mA/cm^2 and 0.668. This efficiency is a record value for this type of cells with a hot-wire absorber layer. A proto-Si:H/proto-SiGe:H/μc-Si:H triple junction cell with hot-wire top and bottom cell absorber layers showed a V_{oc} of 1.977 V, a J_{sc} of 8.35 mA/cm^2 and a FF of 0.661, which combine to an efficiency of 10.9%. The cells show outstanding stability against prolonged light-soaking, which can be attributed to the triple junction structure, i.e. thinner i-layers in each subcell, and the use of high quality light absorbing materials, including that of hot-wire deposited proto-Si:H and μc-Si:H, and the PECVD deposited proto-SiGe:H.

References

1 R.L. Stolk, H. Li, C.H.M. van der Werf, R.E.I. Schropp, 19th European Photovoltaic Solar Energy Conference, Paris, 2004, 3DV1.52.

2 M.K. van Veen, R.E.I. Schropp, J. Appl. Phys. 93 (2003) 121.

3 S. Klein, F. Finger, R. Carius, O. Kluth, L. Baia Neto, H. Wagner, M. Stutzmann, Proceedings 17th European Photovoltaic Solar Cell Conference, Munich, Germany, 22 – 26 October 2001, p. 2965.

4 R. E.I. Schropp, Thin Solid Films 451-452 (2004) 455.

5 M.K. van Veen, *Tandem solar cells deposited using hot-wire chemical vapor deposition*, Ph.D. thesis, Utrecht University, The Netherlands, 2003.

6 M. Fonrodona, D. Soler, J. Bertomeu, J. Andreu, Thin Solid Films 395 (2001) 125.

7 M.K. van Veen, C.H.M. van der Werf, J.K. Rath, R.E.I. Schropp, Thin Solid Films 430 (2003) 216.

8 R.E.I. Schropp, J.K. Rath, IEEE T. Electron. Dev. 46 (1999) 2069.

9 M.K. van Veen, R.E.I. Schropp, Thin Solid Films 403 (2002) 135.

10 M.K. van Veen, P.A.T.T. van Veenendaal, C.H.M. van der Werf, J.K. Rath, R.E.I. Schropp, J. Non-Cryst. Solids 299 (2002) 1194.

11 R.E.I. Schropp, K.F. Feenstra, E.C. Molenbroek, H. Meiling, J.K. Rath, Phil. Mag. B 76 (1997) 309.

12 G.E.N. Landweer, C.H.M. van der Werf, R.W. Stok, J.W. Metselaar, R.E.I. Schropp, Proceedings of the 12th European Photovoltaic Solar Energy Conference, Amsterdam, The Netherlands, 11-15 April 1994, p. 1284.

13 J.K. Rath, R.E.I. Schropp, Sol. Energ. Mat. Sol. C. 53 (1998) 189.

14 F.A. Rubinelli, J.K. Rath, R.E.I. Schropp, J. Appl. Phys. 89 (2001) 4010.

15 S. Guha, C.C Yang, X.X. Xu, US Patent, no. 5,977,476 (1999).

16 N. Pellaton Vaucher, B. Rech, D. FI$_{sc}$her, S. Dubail, M. Goetz, H. Keppner, N. Wyrsch, C. Beneking, O. Hadjadj, V. Shklover, A. Shah, Sol. Energ. Mat. Sol. C. 49 (1997) 27.

17 J. Löffler, A. Gordijn, R.L. Stolk, H. Li, J.K. Rath, R.E.I. Schropp, Sol. Energ. Mat. Sol. C. 87 (2005) 251.

18 B. Rech, T. Roschek, T. Repmann, J. Müller, R. Schmitz, W. Appenzeller, Thin Solid Films 427 (2003) 157.

19 J. Meier, J. Spitznagel, U. Kroll, C. Bucher, S. Faÿ, T. Moriarty, A. Shah, Thin Solid Films 451-452 (2004) 518.

20 K. Yamamoto, M. Yoshimi, Y. Tawada, S. Fukuda, T. Sawada, T. Meguro, H. Takata, T. Suezaki, Y. Koi, K. Hayashi, T. Suzuki, M. Ichikawa, A. Nakajima, Sol. Energ. Mat. Sol. C. 74 (2002) 449.

21 F.A. Rubinelli, R.L. Stolk, A. Sturiale, J.K. Rath, R.E.I. Schropp, J. Non-Cryst. Solids 352 (2006) 1876.
22 E. Klimovsky, A. Sturiale and F.A. Rubinelli, Thin Solid Film 338-440 (2006) 686.
23 J.J.H. Strengers, F.A. Rubinelli, J.K. Rath and R.E.I. Schropp, Thin Solid Films 501 (2006) 291.
24 F.A. Rubinelli, J.K. Rath, R.E.I. Schropp, J. Appl. Phys. 890 (2001) 4010.
25 R.L. Stolk, H. Li, R.H. Franken, C.H.M. van der Werf, J.K. Rath and R.E.I. Schropp, Mater. Res. Soc. Symp. Proc, 910 (2006) A.26.03.
26 A. Gordijn, J. Francke, L. Hodakova, J.K. Rath, R.E.I. Schropp, Mater. Res. Soc. Symp. Proc. 862 (2005) A10.3.
27 Y. Mai, S. Klein, R. Carius, H. Stiebig, X. Geng, F. Finger, Appl. Phys. Lett, 87. (2005) 073503 3. K. Yamamoto, M. Yoshimi, Y. Tawada, S. Fukuda, T. Sawada, T. Meguro, H. Takata, T. Suezaki, Y. Koi, K. Hayashi, T. Suzuki, M. Ichikawa, A. Nakajima, Sol. Energ. Mat. Sol. C. 74 (2002) 449.
28 K. Yamamoto, A. Nakajima, M. Yoshimi, T. Sawada, S. Fukuda, T. Suezaki, M. Ichikawa, Y. Koi, M. Goto, T. Meguro, T. Matsuda, M. Kondo, T. Sasaki, Y. Tawada, Proc. 15th PVSEC, 10- 15 October 2005, Shanghai, China, p. 529.
29 R.L. Stolk, H. Li, R.H. Franken, J.J.H. Strengers, C.H.M. van der Werf, J.K. Rath, R.E.I. Schropp, J. Non-Cryst. Solids 352 (2006) 1933.
30 R.L. Stolk, H. Li, C.H.M. van der Werf, R.E.I. Schropp, Thin Solid Films 501 (2006) 256.
31 R.L. Stolk, J.J.H. Strengers, H. Li, R.H. Franken, C.H.M. van der Werf, J.K. Rath, R.E.I. Schropp, Proc. of the 20th EPVSEC, 6-10 June 2005, Barcelona, Spain, p. 1655.
32 P. Chatterjie, P.J. McElheny, S.J. Fonash, J. Appl. Phys. 67 (1990) 3803.
33 F.A. Rubinelli, R.L. Stolk, J.K. Rath and R.E.I. Schropp, J. Non-Cryst. Solids 352 (2006) 1876-1879.
34 R.L. Stolk, H. Li, R.H. Franken, J.W.A. Schüttauf, C.H.M. van der Werf, J.K. Rath and R.E.I. Schropp, extended abstract of the 4th international Conference on Hot-Wire CVD (Cat-CVD) process, October 4-8, 2006, Takayama, Gifu, Japan, 181.
35 R. H. Franken, *Transparent conducting oxide contacts and textured metal back reflectors for thin film silicon solar cells*, PhD thesis, Utrecht University, the Netherlands, 2006.
36 See chapter 3 of this thesis.
37 See chapter 4 of this thesis.
38 H. Li, R.H. Franken, R.L. Stolk, C.H.M. van der Werf, J.K. Rath, R.E.I. Schropp, extended abstract of the 4th international Conference on Hot-Wire CVD (Cat-CVD) Process, October 4-8, 2006, Takayama, Gifu, Japan, 173.

39 R. Jimenez Zambrano, *Stable Hydrogenated Amorphous Silicon Germanium for Photovoltaic Applications. Experimental and Computational Studies,* PhD thesis, Utrecht University, The Netherlands, 2003.
40 See chapter 5 of this thesis.
41 M.K. van Veen and R.E.I. Schropp, Appl. Phys. Lett. 82 (2003) 287.
42 R.L. Stolk, H. Li, C.H.M. van der Werf and R.E.I. Schropp, Thin Solid Films 501 (2006) 256.
43 H. Li, R.L. Stolk, C.H.M. van der Werf, R.H. Franken, J.K. Rath and R.E.I. Schropp, J. Non-Cryst. Solids 352 (2006) 1941.
44 H. Li, R.H. Franken, R.L. Stolk, C.H.W. van der Werf, J.K. Rath, R.E.I. Schropp, Mat. Res. Soc. Symp. Proc. 989 (2007) A18.3.
45 H. Li, R.H. Franken, R.L. Stolk, J.K. Rath, R.E.I. Schropp, Gettering and Defect Engineering in Semiconductor Technology (GADEST), Erice, Italy, 14-19 Oct. 2007.
46 www.unisolar.com
47 A. Gordijn, R. Jimenez Zambrano, J.K. Rath, R.E.I. Schropp, IEEE Trans. Elec. Dev. 49 (2002) 949.
48 S. Koynov, M.S. Brandt and M. Stutzmann, Appl. Phys. Lett. 88 (2006) 203107.
49 B. Yan, G. Yue, J.M. Owens, J. Yang and S. Guha, 4th WCPEC, 7-12 May 2006, Waikoloa Village, Hawai (USA).
50 R. Jimenez Zambrano, F. A. Rubinelli, W. M. Arnoldbik, J.K. Rath and R.E.I. Schropp, Sol. Energ. Mat. Sol. C. 81 (2004) 73-86.
51 H. Li, R.L. Stolk, J.K. Rath, R.E.I. Schropp, to be published.

8

Summary

A number of aspects in developing high efficiency thin film silicon based solar cells on flexible substrates are discussed.

Starting from Chapter 2, a review on the filament surface reaction mechanism of hot-wire chemical vapour deposition (HWCVD) is given, together with the key factors in performing a reliable and accurate solar cell characterization.

Chapter 3 discusses the performance of hydrogenated microcrystalline silicon (μc-Si:H) n-i-p cells directly grown on rough ZnO/Ag substrates, in particular the dependence of the open circuit voltage V_{oc} and the fill factor *FF* on defects created in the i-layer that are induced by the rough substrate. Studies on the microstructure of such samples point out that a substrate with too large Ag grains create a high density of shunting paths in the μc-Si:H i-layer, which eventually results in short-circuiting of the complete device. For cells deposited on a medium rough substrate, the yield of working cells is acceptable, but V_{oc} of the cells decreases with increasing substrate roughness. This is identified to be the result of two most probable mechanisms. One mechanism is that the i-layer is unintentionally doped due to accumulation of impurities such as oxygen,

of which the incorporation takes place through a high density of structural defects, namely low density regions and cracks that are associated with deep valleys at the substrate surface. The other mechanism is related to the tilt angle of crystallites, as they tend to grow perpendicular to the local substrate surface. The collisions of the columnar silicon result in a high density of structural defects, which may introduce deep electronic defects in the μc-Si:H i-layer. This in turn results in an increase in the dark reverse saturation current density J_0 and the diode quality factor n, the former in particular contributing to a decrease in the cell V_{oc}. The formation of low-density stripes and cracks is explained as the result of hydrogen etching of strained silicon bonds in the region where adjacent silicon columns collide. The appearance of these stripes clearly dependents on the nanoscale opening angle of the valleys at the substrate surface. A threshold in the opening angle for low-density stripes to appear of around 110 degrees has been found, which correlates to the bond angle of Si-Si-Si in a μc-Si:H material. This suggest that to reduce the number of structure related electrical defects in μc-Si:H layers developed on a rough substrate, the valleys at the substrate surface should not have steep slopes. In this way, the collision of silicon columns can be avoided. A high *FF* and V_{oc} would then be achievable for solar cells grown on rough substrates.

One common technique to obtain a high efficiency μc-Si:H solar cell is to maintain the structure of μc-Si:H i-layer at the phase transition regime between amorphous and microcrystalline silicon. This is typically done by a technique called hydrogen profiling, by which the H_2 to SiH_4 gas flow ratio is decreased during the i-layer deposition in order to avoid the increase of i-layer crystallinity along the growth direction. For solar cells with a μc-Si:H i-layer deposited by hot-wire CVD, however, we found that the crystallinity decreases, instead of increases, during the layer growth. This is most probably related to the progressing filament aging under constant filament current conditions. In order to obtain a high quality μc-Si:H i-layer with a homogeneous structure and better electronic quality near the phase transition region, in Chapter 4, a *reverse* H_2 profiling technique was developed for hot-wire CVD, which means that the H_2 /SiH_4 gas flow ratio R_H is increased instead of decreased during deposition. The experimental results show an encouraging high efficiency (8.5 %) for μc-Si:H n-i-p cells with a hot-wire CVD i-layer on stainless steel foil coated with rough Ag/ZnO having a still unoptimized substrate surface morphology. Compared to the cells made with a constant R_H, the cells with this profiled i-layer show higher values of all main solar cell parameters, namely the short circuit current J_{sc}, V_{oc}, and *FF*, which was attributed to be the result of better collection of photogenerated carriers in the i-layer. Using, in addition to reverse H_2 profiling, a so-called “cold start” technique, i.e., starting the i-layer deposition at a lower substrate temperature by opening the shutter before the system reaches to a thermal equilibrium, the *FF*’s have been further increased. This is probably

due to a lower electrical defect density in the i-layer, especially near the n/i interface. Our best cell (8.5%) has efficiency comparable to the n-i-p cells developed by UniSolar Ovonic Corp. on stainless steel substrates with similar rough Ag/ZnO coating but using VHF (Very High Frequency) Plasma-Enhanced CVD deposited silicon layers (8.9%). The small difference between these two cells can be attributed to the still quite high substrate temperature (270 ^{o}C) used for our hot-wire deposited i-layer. Further room for improvement of both cells (either with a hot-wire deposited i-layer or with a VHF PECVD i-layer) is thought to be present in the optimization of the substrate surface morphology.

In Chapter 5, the carrier transport barriers discovered near the i/p/ITO region of n-i-p cells is discussed. The discussion starts with a literature overview of the deposition techniques involved for a high quality μc-Si:H p-layer. Emphasizes were put on the difficulty of the nucleation of nanocrystallites on the surface of a device-quality amorphous i-layer, when using a gas mixture of SiH_4, H_2 and $B(CH_3)_3$ (TMB) for the p-layer deposition. The influence of the structural deviation of the p-layer from a heavily doped p-type μc-Si:H layer to an inefficiently doped p-type a-Si:H is discussed for the case of proto-SiGe:H n-i-p cells, where the influence of this deviation is found to be the most serious. Annealing experiments were performed on cells showing an S-shape in their AM1.5 *J-V* plots, due to which the location of the barrier was identified to be at the i/p/ITO region. By optimizing p-layer deposition conditions, the barrier was almost completely removed. The effect of post-deposition annealing on the removal of the carrier transport barrier is further discussed based on the study of the dark *J-V* characteristics of three types of n-i-p cells, i.e., cells with an a-Si:H, a μc-Si:H and a proto-SiGe:H absorber layer individually. The dominating carrier transport mechanism was identified in each of three distinguishable regions in the forward bias range of the J_{dark}-V curves. In the recombination current dominated region, the dark current density (J_{dark}) of all three types of cells decreases after annealing, resulting in an increase of *FF* and V_{oc} in their AM1.5 *J-V* characteristics. This is explained by a field enhancement effect of the post-deposition annealing treatment on the p/ITO interface. The diode quality ~ Voltage dependence (n-V curve) of the proto-SiGe:H cells shows an remaining shoulder near V_{oc} after annealing. This is probably due to a barrier caused by a band misalignment between the proto-SiGe:H i-layer and the unoptimized p-layer. For proto-SiGe:H cells with an optimized μc-Si:H p-layer, this shoulder is not observed. This analysis provides a deep understanding on the dark *J-V* of thin film silicon solar cells.

In Chapter 6, a special phenomenon observed in the external collection efficiency (ECE) of μc-Si:H n-i-p cells is discussed. A largely enhanced ECE curve was observed when the measurement was done with a coloured bias light, such as a blue light. The magnitude of this enhancement decreases with decreasing bias light intensity, and it

increases with decreasing intensity of the monochromatic light. Computer simulations using D-AMPS point out that the mechanism for the observed phenomena is similar to the "photogating" (PG) effect that was observed previously in a-Si:H p-i-n and Schottky devices. The use of the term "photogating" is proposed to be extended to the description of the observed phenomenon in μc-Si:H cells. Simulations point out that a weak electric field and a high density of sub gap defects in the i-layer are the key factors leading to a strongly enhanced PG effect in a μc-Si:H p-i-n structure. This is in agreement with the experimental observation that the PG effect is present in cells even with device quality i-layers but with a lowered internal field due to the existence of an interface barrier near the p/ITO layers. By performing a post-deposition annealing treatment, the barrier can be removed due to which the internal field is enhanced, and thus the PG effect is considerably reduced. The sensitivity of the PG effect on structural defects can be used to find the direction for the optimization of μc-Si:H solar cells in order to have a maximum cell output performance, i.e. a balance between the internal electric field and the maximum i-layer thickness is always necessary in order to transfer a maximum amount of energy from the absorbed incident light.

In Chapter 7, issues related specifically to multijunction thin film silicon solar cells are discussed. Section 7.1 discusses the tunnel recombination junction (TRJ) of multijunction n-i-p cells. Due to the fact that the subcells are internally connected in series, the output current of a multijunction solar cell is expected to be always equal to the lowest subcell current. When measured in the dark, the spectral response (SR) of such a cell shall be, at all wavelengths, equal to the lowest subcell response. The dark SR's of previously deposited a-Si/a-Si:H and a-Si:H/μc-Si:H tandem cells, however, showed a strange behaviour that only the response of the top cells are observed, i.e. the photogenerated current by the impinging probe beam seems to be able to "leak" through the bottom cell. This "current-leaking" behaviour is found to be related to the deposition conditions of the μc-Si:H n-layer of the top cells. Investigations on a series of a-Si:H/μc-Si:H (micromorph) tandem cells with different TRJ's show that the "current leaking" behaviour disappears after inserting an amorphous silicon interlayer between the bottom cell p-layer and the top cell n-layer, which results in tandem cell dark SR's following the lowest response of the two subcells. Good V_{oc} and FF are obtained on cells with a 5 nm interlayer. Introducing an air-break between this interlayer and the μc-Si:H n-layer of the top cell, which normally results in an increase of the crystallinity of the n-layer, further increases the tandem cell V_{oc}. This can not be explained by the band discontinuity theory proposed by Pellaton Vaucher *et al.* According to that theory, a stronger band-misalignment shall exist between the amorphous interlayer and top cell μc-Si:H n-layer with a higher crystallinity, which could have only decreased the tandem cell V_{oc}. Based on these observations, we propose that the effect of using an amorphous silicon interlayer

in the TRJ of a tandem cell is to reduce the plasma damage on the bottom cell i/p region during the top cell n-layer deposition. Decreasing the plasma power and reducing the deposition time for the top cell n-layer deposition both result in a smaller damage on the i/p region of the bottom cell, therefore a better behaved tandem cell dark SR. Subsequent device simulation conducted by F. Rubinelli et al proves that a defective region in the bottom cell i-layer near the i/p interface can indeed cause the tandem cell dark SR matching the light SR of the top cell. The mechanism is explained to be due to the extra carriers thermally generated in the defective region and collected during the SR measurement. This extra current can not be distinguished from the photogenerated current by the probing light absorbed in the top cell, and therefore, results in an increase in the tandem cell SR, which is similar to the top cell SR.

Multijunction thin film silicon solar cells often show higher *FF* than that of any subcells alone, especially for a current-mismatched solar cell. In Section 7.2, this is explained with the help of experiments and computer simulations on micromorph tandem cells containing hot-wire made a-Si:H and μc-Si:H absorber layers. Besides the increases of *FF* brought about by a shifting of maximum power point (MPP) to a higher voltage by a value of roughly equal to the V_{oc} of the non-limiting subcell(s), and that introduced by a higher shunting resistance normally exists in a multijunction structure, the effect of current mismatch on the carrier recombination in each subcell is discussed. It is showed that due to the accumulation of extra carriers in the non-limiting subcell, the internal field in this subcell is reduced, which results in an increase of the carrier recombination rate; on the other hand, the field in the current-limiting subcell is enhanced, which results in a reduced carrier recombination rate in that subcell. Since the tandem cell *FF* is mostly dominated by the *FF* of the current-limiting subcell, a reduction in the carrier recombination rate in that subcell will most probably result in an increased *FF* of the tandem cell.

In the last part of Chapter 7, a summary of the improved efficiencies of single and triple junction solar cells containing silicon i-layers made by hot-wire CVD are given. Room for the further improvement in cell efficiencies is also discussed.

The present research has given better understanding of the structural and electrical properties of hot-wire made μc-Si:H n-i-p cells, and the behaviour of multijunction solar cells with such layers. The uniqueness of hot-wire CVD and the μc-Si:H i-layer deposited with this technique require a few adjustments in the strategy for optimization of n-i-p (p-i-n) solar cells, such as the use of a reverse H_2 profiling techniques. Due to this, the output performance for cells with a hot-wire CVD deposited i-layer has become very similar to that with a VHF PECVD deposited i-layer. The remaining small difference between the best cells obtained so far in our laboratory and the reported best cell with VHF PECVD i-layer is attributed to the difference in the rough substrate.

Throughout this research, we used sputtered Ag layers as rough surfaces, and these were covered by thin ZnO layers to obtain proper contact with the μc-Si:H n-layer of the n-i-p cells. Cross-sectional transmission electron microscopy (XTEM) examinations of our μc-Si:H solar cell samples have shown that a defective i-layer develops on such rough substrates, especially for cells developed on substrate with a very rough surface (sharp opening angles of valleys at the surface). Considering that the best reported μc-Si:H cells are all developed on substrates with a wet-etched ZnO coating, it is reasonable to suggest that, at least at this stage, the texture-etched ZnO approach currently used by many groups may result in better substrate surface morphology than that obtained by metal sputtering at elevated temperatures, namely a less steep valley combined with a high *rms* roughness. How to obtain effective light scattering while maintaining a proper surface morphology is an urgent question to be answered by the thin film solar cell community.

Samenvatting

In dit proefschrift wordt een aantal aspecten van de ontwikkeling van dunne zonnecellen met een hoog rendement op flexibele substraten behandeld.

In hoofdstuk 2 wordt een overzicht gegeven van het reactiemechanisme van chemische damp depositie met behulp van gasontleding aan hete draden (hot-wire chemical vapour deposition, HWCVD) en van de factoren die een cruciale rol spelen bij een betrouwbare en nauwkeurige karakterisering van zonnecellen.

Hoofdstuk 3 behandelt de prestaties van gehydrogeneerde microkristallijne siliciumcellen (µc-Si:H; n-i-p cellen) die direct gegroeid zijn op ruwe ZnO/Ag achtercontacten. In het bijzonder wordt de invloed besproken die defecten, die tijdens de groei van de i-laag ontstaan, hebben op de open klemspanning V_{oc} en de vulfactor *FF*. Deze defecten worden veroorzaakt door de ruwheid van het achtercontact. Studies van de microstructuur van deze zonnecellen laten zien dat een onderlaag met te grote Ag korrels een hoge dichtheid van shuntpaden (elektrische kortsluitingen) veroorzaakt in de µc-Si:H i-laag. Deze shuntpaden resulteren uiteindelijk in kortsluiting van de gehele cel. Voor cellen die gedeponeerd zijn op een achtercontact met matige ruwheid is de opbrengst van

werkende cellen acceptabel, maar de V_{oc} van de cellen neemt af met toenemende ruwheid van het achtercontact. Dit kan waarschijnlijk worden verklaard aan de hand van twee mechanismen. Bij het eerste mechanisme wordt de i-laag onbedoeld verontreinigd door ophoping van onzuiverheden zoals zuurstof. Deze zuurstof dringt het materiaal binnen door gebieden met een lage dichtheid en microbreuken die ontstaan in nauwe dalen met steile hellingen aan het oppervlak van het substraat en zich door de i-laag voortzetten. Het andere mechanisme hangt samen met de hoeken van de kristallieten die vaak loodrecht op het lokale oppervlak van het achtercontact groeien. De botsingen tussen de zuilvormige structuren die vanaf de verschillende lokale oppervlakken groeien leiden tot een hoge dichtheid van structurele fouten, die energetisch diepgelegen elektrische defecten kunnen veroorzaken in de i-laag van µc-Si:H. Dit heeft op zijn beurt een verhoging van de diode donkerstroom J_0 en de diode kwaliteitsfactor n tot gevolg, waarvan vooral de eerste de oorzaak is van het afnemen van de V_{oc}. Het ontstaan van scheuren en strepen van lage dichtheid wordt verklaard uit het etsen met waterstof van zwakke siliciumbindingen in gebieden waar de kolommen botsen. Het optreden van deze strepen hangt duidelijk af van de openingshoek van inkepingen op nanoschaal in het oppervlak van het achtercontact. Een grenswaarde in de openingshoek voor het ontstaan van strepen met lage dichtheid lijkt rond 110 graden te liggen, hetgeen samenhangt met de bindingshoek van Si-Si-Si in µc-Si:H materiaal. Dit suggereert dat voor het verminderen van het aantal elektrische defecten dat samenhangt met de opbouw van µc-Si:H lagen op een ruwe onderlaag, de lokale vlakken in de onderlaag geen steile hellingen mogen hebben, zodat botsingen van kolommen van silicium voorkomen kunnen worden. Dit zou kunnen leiden tot hogere FF en V_{oc} voor zonnecellen die gegroeid worden op ruwe substraten.

Een veel gebruikte techniek om µc-Si:H zonnecellen met hoog rendement te verkrijgen, is het groeien van de µc-Si:H i-laag met een structuur in het overgangsgebied tussen de amorfe en de microkristallijne fase. Dit wordt normaliter bereikt met een techniek die *hydrogen profiling* heet, waarbij de verhouding van H_2 en SiH_4 gas, R_H, verminderd wordt tijdens het groeien van de i-laag. Dit om te voorkomen dat de kristalliniteit van de i-laag langs de groeirichting toeneemt. Bij zonnecellen met een hot-wire µc-Si:H i-laag vonden we echter dat tijdens de groei van de laag de kristalvorming vermindert in plaats van toeneemt. Dit wordt toegeschreven aan de veroudering van de gloeidraad bij gelijkblijvende stroom door de gloeidraad. Hoofdstuk 4 bespreekt een omgekeerde H_2-profileringstechniek die werd ontwikkeld voor hot-wire CVD om een µc-Si:H i-laag van hoge kwaliteit, d.w.z. met een homogene structuur en betere elektronische eigenschappen, in het overgangsgebied tussen de amorfe en microkristallijne fase te groeien. Om dat te bereiken werd de verhouding van de gasstromen van H_2 en SiH_4 vergroot in plaats van verminderd gedurende het groeien. De

experimentele resultaten zijn veelbelovend en tonen een hoog rendement (8.5 %) voor µc-Si:H n-i-p cellen met een hot-wire CVD i-laag op roestvrij staal folie dat gecoat is met een ruw Ag/ZnO achtercontact. De morfologie van het substraatoppervlak kan echter nog verder geoptimaliseerd worden. Vergeleken met cellen die gemaakt zijn met een constante R_H, tonen de cellen met deze geprofileerde i-laag hogere waarden voor alle belangrijke zonnecelparameters, namelijk de J_{sc} (kortsluitstroom), V_{oc}, en *FF*. Dit wordt toegeschreven aan een verbeterde collectie van de door licht gegenereerde ladingsdragers uit de i-laag. Naast omgekeerde H_2 profilering is gebruik gemaakt van een zogenaamde "koude start" techniek. Hierbij wordt het eerste deel van de i-laag bij een lagere substraattemperatuur gedeponeerd, door de gasinlaat te openen vóórdat het systeem de evenwichtstemperatuur heeft bereikt. Dit leidde tot een verdere toename van de *FF*. Deze toename wordt waarschijnlijk veroorzaakt door een lagere elektrische defectdichtheid in de i-laag, in het bijzonder bij het n/i grensvlak. Het rendement van onze beste cel (8.5 %) is vergelijkbaar met dat van de n-i-p cellen ontwikkeld door United Solar Ovonic Corp. (8.9 %). Die cellen zijn gemaakt op een onderlaag van roestvrij staal met een vergelijkbaar ruwe Ag/ZnO coating, maar hierbij wordt gebruik gemaakt van VHF (Very High Frequency) Plasma-Enhanced CVD depositie van het silicium. Het nog slechts geringe verschil tussen deze twee typen cellen kan toegeschreven worden aan de nog steeds vrij hoge temperatuur van het substraat (270°C) tijdens hot-wire depositie van de i-laag. Wij veronderstellen dat verdere verbetering van dit type cellen (n-i-p µc-Si:H) mogelijk is door optimalisatie van de oppervlaktemorfologie van het achtercontact.

In hoofdstuk 5 wordt de barrière voor ladingstransport, die we hebben gevonden in het gebied van de i/p/ITO lagen van de n-i-p cellen, besproken. De bespreking begint met een literatuuroverzicht van de depositietechnieken die worden toegepast voor het vervaardigen van µc-Si:H p-lagen van hoge kwaliteit. Nadruk wordt gelegd op het probleem van de nucleatie van nanokristallieten aan het oppervlak van een amorfe i-laag van goede kwaliteit bij het groeien van de p-laag.. Daarbij wordt gebruik gemaakt van een gasmengsel van SiH_4, H_2 en $B(CH_3)_3$ (TMB). Bij de eerste pogingen een p-type µc-Si:H laag te groeien bleek de laag amorf i.p.v. microkristallijn te worden. Deze laag heeft een, voor amorf materiaal, te lage doteringsconcentratie. De invloed van de structuurverandering van de p-laag wordt besproken voor proto-SiGe:H n-i-p cellen, omdat de invloed van de structuur van de p-laag op deze cellen het grootst is. Cellen, die in hun AM1.5 *J-V* grafieken een barrière (S-curve) vertonen, werden naverhit. Aan de hand hiervan kon de locatie van de barrière worden bepaald. Deze bevond zich in het i/p/ITO gebied. Door het optimaliseren van de condities voor het groeien van de p-laag, werd de barrière vrijwel geheel verwijderd. Het effect van het naverhitten op het verwijderen van de barrière wordt verder besproken in de studie van de in het donker gemeten *J-V* karakteristieken van drie typen n-i-p cellen met respectievelijk een a-Si:H,

µc-Si:H en proto-SiGe:H absorptielaag. Het belangrijkste mechanisme voor ladingstransport werd geïdentificeerd in drie te onderscheiden gebieden in de J_{dark}-V grafieken. Na het naverhitten vermindert de donkerstroomdichtheid (J_{dark}) van alle drie typen cellen in het gebied dat overheerst wordt door de recombinatiestroom. Dit resulteert in een verhoging van FF en V_{oc} in de AM1.5 J-V karakteristieken. Dit wordt verklaard uit een verbetering van het interne elektrische veld als gevolg van het naverhitten (ná de vorming van het p/ITO grensvlak). Als de diodekwaliteitsfactor wordt uitgezet tegen de spanning (n-V curve) van de proto-SiGe:H (a-SiGe:H) cellen wordt in de curve bij V_{oc} een schouder zichtbaar. Deze schouder blijft ook na het naverhitten zichtbaar. Dit wordt toegeschreven aan een barrière die veroorzaakt wordt door het slecht aansluiten van de energiebanden (*band misalignment*) van de proto-SiGe:H i-laag en de niet geoptimaliseerde p-laag. Voor proto-SiGe:H cellen met een geoptimaliseerde µc-Si:H p-laag, werd deze schouder niet waargenomen. Deze analyse levert een beter begrip van de donkere J-V karakteristiek van zonnecellen met dunne silicium lagen.

Hoofdstuk 6 bespreekt een speciaal verschijnsel dat is waargenomen in de "external collection efficiency" (ECE) van µc-Si:H n-i-p cellen. Als de meting hiervan werd uitgevoerd met gekleurd bias-licht (bijverlichting), met name met blauw licht, werd een aanzienlijk hogere ECE curve waargenomen. De mate van deze toename neemt af met een afnemende intensiteit van het bias-licht, en neemt toe met afnemende intensiteit van het monochromatische licht. Computersimulaties die gebruik maken van het programma D-AMPS, laten zien dat het mechanisme voor dit verschijnsel vergelijkbaar is met het "photogating" (PG) effect dat voorheen werd waargenomen in a-Si:H p-i-n en Schottky diodes. We stellen voor het gebruik van de term "photogating" uit te breiden naar de beschrijving van de waargenomen verschijnselen in µc-Si:H cellen. Simulaties laten zien dat zwakke elektrische velden en een hoge dichtheid van "subgap" defecten in de i-laag de cruciale factoren zijn die leiden tot een flink versterkt PG effect in een µc-Si:H p-i-n structuur. Overeenkomstig hebben we experimenteel waargenomen dat het PG effect zelfs aanwezig is in cellen met i-lagen van goede kwaliteit, maar met een verzwakt intern veld, hetgeen veroorzaakt wordt door het bestaan van een interface barrière bij de i/p/ITO lagen. Door het uitvoeren van een naverhittingsbehandeling kan de barrière verwijderd worden. Hierdoor wordt het interne veld verbeterd en het PG effect aanzienlijk onderdrukt. De gevoeligheid van het PG effect voor defecten kan gebruikt worden om de maximale stroomopbrengst van µc-Si:H zonnecellen te optimaliseren, dat wil zeggen het zoeken naar de balans tussen het interne elektrische veld en de maximale dikte van de i-laag, om een maximale hoeveelheid elektrische energie te verkrijgen uit het ontvangen licht.

Hoofdstuk 7 behandelt specifieke vraagstukken met betrekking tot gestapelde zonnecellen. Sectie 7.1 behandelt de *tunnel recombination junction* (TRJ) van gestapelde

n-i-p cellen. Omdat de subcellen intern in serie geschakeld zijn zal de opgewekte stroom van een gestapelde zonnecel altijd gelijk zijn aan die in de subcel met de laagste stroom. De spectrale response (SR) van zo'n cel zal, gemeten in het donker (zonder bias-belichting), bij alle golflengten gelijk zijn aan die van de subcel met de laagste respons. Deze 'donker-SR' van eerder gemaakte a-Si/a-Si:H en a-Si:H/µc-Si:H tandem cellen toonde echter een afwijkend gedrag; alleen de respons van de bovenop gelegen cel kon worden geobserveerd. Dat wil zeggen dat de door de testlichtstraal opgewekte stroom in staat is door de onderliggende cellen te "lekken". Dit gedrag van "elektrisch lekken" wordt in verband gebracht met de groeicondities van de µc-Si:H n-laag van de bovenste cellen. Onderzoek aan een serie van a-Si:H/µc-Si:H (micromorfe) tandem cellen met verschillende TRJ's toont aan dat het "elektrische lek" verdwijnt als een amorf silicium laag wordt gebruikt tussen de p-laag van de onderste cel en de n-laag van de bovenste cel. Het toepassen van deze extra laag resulteert in een 'donker-SR' die de laagste respons van twee subcellen volgt. Goede V_{oc} en *FF* worden verkregen voor cellen met een 5 nm dikke amorf silicium tussenlaag. Het aan de lucht blootstellen (oxideren) van deze tussenlaag, vóór het aanbrengen van de µc-Si:H n-laag van de bovenste cel, zorgt voor een toename van de kristallisatie van de n-laag en bevordert de V_{oc} van de cel. Het effect van de tussenlaag kan derhalve niet worden verklaard uit de "band discontinuity theory" voorgesteld door Pellaton Vaucher *et al.* Volgens die theorie zou een sterkere discontinuïteit van energiebanden (band-misalignment) ontstaan tussen de amorfe tussenlaag en de µc-Si:H n-laag van de bovenste cel met een hogere kristallijniteit. Dit zou juist tot een lagere V_{oc} moeten leiden. Op basis van deze observaties stellen wij dat door het gebruik van een amorf silicium tussenlaag in de TRJ van een tandem cel de plasmaschade, die gedurende het groeien van de n-laag van de bovenste cel wordt aangebracht aan de i/p regio van de onderste cel, kleiner wordt. Het verkorten van de depositietijd voor de n-laag resulteert in een kleinere schade aan de i/p regio van de onderste cel en daardoor in een beter gedrag van de 'donker SR' van de tandem cel. Een simulatie van de zonnecel, zoals uitgevoerd door F. Rubinelli *et al.*, bewijst dat een defectrijk i/p interface inderdaad tot gevolg kan hebben dat de 'donker-SR' lijkt op de 'licht-SR' van de bovenste cel. Dit werd door hen verklaard met extra thermische ladingsdragers in de defectrijke regio, die gecollecteerd worden bij de metingen. Deze extra elektrische stroom kan niet worden onderscheiden van de stroom die wordt gegenereerd door het in de bovenste cel geabsorbeerde licht, en leidt tot een verhoging van de 'donker-SR' van de tandem cel, die daardoor lijkt op die van de 'licht-SR' van de bovenste cel.

Gestapelde zonnecellen van dunne film silicium vertonen vaak een hogere *FF* dan de enkelvoudige subcellen, in het bijzonder in een elektrisch slecht uitgebalanceerde (*current-mismatched*) zonnecel. In sectie 7.2 wordt dit uitgelegd met behulp van

experimenten en computersimulaties van micromorfe tandemcellen (dubbele zonnecellen) die absorberende lagen bevatten van a-Si:H en µc-Si:H die d.m.v. hot-wire CVD zijn geproduceerd. De verhoging van de *FF* wordt veroorzaakt door de verschuiving van het maximum power point (MPP) naar een hoger voltage. Deze verschuiving is ongeveer even groot als de waarde van de V_{oc} van de niet-limiterende subcel. Naast de verhoging van de *FF* wordt ook het effect van slechte elektrische uitbalancering op de recombinatie in de subcellen besproken. We tonen aan dat vanwege de accumulatie van extra ladingsdragers in de subcel met de grootste fotostroom, het interne elektrische veld in deze subcel gereduceerd is, hetgeen leidt tot een verhoging van de recombinatie van ladingsdragers. Aan de andere kant wordt het veld in de stroomlimiterende subcel versterkt. Dit resulteert juist in een lagere recombinatie van ladingsdragers in deze subcel. Omdat de *FF* van de tandem cel meestal gedomineerd wordt door de *FF* van de stroomlimiterende subcel, zal een afname in de recombinatiesnelheid van ladingsdragers in die subcel leiden tot een verhoogde *FF* van de tandem cel.

In het laatste deel van hoofdstuk 7 wordt een samenvatting gegeven van het verbeterde rendement van enkelvoudige en drievoudig gestapelde zonnecellen die silicium i-lagen bevatten die d.m.v. hot-wire CVD gemaakt zijn. Hier wordt ook besproken waar verdere verbetering van het celrendement mogelijk is.

Het huidige onderzoek heeft tot een beter begrip geleid van de structurele en elektrische eigenschappen van µc-Si:H n-i-p cellen die met behulp van hot-wire CVD geproduceerd zijn, en het gedrag van meervoudig gestapelde zonnecellen met dergelijke lagen. De unieke eigenschappen van hot-wire CVD en de met deze techniek gegroeide µc-Si:H i-lagen vereisen enige aanpassingen in de optimalisatiestrategie voor n-i-p (p-i-n) zonnecellen, zoals het gebruik van omgekeerde H_2 profilering. Als gevolg daarvan is de prestatie van deze cellen nu goed vergelijkbaar met die van cellen waarvan de i-laag is aangebracht met VHF PECVD. De overblijvende kleine verschillen tussen de beste cellen die tot dusver zijn geproduceerd in ons laboratorium en de beste gerapporteerde cellen met een VHF PECVD i-laag worden toegeschreven aan de verschillen in het ruwe achtercontact (substraat). Tijdens dit hele onderzoek gebruikten we gesputterde Ag lagen als ruwe onderlaag, die werden bedekt met een dunne laag ZnO om een goed contact te verkrijgen met de µc-Si:H n-laag van de n-i-p cellen. Onderzoek met *cross-sectional transmission electron microscopy* (TEM) aan een aantal van onze µc-Si:H zonnecellen heeft uitgewezen dat zich op zo'n ruw achtercontact een defectrijke i-laag kan ontwikkelen, met name als het achtercontact een zeer ruw oppervlak heeft (met scherpe openingshoeken van de inkepingen aan de oppervlakte). In aanmerking genomen dat de best geteste p-i-n µc-Si:H cellen in de literatuur alle werden gemaakt op onderlagen met een nat geëtste ZnO laag, is het redelijk aan te nemen, dat, tenminste op dit moment, de door etsen getextureerde ZnO lagen een betere oppervlaktemorfologie hebben dan lagen

die verkregen worden door metaalsputteren bij hogere temperaturen. Deze betere oppervlaktemorfologie bestaat uit een minder diep geaccidenteerd oppervlak terwijl er toch een hoge *rms* ruwheid bereikt wordt. Hoe tegelijkertijd een effectieve lichtverstrooiing te verkrijgen en een goede oppervlaktemorfologie te bereiken is een urgente vraag die nog beantwoord moet worden door de groepen die werken aan de dunne film zonnecellen.

List of publications

Publications related to this research

1. R.L. Stolk, H. Li, C.H.M. van der Werf, R.E.I. Schropp, *Improvement of the Tunnel Recombination Junction in Micromorph Tandem Silicon Solar Cells with Hot-Wire Deposited Absorber Layers*, proceedings, 19th European Photovoltaic Solar Energy Conference, Paris, 2004, 3DV1.52.
2. H. Li, R.L. Stolk, C.H.M. van der Werf, M.Y.S. Rusche, J.K. Rath, R.E.I. Schropp, *Thin film micro- and polycrystalline silicon nip cells on stainless steel made by hot-wire chemical vapour deposition*, proceedings, 3rd internal conference on Hot-Wire CVD (Cat-CVD) process, August 23-27, 2004 Utrecht, the Netherlands. Published on Thin Solid Films 501 (2006) 276-279
3. H. Li, R.L. Stolk, C.H.M. van der Werf, M.Y.S. Rusche, R.E.I. Schropp, *junction silicon thin film solar cells with intrinsic layers prepared by hot-wire CVD*, proceedings, 3rd internal conference on Hot-Wire CVD (Cat-CVD) process, August 23-27, 2004 Utrecht, the Netherlands. Published on Thin Solid Films 501 (2006) 256-259.
4. H. Li, R.L. Stolk, R.H.J. Franken, C.H.M. van der Werf, J.K. Rath, and R.E.I. Schropp, *Implementation of Protocrystalline SiGe:H in Thin Film Multijunction n-i-p Solar Cells*, proceedings, 15th International Photovoltaic Science & Engineering Conference (PVSEC-15) October 19-24, 2005, Shanghai China, 52-7.

5. H. Li, R.L. Stolk, C.H.M. van der Werf, R.H. Franken, J.K. Rath and R.E.I. Schropp, *Optimization of n-i-p protocrystalline SiGe:H thin film solar cells for application in thin film multijunction solar cells*, proceedings, 21st International Conference Amorphous and Nanocrystalline Semiconductor, September 4-9, 2005, Lisbon, Portugal, ThO1.2. Published on Journal of Non-Crystalline Solids, 352 (2006) 1941-1944
6. J Löffler, A. Gordijn, R.L. Stolk, H. Li, J.K. Rath, And R.E.I. Schropp, *Amorphous And Micromorphous Silicon Tandem Cells With High Open Circuit Voltage*, Sol. Energ. Mat. Sol. C. 87 (1-4) (2005) 251-259
7. R. Schropp, R. Franken, A. Gordijn, R.J. Zambrano, H. Li, J. Löffler, J. Rath, R. Stolk, M. van Veen, K. van der Werf, *Thin film silicon alloys with enhanced stability made by PECVD and HWCVD for multibandgap solar cells*, Conference Record of the 31th IEEE Photovoltaic Specialists Conference, 2005, pp. 1371-1376
8. R.L. Stolk, H. Li, J.J.H. Strengers, C.H.M. van der Werf, J.K. Rath, R.E.I. Schropp, *The Potential of Hot-Wire Deposited Microcrystalline Silicon for Thin Film Silicon Single- and Multijunction Solar Cells*, proceedings, 20th European Photovoltaic Solar Energy Conf., Barcelona, Spain 6-10 June 2005,1655.
9. R.L. Stolk, H. Li, R.H. Franken, J.J.H. Strengers, C.H.M. van der Werf, J.K. Rath, R.E.I. Schropp, proceedings, *Hot-Wire Chemical Vapour Deposited Microcrystalline Silicon in Single and Tandem N-I-P Solar Cells*, proceedings, 21st International Conf. on Amorphous and Nanocrystalline Semiconductors, Lisbon, Portugal (2005) 4-9 September, published on J. Non-Cryst. Solids 352 (2006) 1933.
10. H. Li, R.H. Franken, R.L. Stolk, C.H.M. van der Werf, J.K. Rath, R.E.I. Schropp, *Improvement of µc-Si:H n-i-p cell efficiency with an i-layer made by hot wire CVD by reverse H2-profiling*, proceedings, 4th international Conference on Hot-Wire CVD (Cat-CVD) process, October 4-8, 2006, Takayama, Gifu, Japan, published on Thin Solid Films (2007) in Press
11. H. Li, F.A. Rubinelli, J.K. Rath, and R.E.I. Schropp, *Observation Of Photogating Effect In Microcrystalline Silicon Solar Cells And Its Contribution To Device Optimization*, proceedings, 21st European Photovoltaic Solar Energy Conference and Exhibition, Dresden, Germany, 4-9 September 2006, paper 3DV3.51.
12. R.H. Franken, C.H.M. van der Werf, R. L. Stolk, H. Li, J.K. Rath, R.E.I. Schropp, *Control of the growth of textured Ag and Ag:Al2O3 back reflectors for n-i-p solar cells*, proceedings, 21st EUPVSEC, Dresden, Germany, 4-9 September 2006.
13. R.H. Franken, C.H.M. van der Werf, R. L. Stolk, H. Li, J.K. Rath, R.E.I. Schropp, *Correlation between the surface morphology of texture-grown Ag back reflectors and the current enhancement in microcrystalline n-i-p solar cells*, proceedings, 21st EUPVSEC, Dresden, Germany, 4-9 September 2006.

14. R.L. Stolk, H. Li, R.H. Franken, C.H.M. van der Werf, J.K. Rath and R.E.I. Schropp, *High quality hot-wire microcrystalline silicon for efficient single and multijunction n-i-p solar cells*, Mater. Res. Soc. Symp. Proc. 910, A.26.03, (2006).
15. R.L. Stolk, H. Li, R.H. Franken, J.W.A. Schüttauf, C.H.M. van der Werf, J.K. Rath and R.E.I. Schropp, *Improvement of the efficiency of triple junction n-i-p solar cells with hot-wire CVD proto- and microcrystalline silicon absorber layers*, proceedings, 4th international Conference on Hot-Wire CVD (Cat-CVD) process, October 4-8, 2006, Takayama, Gifu, Japan. Thin Solid Films (2007), in Press.
16. R.E.I. Schropp, R.H. Franken, H.D. Goldbach, Z.S. Houweling, H. Li, J.K. Rath, J.W.A. Schüttauf, R.L. Stolk, V. Verlaan, C.H.M. van der Werf, *Hot Wire CVD for thin film triple junction cells and for the SiN passivation layer on polycrystalline Si solar cells*, proceedings, 4th international Conference on Hot-Wire CVD (Cat-CVD) process, October 4-8, 2006, Takayama, Gifu, Japan. Thin Solid Films (2007) in Press.
17. R.H. Franken, H. Li, R.L. Stolk, C.H.M. van der Werf, J.K. Rath, R.E.I. Schropp, *Stable, high deposition rate, wide gap silicon for the rather thick top cells in thin film silicon multibandgap solar cells*, proceedings, IEEE 4th World Conference on Photovoltaic Energy Conversion, May 7-12, 2006, Hilton Waikoloa Village, Waikoloa, Hawaii.
18. H. Li, R.H. Franken, R.L. Stolk, C.H.M. van der Werf, J.A. Schuttauf, J.K. Rath, R.E.I. Schropp, *Improved efficiency of single junction microcrystalline silicon n-i-p solar cells with an i-layer made by hot-wire CVD*, Mater. Res. Soc. Symp. Proc. 989 (2007) A18.3.
19. R.H. Franken, R.L. Stolk, H. Li, C.H.M. van der Werf, J.K. Rath, R.E.I. Schropp, *Understanding light trapping by light scattering textured back electrodes in thin film n-i-p-type silicon solar cells*, J. Appl. Phys. 102, 014503 (2007).
20. H. Li, R.H. Franken, R.L. Stolk, J.K. Rath, R.E.I. Schropp, *Mechanism of Shunting of Nanocrystalline Silicon Solar Cells Deposited on Rough Ag/ZnO Substrates,* GADEST (Gettering and Defect Engineering in Semiconductor Technology), Erice, Italy, 14-19 Oct. 2007.
21. R.E.I. Schropp, H. Li, R.H.J. Franken, J.K. Rath, C.H.M. van der Werf, J.W.A. Schüttauf, and R.L. Stolk, Triple Junction n-i-p Solar Cells with Hot-Wire Deposited Protocrystalline and Microcrystalline Silicon, Mater.Res.Soc.Symp. Proc. Volume 989, Warrendale, PA, 2007.

Other Publications

22. A.H. Mahan, S.P. Ahrenkiel, B. Roy, R.E.I. Schropp, H. Li, D.S. Ginley, *A comparison of Grains nucleation and grain growth during crystallization of HWCVD and PECVE a-Si:H films*, Proceedings, 4th international Conference on Hot-Wire CVD (Cat-CVD) process.
23. A.H. Mahan, S.P. Ahrenkiel, B. Roy, R.E.I. Schropp, H. Li, and D.S. Ginley, *On The Effect Of The Film Hydrogen Content And Deposition Type On The Grain Nucleation And Grain Growth During Crystallization Of A-Si:H Films*, Proceedings IEEE 4th World Conference on Photovoltaic Energy Conversion, May 7-12, 2006, Hilton Waikoloa Village, Waikoloa, Hawaii.
24. J. Stradal, G. Scholma, H. Li, C.H.M. van der Werf, J.K. Rath, P.I. Widenborg, P. Campbell, A.G. Aberle, R.E.I. Schropp, *Epitaxial thickening of AIC polycrystalline silicon seed layers on glass by hot wire CVD*, 3rd internal conference on Hot-Wire CVD (Cat-CVD) process, August 23-27, 2004 Utrecht, the Netherlands.
25. J. Stradal, G. Scholma, H. Li, C.H.M. van der Werf, J.K. Rath, P.I. Widenborg, P. Campbell, A.G. Aberle, R.E.I. Schropp, *Hot wire CVD for epitaxial thickening of polycrystalline silicon seed layers made by AIC on glass*, Conference Record of the 31th IEEE Photovoltaic Specialists Conference, (2005) pp. 1540-1543.

Talks, posters

26. H. Li, R.L. Stolk, C.H.M. van der Werf and R.E.I. Schropp, *Thin film poly silicon nip cells on stainless steel*, Asinet workshop, 25-27 February 2004 in Bratislava.
27. R.L. Stolk, H. Li, J.J.H. Strengers, C.H.M. van der Werf, J.K. Rath, R.E.I. Schropp, *The Potential of Hot-Wire Deposited Microcrystalline Silicon for Thin Film Silicon Single- and Multijunction Solar Cells*, Dutch Solar Cell R&D Seminar, Utrecht, The Netherlands (2005) 28 September.
28. R.L. Stolk, H. Li, J.J.H. Strengers, C.H.M. van der Werf, R.E.I. Schropp, *Hot-Wire CVD Microcrystalline Silicon for Multijunction Solar Cells, 11th Euregional Workshop on Thin Silicon Devices*, Delft, The Netherlands (2005) 2-4 February.
29. H. Li, R.H. Franken, R.L. Stolk, C.H.M. van der Werf, J.K. Rath, R.E.I. Schropp, *Controlling the quality of microcrystalline i-layers made by hot-wire chemical vapour deposition by using a reverse H_2 profiling technique,* accept as Oral presentation on 22nd International Conference on Amorphous and Nanocrystalline Semiconductors (ICANS 22), Colorado, USA, 19-24 August 2007.
30. H. Li, R.L. Stolk, R.H. Franken, J.W.A. Schüttauf, J.K. Rath, and R.E.I. Schropp, *Development of single and multijunction solar cells with Hot-Wire CVD deposited active layers,* accept as Oral presentation on 22nd International Conference on Amorphous and Nanocrystalline Semiconductors (ICANS 22), Colorado, USA, 19-24 August 2007.

Acknowledgements

Everything comes to an end. While looking back through my research at Utrecht University and my staying in the Netherlands, I was touched by the help, support and encouragement that I have had from such many people.

It is my great privilege to have worked under the guidance of Prof. Ruud Schropp. Ruud, thanks for having let me work in the SID group. It is from here that I rediscovered my interest in doing good scientific work, it is here that I realized that how technologies are developed from scientific ideas, and it is here that I learned how a scientist can do good research work while fully enjoying his free time. This is all because that I got a chance to work here, in such a wonderful group, in such a fascinating country.

Thanks for the committee who spend time reading the manuscript of my thesis. They are Prof. J. Dijkhuis, Prof. W. Sinke, Prof. J. Kelly, Prof. H. Rudolph, and Dr. W. van Sark. Wilfried, especially thanks to you for reading the earlier versions, and for spending time to do corrections. They are really helpful! Thanks Dr. Francisco Rubinelli at INTEC, Universidad Nacional del Litoral, Argentina for discussion and his

contribution on Chapter 6. Thanks Dr. Ernst van Faassen for reading the draft version and the discussion. Also thanks Dr. Friedhelm Finger at IPV Juelich who had contributed to recommending me to the solar cell group at Utrecht University.

I would like to thank C.H.M. van der Werf and Ruurd Lof, who had done excellent job in assisting many researchers in our group. I was lucky to be one of them. Karine, all the samples used in my study were made by you. I cannot go anywhere without your constant help in preparing them and your precise control on every deposition parameters. Ruurd, you were the first one I worked with in the UU group. I cannot imagine how things will be without your continuous development on the characterization setups. Sharing the similar curiosity and perfectionism, we work happily together on many of those setups, such as PDS, CPM, Spectra response, activation energy, SSPG, FPTS, FTIR and the data logger for PASTA. All my demands had come true with your amazing creativity. It has been so enjoyable to work with all the equipments you have made or improved! Then my closest team mates Robert Stolk and Ronald Franken, I enjoyed being in the same project with you. Robert, how can I say in such a limited space so many thanks for your constant help in these four years in organizing the triple project's work, in improving my English writings for almost every publication I wrote, and in helping me solving various problems in the beginning of my work in Holland. Bedankt! Ronald, my roommate, all your effort in developing textured back reflector has given the greatest help in improving the solar cell efficiencies. We cannot go far without your exploration on sputtering deposited Ag, ZnO and ITO, which has been for a long time a lack of the Utrecht group. Thank you for your excellent work. I enjoyed the discussions we have had, and I am happy that I have been sharing the same room with you. Then Dr Jatin Rath. Jatin, I have learned much from the discussions that we had in the past few years. Many of our chats during coffee pauses and lunch breaks have come to new ideas and new results. Thanks!

For the people who were not in the triple project: our secretary Riny de Haas, my colleagues Paula Bronsveld, Monica Brinza, Yaohua Mai, Yanchao Liu, Vasco Verlaan, Arjan Verkerk, Arjen Bink and Caspar van Bommel. Riny, so nice to work with you in this group, with your efficient work you have given me so much help. Not only did you support my work, but also did you give me many useful tips and suggestions for staying in Holland. Bedankt! Paula, it was really joyful to have you as a colleague for almost all my research period here. Your creative work on the silicon growth at low temperature had also improved my understanding on the film growth mechanism on a conventional temperature. It was from you that I learned the basics of Unix and the software package IDL. I have been enjoying using many of your IDL programs such as Ramps and Optics2. Your contribution on the surface area integration program for AFM pictures has made the estimation of rough surface influences on the current density possible. Thank you and I

wish you success with your thesis writing and a good start for your new job! Monica, it is such a pleasure to have you as my new roommate. I hope you did not get too much disturbed by the mess on my table. Though you came very recently, I have learned quite a lot from you, especially about the defect density characterization for amorphous silicon materials. Thanks and I wish you success with your research. Yaohua, I am so glad to work together with you again! As good friends, we have been collaborating since long time ago, and I am sure we well keep enjoying our close friendship and joyful collaboration in the future. I wish you success in your research and your family reunion in Holland. Yanchao, Thanks for the help you have given us and many other Chinese scholars and students here, I am glad to see that you have become a solar cell man too. I wish you success with your PhD research! Vasco, I was so happy to share with you my birthday in Lisbon during the ICANS-21 conference. In my heart I still own you a birthday cake. Thanks for your help in doing RBS measurement and data interpretation, also thanks for your constant effort in helping to keep this group well integrated. Success with writing your thesis! Arjan, thanks for the nice discussion and talks. Congratulations for your new baby, and enjoy your PhD research at UU! Arjen and Caspar, thanks for many suggestions and tips in handling setups, and also for staying in Holland.

For the people outside of the device physics group, Marites Violanda, Eddy van Hattum, Govert Kruijtzer and Wim Arnold Bik. Marites, thank you for reading the first version of Chapter 1, your remarks was very helpful. I wish you enjoy your PhD study here. Eddy and Govert, thank you for helping me doing the ERD, RBS and XPS measurements in your valuable time. The talks we had always let me feel happy. Eddy, Cheers! My best wishes for your new job at FOM. Govert, my opinion is that finding a good girl friend to share your life with is not too much harder than quantum mechanics. Success with you PhD thesis, and enjoy the rest time of your research here. Wim, also thanks for doing and arranging RBS and ERD measurement on the poly sample we have had.

For the people who have left the SID groups during my research: Marieke van Veen, Raul Jimenez Zambrano, Hanno Goldbach, Geoffrey Munyeme, Aad Gordijn, Bernd Stannowski, Jochen Loffler and Gerard van der Mark. Thank you, Marieke! Almost all the Hot-wire silicon materials were made with the recipes developed during your PhD research here at UU. Without your excellent work, I would have spent much more time to make silane concentration series on material characterization. Raul, same thanks for your help in providing useful information on SiGe:H materials and solar cells, and the help on the AMPS software package even during the time you were no longer working at UU. Hanno, 4 years, we had a really joyful time here at UU. I could recall many chats we had in the corridor, at the coffee corner, and in our offices. Though the jogging team we have had was not the fastest, it had brought us much happiness while running together. I

enjoyed that. I wish you success for your job in Oerlikon and also my best wishes to your family. Geoffrey, it has been a pleasure to share with you such a nice time here at UU, I wish you a good time in Zambia. Then the former "ASTER" people: Aad, thanks for helping me in many characterization issues, and many practical help in my house finding and moving. Jochen, the discussion we had was always encouraging and helpful, and I enjoyed the wine testing course we had together. Bernd, we had only short time overlapping in doing research together, but as a Post Doc at UU at that time you gave me a good impression on how a good scientist should be. Bedankt! Gerard, thanks for designing the metal masks for contact evaporation. They are really cool. Gert, Adam and Marielle, you have left long before the end of the Triple project. Yet, I own you thanks for your contribution on the ITO depositions, Raman characterization and the teaching of many other characterization techniques. I wish you all the best for your work and life.

During the triple project, many students have their contributions on the development of solar cells, especially Jan Willem, Jirka Stradal, and Geert Scholma. Jan Willem, you have done a wonderful job on the characterization of triple junction solar cells, we were so lucky to have had you near the end of the triple project. Thank you, and I hope you enjoy your first world round trip and start in September a successful new study. Jirka and Geert, thanks for your efforts in developing poly-Si materials. I wish you both success with your future study and research.

Besides, I owe many thanks to the people who helped me settle down in Utrecht and keep me concentrating on my research. They are Ms Linda Taju in the international relation office of Utrecht University, Thea de Caes and her colleagues in the personnel department of science faculty, Maria Vliegen, my lovely landlady, and Mariet Jellema, my nice neighbour while I lived in Nijenheim, Zeist. Linda, so many thanks for your continuous help in finding good accommodations for my family. Having been living in such many houses you provided us has itself become a valuable experience for me. Bedank! Thea, whenever I needed help, you are always there. In the past few years, you have helped me filled uncountable amount of paper works which would otherwise cost me months if I had filled them all myself. Thanks! Maria, I had a really nice time while I lived in Zeist. It was so joyful to share a house with you! Mariet, it was such a nice memory to have had you as my neighbour. Also many thanks to you for having helped me much in filling the many forms in Dutch and doing house moving before my family's coming to Holland in 2004.

I owe a great deal to the close friends of my family, Izaak de Hulster and Dorottya Nagy, who have been accompanied us through all these years with joy and sometimes with a bit sadness. Thank you for all the help you have given us! We were so lucky to have had you to share our life in Holland.

这部分的内容我以中文表达。我在荷兰的工作能够顺利开始还必需感谢我在中国非晶硅薄膜领域尤其是南开大学曾经的同事与朋友们的支持与鼓励。这之中包括我曾经的领导，同事，导师南开大学的耿新华教授，王宗畔教授，熊少珍教授，徐温元教授，以及中国科学院研究生院朱美芳教授。感谢你们为我提供的推荐信，没有它们，我在荷兰的工作可能不会顺利地开始以至如今最终完成。感谢你们在我在南开工作的九年期间的鼓励与支持，使我在非晶薄膜领域积累了充实的实践经验以至终生受用。感谢我曾经在南开的其他同事特别是赵颖教授，孙云教授，李长健教授，孙仲林教授曾经对我的帮助。感谢吴仲康教授对我的关心与支持。感谢许许多多南开的其他同事多年的友谊与支持。在南开学习，生活与工作的十三年已成为我生命中最美好回忆的一部分。祝你们工作顺利，生活愉快。

Last but most important, I thank my beloved family, my wife Ruiying, my son Yiming and my parents Zhe Li and Huiqin Liu. Without your support, it is not possible for me to come to Holland, do and complete my research here. I owe you so much. I love you!

最后，我要把我最诚挚、最深刻的爱献给我最敬爱的亲人们，我的父亲母亲，以及我的夫人与孩子。没有这些年来你们对我的鼓励和祝福，我在这里的研究工作能够进行是不可想象的。我把这本饱含着我工作心血的论文献给你们。 I love you!

Curriculum Vitae

Hongbo Li was born in Tianjin, China on September 11, 1971. From September 1986 to July 1989, he studied at the 31st high school in Tianjin. From September 1989 to June 1993, he studied in the Physics Department at Nankai University, Tianjin, and received his Bachelor degree in science (Optics). From July 1993, he worked as a young researcher at the institute of Photo-electronics, Nankai University, with a focus on the deposition of silicon thin film material and devices by plasma enhanced chemical vapour deposition techniques. In September 1997, he started his 3-year postgraduate study on microelectronics and solid state electronics at Nankai University and received his Master degree in science in May 2000 with a thesis, *thin film amorphous silicon solar cells deposited on plastic foil*. He started in October 2002 his PhD research with the Surfaces, Interfaces, and Devices group, at Debye Institute of the Utrecht University, the Netherlands, working for the Dutch SenterNovem project "High efficiency triple junction thin film solar cells". Since January 2007, he worked for the European FP-6 project SE-PowerFoil with Helianthos, aiming at improving efficiency of flexible solar cell laminates.